# HIGH PERFORMANCE SILVER-BASED BRAZES, CURRENT COLLECTORS, AND ELECTRICAL CONTACTS FABRICATED VIA A NOVEL PARTICLE INTERLAYER DIRECTED WETTING AND SPREADING TECHNIQUE

By

Genzhi Hu

## A DISSERTATION

Submitted to
Michigan State University
in partial fulfillment of the requirements
for the degree of

Materials Science and Engineering—Doctor of Philosophy

#### **ABSTRACT**

Reliable dissimilar material bonding is crucial in various fields, and the silver-nickel brazing technique has emerged as a promising method for joining ceramics to stainless steel. This technique offers improved mechanical bonding strengths and enhanced longevity compared to the commonly used Ag-CuO reactive air brazes. Additionally, this Particle Interlayer Directed Wetting and Spreading (PIDWAS) technique can also be used to prepare silver circuits on a variety of substrates that cannot normally be wet by molten silver. However, there is a lack of understanding regarding the mechanical and electrical behavior of circuits or current collectors produced using this technique. Furthermore, its applicability to aluminum containing stainless steel and the feasibility of using alternative interlayer materials remain uncertain.

To address these gaps, this dissertation focuses on investigating the mechanical and electrical performance of Ag-Ni circuits created through the PIDWAS technique. The bonding strength between alumina substrates is examined and compared to commercially available silver pastes such as Heraeus C8710 and DAD-87. The sheet resistivity on alumina and contact resistivity on lanthanum strontium manganite are evaluated to assess the electrical properties of Ag-Ni current collectors. The findings demonstrate that PIDWAS-produced Ag-Ni layers exhibit better overall performance than conventional Ag contact pastes for circuit and current collector applications.

Furthermore, this research explores the feasibility of utilizing the Ag-Ni PIDWAS brazing technique for aluminum containing stainless steel and investigates the mechanical, electrical, and durability aspects of the resulting braze joints. The braze joints are evaluated under various conditions, including as-produced, air annealed, reduction-oxidation (redox) cycled, and rapid thermal cycled states. The results indicate that Ag-Ni brazes effectively getter and stabilize

unwanted aluminum from the substrate, highlighting its potential for applications involving aluminum containing stainless steel.

Additionally, a novel PIDWAS brazing technique using Ag-Pt is introduced in this work. The mechanical and electrical performance, as well as the microstructure changes of Ag-Pt brazes, are evaluated in as-produced, air annealed, redox cycled, and rapid thermal cycled conditions. The results demonstrate that Ag-Pt brazes outperform Ag-Ni brazes in oxidizing environments. The potential application of Ag-Pt brazes in other systems is also discussed. In summary, this work demonstrates that 1) different PIDWAS interlayer materials can be used to promote the wetting and spreading of molten silver, and 2) these interlayers can also be used to chemically getter undesirable surface-segregating substrate components.

Copyright by GENZHI HU 2023 This dissertation is dedicated to my beloved family, who instilled in me the value of education and supported me throughout this journey.

## **ACKNOWLEDGEMENTS**

The silver-nickel part of the presented work was supported by Department of Energy Office of Fossil Energy under Award Number of DE-FE-0031672. The silver-platinum part of the presented work was supported by Nissan North America. The microscopy and mechanical tests were conducted in the Michigan State University Composite Materials and Structures Center. I am grateful to Department of Energy, Nissan North America, and the Composite Materials and Structures Center.

I would like to express my deepest gratitude to my PhD advisor Dr. Jason D. Nicholas for his patience with the guidance of my PhD research. The discussions in our weekly meetings and daily research life always helped my research. The encouragement I received from my advisor alleviated my anxiety from the intense research work and the pandemic. I am thankful to my dissertation committee members Drs. Thomas R. Bieler, Alexandra Zevalkink, Patrick Kwon, for their valuable suggestions for my PhD work. I am thankful to Dr. Timothy Hogan for allowing me to use his resistance measurement setup. I would like to thank my many collaborators for their help and contributions. I would also like to thank weekly metal group meeting members Drs. Carl Boehlert, Martin Crimp, Philip Eisenlohr, and my fellow metals group meeting students. They often gave me suggestions on my presentations and research work.

I also want to thank my group members, friends, and fellow graduate students who have significantly contributed to both my personal well-being and the advancement of my research. Drs. Quan Zhou, Yuxi Ma and Yubo Zhang helped my research and had many lunches with me. Yuan Peng, Zihan Li, and other friends had frequent contact with me in the past years. They gave me support and made my journey more fulfilling. Their company helped me a lot. My roommate, Dr. Tong Zhou, helped me a lot when I came to the United States. Dr. Jiawei Lu, Dr. Wanyue Peng,

Min Feng, Dr. Jiyun Park, Sevan Chanakian, Tanzilur Rahman, and other fellow graduate students from the ChEMS Department greatly enriched my journey through their interactions and support. It was a pleasure spending these years with you all.

Finally, I am deeply grateful to my family, especially to my parents, for their constant support during my academic journey. Their unswerving belief in education has guided me to where I am today. Little did I anticipate that a pandemic would coincide with my pursuit of a PhD abroad. Throughout these years, moments of isolation and loneliness have been challenging. Their support and love have been my guiding light, helping me overcome difficulties and uncertainty.

# TABLE OF CONTENTS

1	Int	roduction	1
	1.1	Global Energy Challenges	1
	1.2	Solid Oxide Fuel Cells Technology Overview	1
	1.3	SOFCs Mechanism and Structure	
	1.4	Challenges and Objectives	4
2	Lit	terature Review	7
	2.1	Silver Based Brazing Techniques in SOFCs	
	2.2	Other Silver-Based Bonding Techniques	
	2.3	Summary	
3	Ex	perimental Methods	22
	3.1	Sample Preparation	
	3.2	Air Annealing Treatment	
	3.3	Reduction-Oxidation Cycling Treatment	
	3.4	Extremely Rapid Thermal Cycling Treatment	
	3.5	Bonding Strength Measurement	
	3.6	Resistance Measurement	
	3.7	Scanning Electron Microscopy	
4	Ag	g-Ni Circuits on Alumina	43
	4.1	Introduction	43
	4.2	Tensile Strength	
	4.3	Sheet and Contact Resistivity	
	4.4	Microstructure Analysis	
	4.5	Discussion	50
	4.6	Summary	51
5	Pe	rformance and Durability of Ag-Ni Braze Joints to Dissimilar Stainless Steels	52
	5.1	Introduction	
	5.2	Microstructure Analyses	53
	5.3	Shear Strength Results	61
	5.4	Contact Resistivity Results	62
	5.5	Competing Brazing Techniques	64
	5.6	Discussion	79
	5.7	Summary	83
6	Pe	rformance and Durability of Ag-Pt Braze Joints to Dissimilar Stainless Steels	84
	6.1	Introduction and Rationale of Ag-Pt Brazing	
	6.2	Microstructure Analyses	
	6.3	Shear Strength Results	
	6.4	Contact Resistivity Results	100
	6.5	Ag-Pt Joints for Ceramic-Steel Brazing	101
	6.6	Discussion	101

	6.7	Summary	108
7	Coı	nclusions	109
ΒI	BLIO	GRAPHY	112
ΑF	PEN	DIX A: BRAZING TEMPERATURE PROFILES AND RATIONALE	128
ΑF	PEN	DIX B: METAL-ALUMINIDE DUCTILITY DETERMINATION	132
ΑF	PENI	DIX C: SIDE EFFECTS OF COMBINING PT AND NI INTERLAYERS	135

#### 1 Introduction

# 1.1 Global Energy Challenges

The world is facing significant energy challenges, including the depletion of traditional fossil fuels, increasing demand for energy, and the impact of energy production on the environment [1]. The energy sector is one of the largest contributors to greenhouse gas emissions, which have been linked to climate change and its associated effects, such as rising sea levels, more frequent and severe weather events, and biodiversity loss [2]. Moreover, a large portion of the world's population still lacks access to reliable and affordable energy, hindering economic development and human progress [1]. As a result, there is an urgent need for sustainable and clean energy technologies to meet the world's growing energy demand while mitigating the negative environmental impacts. Solid Oxide Fuel Cells (SOFCs) represent one such technology, offering high efficiency, low emissions, and fuel flexibility [3, 4]. It has the potential to solve global energy challenges.

## 1.2 Solid Oxide Fuel Cells Technology Overview

Solid Oxide Fuel Cells operate by converting chemical energy into electrical energy through a solid-state electrochemical process [3, 4]. The working principle of SOFCs is based on the oxygen ion conducting ceramic electrolyte that separates the fuel and air compartments of the cell. When fuel and air are supplied to the anode and cathode sides, respectively, the chemical reactions occur on the surfaces of the electrodes, generating an electric potential across the electrolyte. SOFCs have many advantages over conventional energy generating methods, which include 1) higher electrical efficiency of up to 60% [3, 5-7], which is significantly higher than the 30-40% efficiency of traditional power plants [8]. 2) lower emissions (SOFCs emit only water vapor and carbon dioxide [4], whereas coal-fired power plants emit significant amounts of sulfur

dioxide, nitrogen oxides, and unburned hydrocarbons). 3) higher gravimetric and volumetric power density [9]. 4) fuel flexibility (SOFCs can operate on a variety of fuels, including hydrogen, methane, propane, and other hydrocarbons, as well as biogas and even coal-derived gases) [10]. 5) low noise and vibration [11]. As a result, SOFCs have the potential to play a key role in meeting the growing energy demands of the future, while reducing greenhouse gas emissions and promoting sustainable development.

### 1.3 SOFCs Mechanism and Structure

SOFCs consist of several layers of functional materials, including anode, cathode, and electrolyte, which are sandwiched between two current collectors [12]. The oxygen gas gets reduced into oxygen ions by the electrons on the porous cathode layer. Then, the oxygen ions get transported across the electrolyte to the porous anode layer and react with the energy carriers. Figure 1-1 shows a schematic diagram of a typical operating SOFC. In this process, energy is transformed from chemical energy to electrical energy. Electrons will be transported through external circuits, and water and carbon dioxide form. Because the whole reaction relies on the oxygen gas reaction on the cathode and the oxygen ions diffusion across the dense electrolyte, the operation temperature of SOFCs is relatively high (usually above 600°C) to ensure sufficient reaction rates [3, 4, 9, 12, 13]. With the development of advanced materials and manufacturing techniques, the performance and durability of SOFCs have been significantly improved. Low temperature Solid Oxide Fuel Cells (LT-SOFCs) have been reported to operate below 500°C with satisfactory efficiency [13, 14]. They have shown great potential as a clean and efficient power generation technology for both stationary and mobile applications.

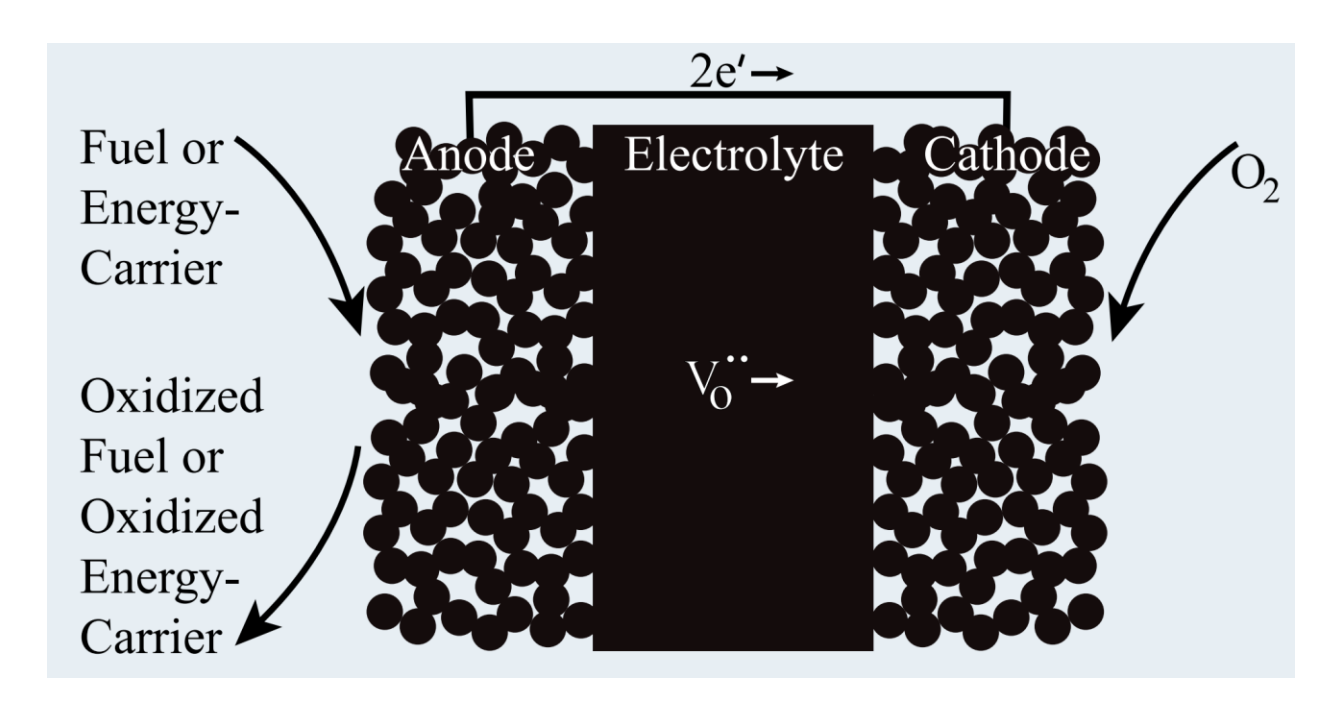


Figure 1-1 Schematic diagram showing the operation of a typical SOFC with anode, electrolyte, cathode, and the external circuits, from [3].

SOFC cells can be connected differently for different applications. For planar SOFCs, interconnects are utilized to stack two cells. Sealant is utilized for the bonding between the cell picture frame and the interconnect. The sealant also needs to separate the fuel and air at high temperature. Figure 1-2 shows the schematic of a SOFC stack [15]. The cell unit, which contains the cathode, anode and electrolyte, is bonded to the stainless steel picture frame. The picture frame is then bonded to the interconnect. This structure is repeated to build the whole SOFC stack. SOFCs can also be designed as tubular cells. However, when compared to planar SOFCs, tubular SOFCs have a lesser energy density, although the sealant issues are not as significant as in the planar design [16-19].

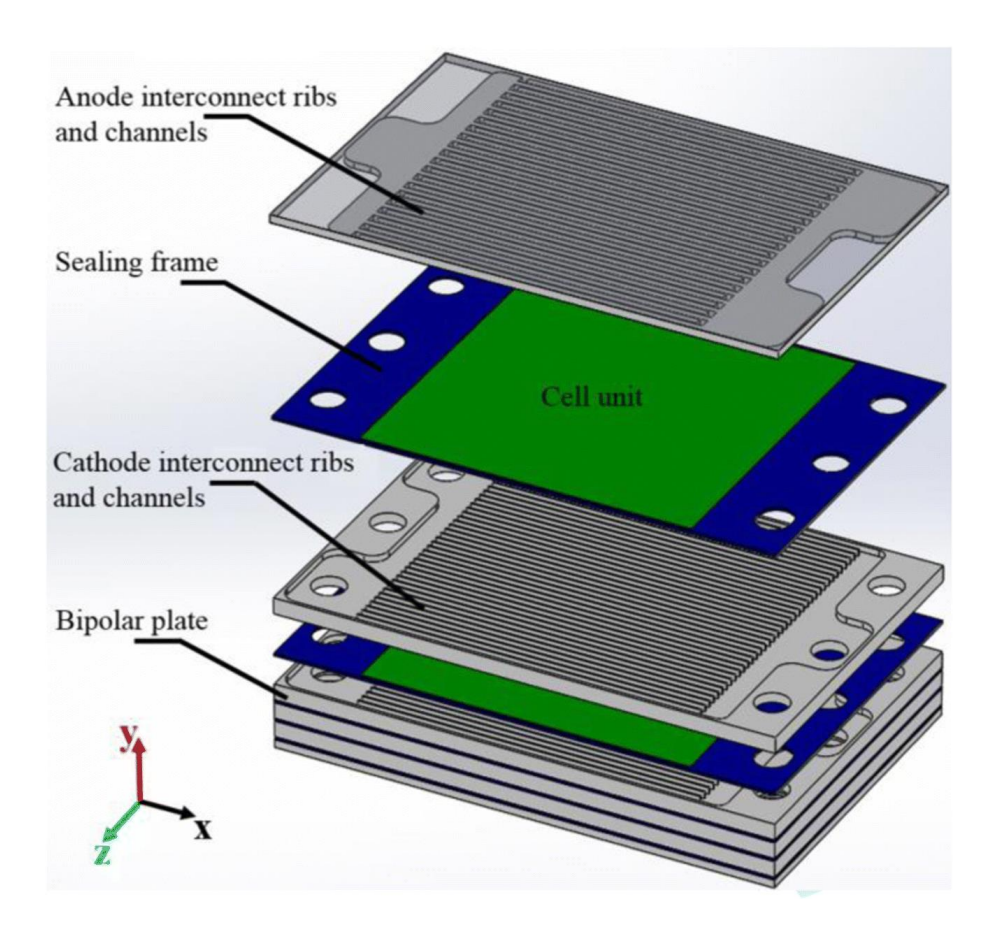


Figure 1-2 Schematic diagram of the Solid Oxide Fuel Cell stack components.

## 1.4 Challenges and Objectives

Despite the advantages of SOFCs, the implementation of SOFCs is hindered by the high price and the long-term durability concerns. The durability challenges include the degradation of the sealants [20], the reduction of the cathode performance [21-31], the degradation of the electrolyte [32-38], and the decline of the anode performance [39-55].

The sealants play a crucial role in bonding different components and separating the fuel and air in SOFCs. As such, degradation of the sealants can result in damage to the entire cell stack and lead to gas leakage, which can cause a decrease in power output efficiency, or even explosion [56].

Sealing in SOFCs can be achieved through two main methods: compressive seals, where load is applied to the seal during operation, and rigid seals, where no load is applied during operation [57]. In the category of compressive seals, metallic compressive seals or mica-based compressive seals are commonly used. For rigid seals, glass/glass-ceramic sealants or brazes are the primary options.

Metallic compressive seals rely on the plastic deformation of metals, such as gold and silver, to achieve effective sealing [57]. However, the deformability of the metals used can impact the quality of the sealant. Designing the shape of the sealant can also help accommodate less-deformable metals [58, 59], which introduces complexity and rises cost.

Mica-based compressive seals operate by causing mica crystals to collapse into each other, ensuring a good seal [57]. However, this technique requires the application of high stress to the sealant in order to achieve a low leak rate. Uniform distribution of stress during operation can be challenging to achieve as well.

Glass and glass-ceramic sealants are widely used in SOFCs and have been tested for 1,000 hours of operation without significant degradation [60]. These sealants rely on the softening of the sealant above its glass transition temperature to ensure good sealing. Matching the glass/glass-ceramic coefficient of thermal expansion (CTE) with the other cell components is required. Unfortunately, some alkali-metal containing glasses are reactive with other SOFC components [61, 62] and may facilitate the volatility of chromium [63, 64], which may degrade the cathode performance. Glasses and glass/ceramics are also inherently brittle, limiting the ability to accommodate thermally and mechanically induced stress [57].

Brazes, on the other hand, have lower stiffness compared to ceramics and can undergo plastic deformation, making them capable of accommodating and reducing stresses [57]. However,

various factors can cause degradation in braze sealants. For instance, poor wetting or volatile species formation during manufacturing can cause defects that may further worsen over time [65]. During operation, the braze sealant composition may change, with the oxide in the sealant getting reduced by the fuel on the anode side, leading to defects [66-68]. Additionally, the fuel and air may react in the sealant and form water, causing pores [69]. Furthermore, the sealant may break due to thermo-mechanical stress during thermal cycles caused by a CTE mismatch with the other cell components [57, 70, 71].

This work aims to address some of the key challenges faced by SOFCs, with a specific focus on braze sealant durability and Cr poisoning. The objective of this study is to systematically evaluate and propose solutions to these challenges through a structured approach. In Chapter 4, the effectiveness of a silver-nickel current collector for ceramic components is thoroughly examined. Chapter 5 extends the research to the application of the silver-nickel PIDWAS brazing technique on aluminum-containing stainless steel. By utilizing this alternative material, the study aims to mitigate the Cr poisoning issue commonly associated with standard stainless steel. Understanding the behavior and performance of the braze joint in this specific context is vital for advancing the practical implementation of SOFCs. Chapter 6 explores a novel silver-platinum PIDWAS brazing technique. This technique is developed with the aim of further enhancing the performance and durability of the braze joint in similar applications. The investigation includes evaluations of the mechanical, electrical, and durability properties of the brazing technique under different conditions, such as air annealing, redox cycling, and rapid thermal cycling tests.

#### 2 Literature Review

# 2.1 Silver Based Brazing Techniques in SOFCs

Silver-based brazing techniques have been extensively studied for their potential use in SOFCs due to their advantageous characteristics, such as a melting point that strikes a balance between remaining solid at typical SOFC operating temperatures and melting at relatively low temperatures during the brazing process, low reactivity with oxygen and other elements to ensure the stability of the braze joints, ductility which accommodates stress induced by CTE mismatch, and excellent electrical conductivity. Various silver-based brazing techniques, such as Ag-CuO, Ag-Ti-CuO, Ag-CuO-Pt, and Ag-Ni, have been investigated for their effectiveness in joining SOFC components, including the anode, cathode, and interconnect. Previous studies have shown that these filler materials can produce high-quality, hermetic seals with low contact resistance and good thermal and mechanical stability. However, the use of silver-based brazing techniques in SOFCs has some challenges, including the potential for delamination, microstructural degradation, and hydrogen embrittlement. Thus, further research is needed to investigate the brazes and to develop new techniques for mitigating these issues.

### 2.1.1 Silver-Copper Oxide Brazes for SOFCs

Weil *et al.* developed the Ag-CuO air brazing technique and now it has been the most widely used method for ceramic to metal joining in SOFC applications [72, 73]. This method involves the use of a silver-copper oxide (Ag-CuO) composite material as the brazing filler. After mixing the silver and copper powder, the filler material is then fired in air to melt the mixture [72, 74-76]. The copper oxide precipitate, which is soluble in silver, segregates to the surface of molten silver and reacts with the alumina substrate by forming copper aluminate. The phase diagram in Figure 2-1 illustrates the Ag-CuO system [76, 77]. The presence of low solubility of copper oxide

in silver plays a significant role in enhancing the interaction between the filler metal and the substrate, consequently promoting favorable wetting behavior. Because the ceramic-ceramic bonding is more favorable than metal-ceramic bonding, this reaction reduces the wetting angle between the filler metal and the substrate and improves the bonding [68, 72]. Density functional theory calculations indicate that more dissolved oxygen at the interface also promoted good wetting [78]. Similar reaction can also happen on the stainless steel side by forming copper-chromium oxide phases [72].

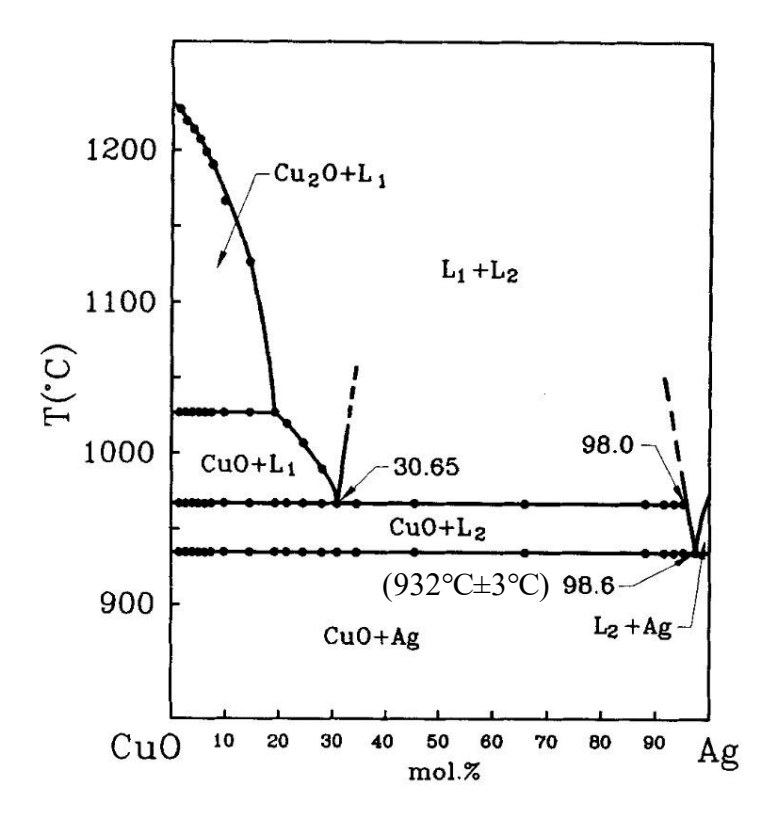


Figure 2-1 Pseudo binary Cu<sub>x</sub>O-Ag phase diagram [76, 77]. CuO can partly dissolve in Ag above 932°C.

Figure 2-2 shows the contact angle of Ag-CuO on SOFC electrolyte (yttria-stabilized zirconia, YSZ), interconnect (stainless steel FeCrAlY) and cathode (lanthanum strontium cobalt ferrite, LSCF) at different CuO concentration. The silver contact angle on YSZ and stainless steel can drop from >80° to ~40°, and from ~100° to ~50°, respectively, with lower than 10 mol.% of

CuO addition [57]. However, the contact angle is still large. Defects will form during brazing due to the still relatively high wetting angle of 50 degrees. Adding more copper oxide can greatly reduce the contact angle. Figure 2-3 shows the contact angle and four-point bend strength of alumina-alumina Ag-CuO brazes at different Ag content in the Ag-CuO filler material [76]. When the CuO concentration reaches over 30 mol.%, the filler contact angle on YSZ and stainless steel can drop to 30° [57, 76]. But adding more CuO will also decrease the bend strength of the joint [76], and 30° is still a high enough to produce poor-wetting-induced brazing defects. The incorporation of 8 mol.% of CuO into the filler metal yields the optimal combination of high mechanical performance and satisfactory wetting properties.

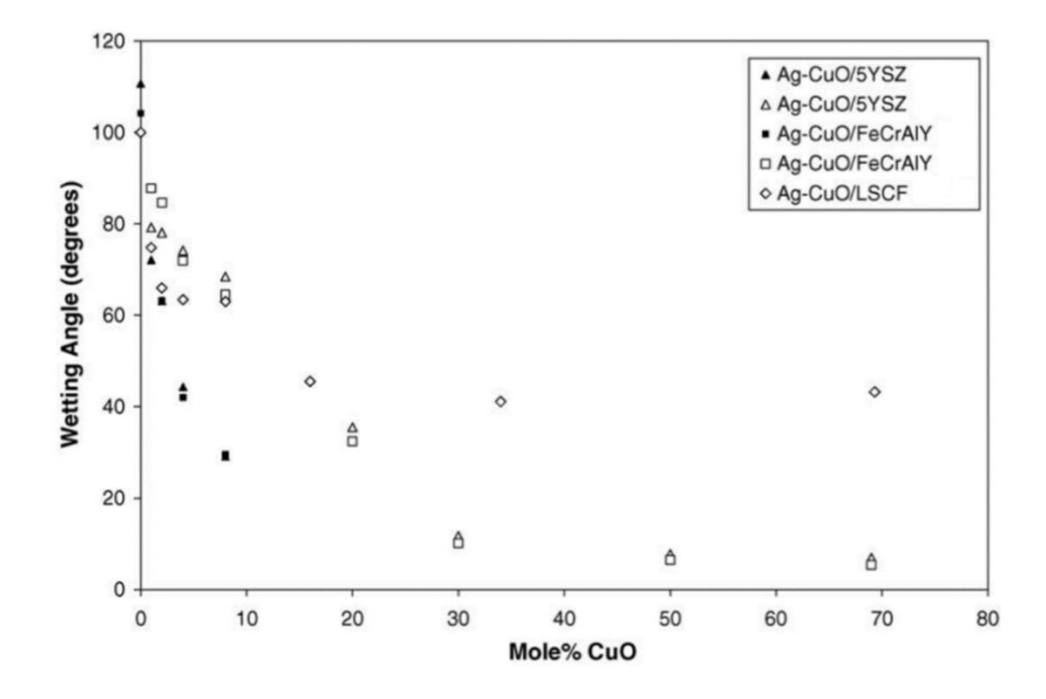


Figure 2-2 Contact angle of Ag-CuO on SOFC electrolyte (YSZ), interconnect (stainless steel FeCrAlY) and cathode (lanthanum strontium cobalt ferrite, LSCF) at different CuO concentration [57].

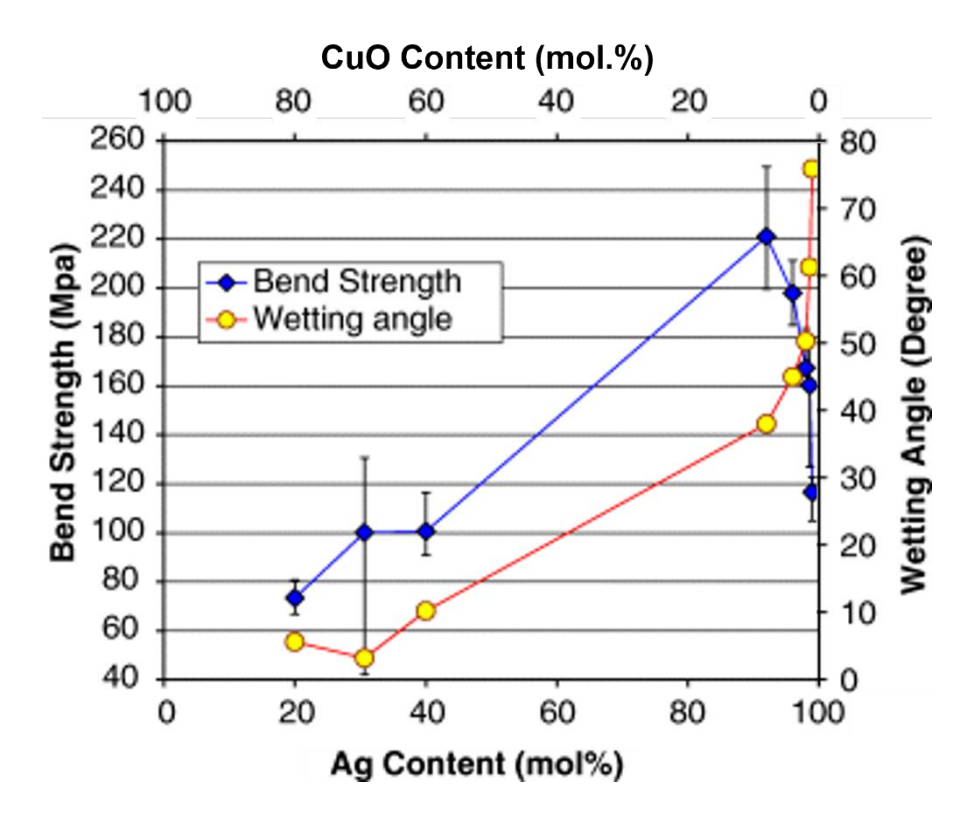


Figure 2-3 Room-temperature four-point bend strength and contact angle as a function of Ag content. Modified from [76].

In addition, the fuel creates a reducing environment on the anode side during SOFCs operation. The CuO in Ag-CuO brazes will get reduced on the anode side, which can lead to pore formation [65]. Tests were performed to observe the structural degradation in actual working conditions by annealing the braze with air on one side and hydrogen on the other side. It was observed that after 100-hour dual atmosphere annealing at 800°C, the samples could remain intact. But after 1000-hour dual atmosphere annealing at 800°C, pores had formed due to the CuO reduction by hydrogen [68]. This is much shorter than the necessary ~40,000 hours of operation for commercial deployment [69].

Another problem is the high diffusivity of oxygen and hydrogen in silver [79]. The oxygen and hydrogen ionic diffusivity in silver at 750° are  $1.6 \times 10^{-5}$  cm<sup>2</sup>•s<sup>-1</sup> and  $7.0 \times 10^{-5}$  cm<sup>2</sup>•s<sup>-1</sup>, respectively [79]. Hence, gaseous-water-induced pores from the hydrogen-oxygen reaction will

also be a problem after a long period of time (>1,000 h) running at 800°C with air on one side and hydrogen on the other side of the braze [68]. The high hydrogen diffusivity may also lead to silver embrittlement issues observed by Klueh and Mullins [80] and by Singh *et al.* [81] in high-purity silver. The defects formed due to poor wetting or precipitate reduction may speed up the gaseous-water-induced pores formation.

Recently, efforts were made to improve the Ag-CuO brazes by introducing other components. There has been extensive research conducted on adding titanium to the Ag-CuO brazes [82-87]. Adding titanium can greatly improve the wetting behavior of the Ag-CuO braze [82-84]. However, achieving good brazes requires vacuum or inert environment, which can reduce and deteriorate the cathode materials [88]. There has been some research about the alumina nanoparticles reinforced Ag-CuO brazing [89, 90]. Adding alumina nanoparticles to the filler material can tailor the filler's coefficient of thermal expansion and improve the shear strength. When 8 wt.% of alumina nanoparticles were added to the Ag-CuO filler, the maximum shear strength reached 62 MPa, which was ~70% higher than using Ag-CuO filler [89, 90]. However, cracks may form because of the addition of alumina [89]. Furthermore, several researchers have explored the potential of Ag-CuO-Pt as a brazing material [91]. Adding platinum into the filler material reduced the coefficient of thermal expansion mismatch and strengthen the silver by uniformly dissolving and distributing in silver [91]. But there are drawbacks including higher cost and the potential to increase the brittleness of the filler metal.

## 2.1.2 Silver-Nickel Brazes for SOFCs

As described in Zhou *et al.*, in collaboration with Delphi Automotive, the Nicholas, Bieler, and Qi Group at Michigan State University developed the Particle Interlayer Directed Wetting and Spreading (PIDWAS) Ag-Ni brazing technique for joining stainless steel and ceramic substrates

[65]. This technique employs a transient nickel interlayer to facilitate silver wetting and promote the formation of a dense braze joint between the substrates.

First, the nickel paste was printed onto the YSZ substrate and then sintered in argon. Next, a pure silver foil was placed between the nickel printed YSZ and bare stainless steel, and heated in argon to melt the silver and form a dense joint [65]. Figure 2-4 shows the microstructure of the dense braze joint formed between 441 stainless steel and YSZ. The joint was observed to be free from cracks or any other visible defects.

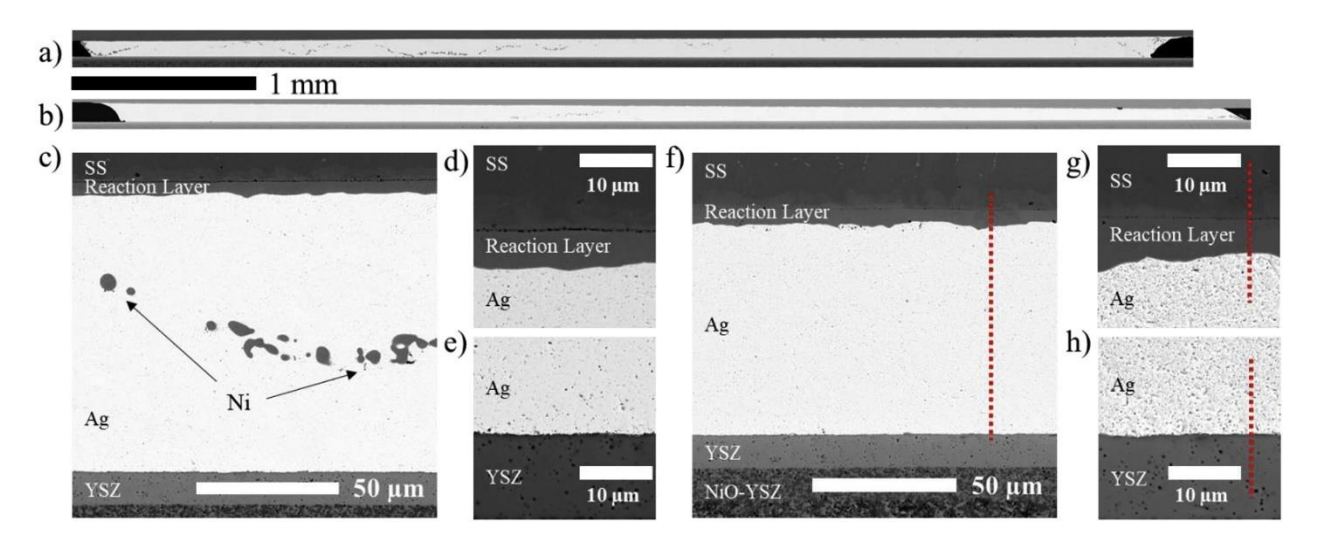


Figure 2-4 Backscattered scanning electron microscopy of (a) the entire 15-min brazed braze joint cross-section, (b) an entire 30-min brazed braze joint cross-section, (c-e) zoomed-in, representative portions of the 15 min brazed joint, and (f-h) zoomed-in, representative portions of the 30 min brazed joint [65].

Figure 2-5 shows the phase diagram between silver and nickel [92]. It is worth noting that silver exhibits low solubility in nickel. Consequently, during the melting process of silver, only a small amount, approximately 1%, dissolves into the nickel. This dissolvent reaction gives rise to a reaction layer, which leads to high work of adhesion between silver and nickel and enables good wetting. This solubility is important to good wetting. Systems with zero silver solubility usually have poor wetting behavior, which will be discussed in Subchapter 6.1.

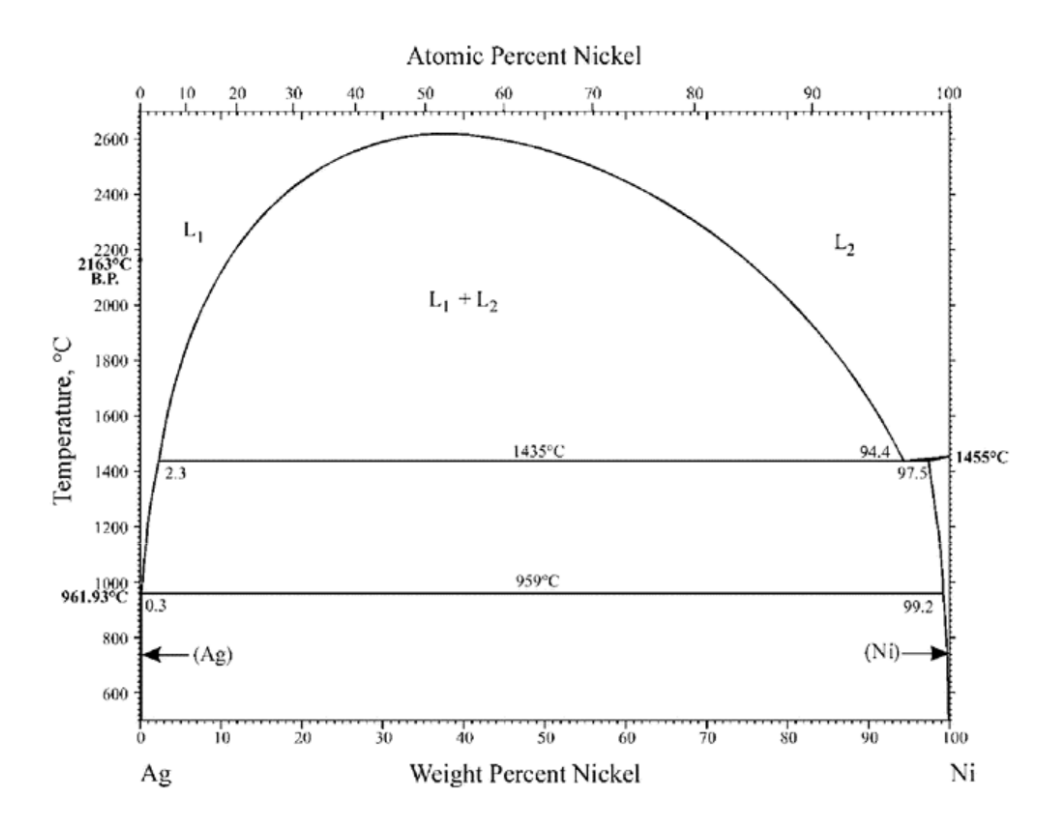


Figure 2-5 The Ag-Ni phase diagram [92]. Silver can partly dissolve in nickel near silver melting point.

This PIDWAS technique has also been demonstrated as a feasible approach for preparing silver-based circuits on non-wettable substrates [93]. Figure 2-6 shows the *in-situ* silver contact angle measurements that were conducted at ~1030±10°C in flowing argon on 96 wt.% Al<sub>2</sub>O<sub>3</sub>, 99.9 wt.% Al<sub>2</sub>O<sub>3</sub>, AlN, and 3YSZ substrates. Bare substrates showed contact angles greater than 90°, but the use of a porous nickel interlayer led to almost 0° contact angles on the same substrates [93]. This improved silver wetting can be beneficial for creating circuits on a variety of substrates. Figure 2-7 shows plan and cross-sectional views of circuits made using the PIDWAS technique [93]. Intricate silver circuits can be made on non-wettable substrates by introducing a nickel interlayer.

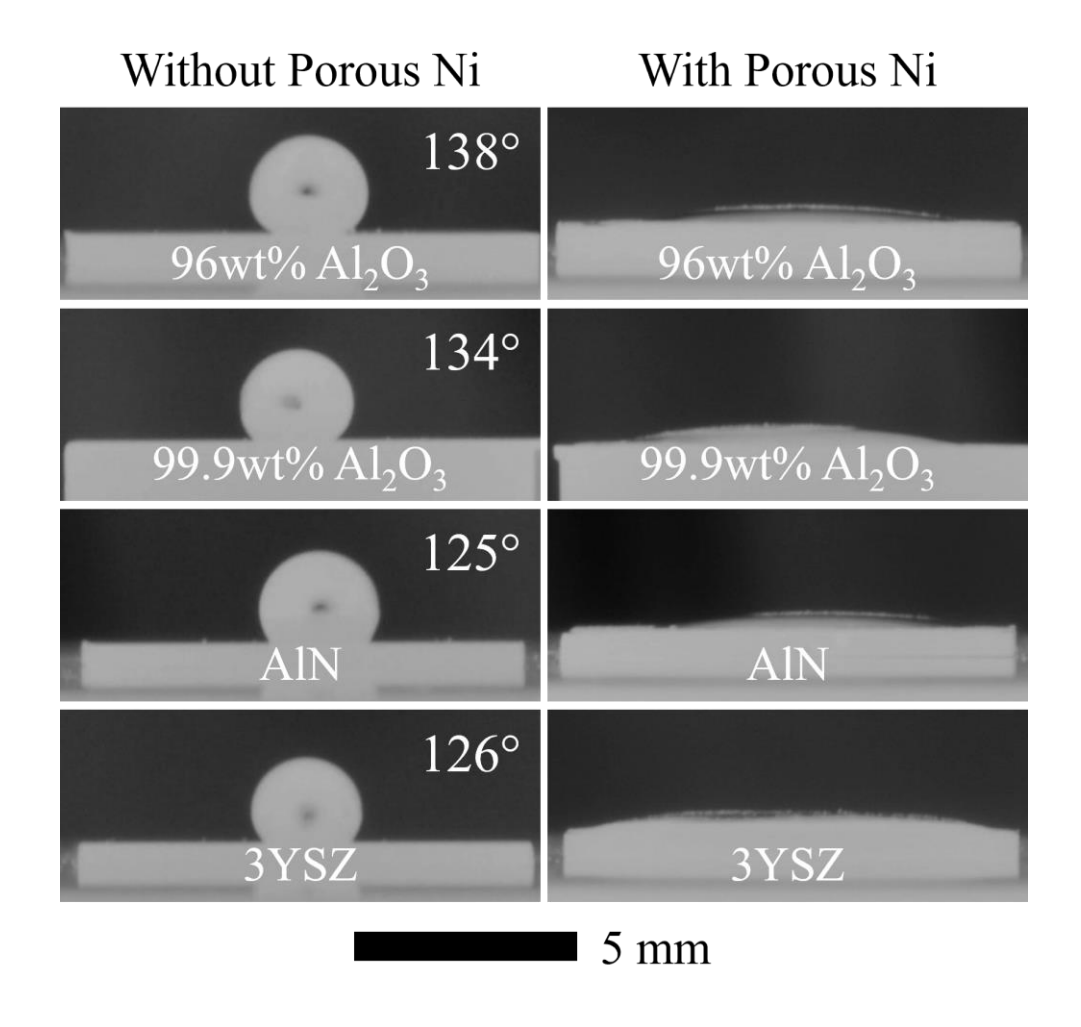


Figure 2-6 In-situ silver wetting angle on 96 wt.%  $Al_2O_3$ , 99.9 wt.%  $Al_2O_3$ , AlN, and 3YSZ in flowing argon at ~1030±10°C [93].

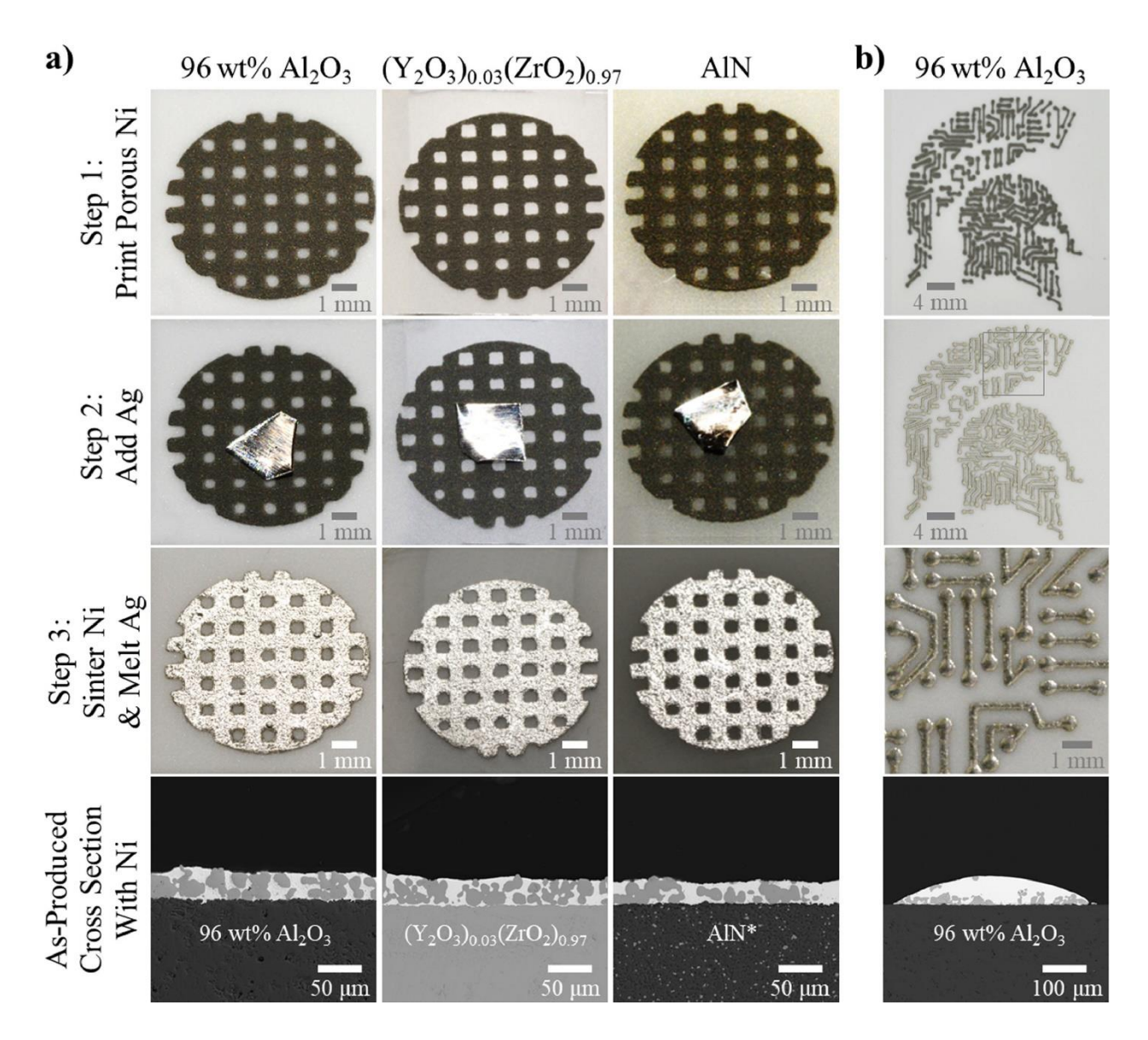


Figure 2-7 Plan and cross-sectional views of Ag-Ni circuits produced via (a) the ~ $1030 \pm 10^{\circ}$ C melting and lateral spreading of bulk Ag through porous Ni grid patterns previously sintered for 2 hours at  $840 \pm 10^{\circ}$ C on various substrates, and (b) the ~ $1030 \pm 10^{\circ}$ C melting and local infiltration of screen-printed Ag pastes on screen-printed Ni pastes that were sintered for 2 hours at  $840 \pm 10^{\circ}$ C on 96 wt.% Al<sub>2</sub>O<sub>3</sub> substrate [93].

Park *et al.* conducted an analysis of the nickel pattern and discovered that the nickel interlayer can be tailored for wetting enhancement, regardless of whether it is porous or not [94]. They also proposed a calculation model to determine the maximum enhanced wetting area based on the intrinsic wetting performance between the liquid and the substrate. These findings suggest that the PIDWAS technique has the potential to be applied to other systems beyond the silver-

ceramic systems discussed above. Termuhlen *et al.* analyzed the interaction between the molten metal and interlayer and found that there is a lower limit for the interlayer particle size [93]. Small particle sizes cannot guarantee good wetting because the particles may not remain securely anchored to the substrates and can get pulled off due to the capillary force during wetting. They also analyzed the imbibition of molten silver through the PIDWAS interlayer [95, 96]. The new model showed a better agreement with experimental observations by calculating pore radii based on the size distribution instead of the permeability.

# 2.2 Other Silver-Based Bonding Techniques

Silver-based brazing can effectively bond ceramics or ceramic/metal substrates. However, there are also alternative techniques available for bonding silver to oxide ceramics, which can produce varying bonding strengths under different conditions. These methods can serve as valuable points of reference for the silver based brazing techniques.

## 2.2.1 Constrained Sintering

Constrained sintering leverages the varying local curvatures of particles within a porous silver sample to facilitate sintering and joint formation between silver and alumina. This technique allows for the fabrication of parts within a relatively low temperature range of 200-550°C, eliminating the need for atmosphere control and external pressure [97-100]. The resulting joint achieves a maximum relative density of only 68% [101], and only achieves a corresponding maximum shear strength of 18 MPa [97, 102, 103]. This technique is commonly used in Solid Oxide Fuel Cells for current collector paintings, structure sealing, or joining. The two most widely used silver paste in the SOFC community are Heraeus C8710 and DAD-87 [104-109].

Heraeus C8710 is a silver paste developed by Heraeus Electronic Thick Film Materials. According to the datasheet, it contains 81.38% solid content. The suggested solidification procedure is holding at 850°C for 10 minutes in air.

DAD-87 is developed by Shanghai Research Institute of Synthetic Resins Co. LTD. It contains 82.0% silver content. The shearing strength at room temperature is typically larger than 4.0 MPa. The volume resistivity is typically lower than  $9.0 \times 10^{-6} \Omega$ •m. The suggested solidification procedure is holding at 250°C for 1 hour in air.

# 2.2.2 <u>Pressure Assisted Sintering</u>

Pressure assisted sintering is a technique that utilizes external stress on the porous silver to facilitate joint formation between silver and alumina. This technique enables sample fabrication within a low temperature range of 250-275°C, without requiring a special atmosphere [101, 110]. However, it should be noted that this technique necessitates the application of relatively high external pressure, typically ranging from 1-50 MPa [101, 110, 111]. Pressing during fabrication introduces complexity, raises cost, and can crack the substrate. The resulting joint exhibits a relative density of 87% [101] and demonstrates a maximum shear strength of 50 MPa [101, 110].

### 2.2.3 Reaction Assisted Sintering

Reaction assisted sintering is a technique that utilizes a chemical or physical reaction to facilitate joint formation between porous silver and alumina. This technique can be accomplished within a relatively low temperature range of 200-400°C [112, 113], with some reports even achieving it at 90°C [114]. The specific atmosphere required depends on the nature of the reaction involved. External pressure is also applied, typically ranging from 5-15 MPa [112-114]. The resulting joint demonstrates a relative density of 85-95% [112-114] and exhibits favorable mechanical properties, including a maximum tensile strength of 70 MPa [112] and a maximum

shear strength of 36 MPa [113]. However, this technique is intricate and necessitates careful consideration of the reaction design to facilitate the bonding process.

# 2.2.4 Stress-Migration Bonding

Stress-migration bonding is a technique that exploits the internal compressional film stress arising from the coefficient of thermal expansion mismatch or other factors to facilitate joint formation between silver and alumina. This method can be carried out within a temperature range of 200-300°C under any atmospheric conditions [115, 116]. It relies on internal stress, eliminating the need for external stress application. By employing this technique, it is possible to achieve nearly 100% densification of the joint, accompanied by a high shear strength of up to 120 MPa [115]. But this method cannot produce thick Ag films on substrates with an arbitrary CTE.

# 2.2.5 Light/Current Assisted Sintering

Light assisted sintering is a technique that harnesses the Joule heat generated by focusing light on the porous silver to promote joint formation between silver and alumina. This method has been reported to be successfully achieved at temperatures of 290°C [117] or 850°C [118], regardless of the atmospheric conditions. Notably, it does not necessitate the application of external stress. The resulting joint exhibits a relative density of approximately 70% [117]. However, no specific information regarding the mechanical properties of silver on alumina has been reported in the literature. A similar technique can also be achieved by heating the sample with the Joule heat from electric current. However, these techniques do not ensure reliable adhesion, and they also present challenges in achieving intricate pattern preparation.

## 2.2.6 Pressure Joining

Pressure joining is a technique that utilizes the deformation of dense silver foils in contact with a substrate under external force to facilitate joint formation between silver and alumina. This method can be accomplished within a temperature range of 500-900°C, independent of atmospheric conditions [119, 120]. The effectiveness of this technique relies on the application of external pressure, typically around 6-7 MPa, to deform the silver foils [120, 121]. Given the use of dense silver foils, the resulting joint exhibits a relative density of 100% [120, 121]. The mechanical properties reported for this joint are favorable, with a maximum tensile strength of 70 MPa [119, 120, 122] and shear strength ranging from 68-75 MPa [122, 123]. But it also introduces complexity, raises cost, and can crack the substrate.

# 2.2.7 Transient Liquid Brazing

Transient liquid brazing is a technique that employs the localized low melting-point component to create a joint between silver and alumina. It involves the addition of specific components to reduce the melting point locally by forming a pseudo-binary eutectic composition. Upon joint formation, these additive components undergo a transformation, either into the substrate or solid silver. The successful execution of this technique relies on locally melting the pseudo-binary eutectic composition, typically at temperatures near but below the melting point of silver [124]. The atmospheric conditions required may vary depending on the specific additive used. Notably, this technique does not necessitate external pressure. However, no specific information about the mechanical properties of the resulting silver-alumina joint has been reported in the literature. This technique also presents challenges in achieving intricate pattern preparation.

# 2.3 Summary

This chapter provides a survey of various bonding techniques utilizing silver as the primary material. Among these techniques, the Particle Interlayer Directed Wetting and Spreading (PIDWAS) technique emerges as a method with distinct advantages.

The PIDWAS technique does not require the application of external pressure during the brazing process, making it a highly versatile and adaptable method that can be utilized in a wide range of systems. It can be utilized in different systems, regardless of the difference in coefficients of thermal expansion (CTE) between the materials being bonded. This versatility is particularly valuable as the CTE mismatch often poses challenges in achieving reliable and durable bonds.

One key advantage of the PIDWAS technique is its ability to ensure good wetting between the bonding materials. The interlayer material employed in this technique promotes wetting and eliminates the formation of defects, resulting in a high-quality bond. Furthermore, the PIDWAS technique has the added benefit of eliminating pores that may arise due to brazing component reduction. Pores can significantly compromise the integrity and mechanical properties of a bonded joint. By facilitating improved wetting and eliminating pores, the PIDWAS technique effectively enhances the integrity and strength of the bond, reducing the risk of failure.

Additionally, the PIDWAS technique allows for the creation of intricate patterns. This is particularly advantageous in applications where complex geometries or specific designs are required. By employing the PIDWAS technique, researchers and engineers can precisely control the wetting and spreading of the molten silver, enabling the formation of intricate patterns with high precision and repeatability.

In summary, the PIDWAS technique stands out among the various silver-based bonding techniques discussed in this chapter. Its unique characteristics, such as the absence of external

pressure, versatility in different systems, excellent wetting capabilities, elimination of pore formation, and the ability to create intricate patterns, make it an attractive choice for a wide range of applications.

# 3 Experimental Methods

## 3.1 Sample Preparation

# 3.1.1 Silver-Based Circuits on Alumina

The bonding strength of circuits on alumina was assessed by conducting tensile strength tests on head-to-head alumina bars jointed together.

Ag-Ni tensile test samples were prepared by printing nickel paste onto the substrates and melting pure silver between them. Specifically, a mixture of 400 mesh 99.8%+ nickel powder (Alfa Aesar; Tewksbury MA, USA) and Heraeus V737 polymetric vehicle (Heraeus Electronics Thick Film Materials; West Conshohocken PA, USA) was manually stirred at a 2:1 weight ratio to create nickel paste. A silver piece was flattened to approximately 350 µm thickness using a hammer, weighing around 0.18 g. Next, 99.6% pure alumina bars measuring 60mm×10mm×5mm (AdValue Technology; Tucson AZ, USA) were subjected to a 5-minute ultrasonic cleaning in acetone. After cleaning, the nickel paste was screen-printed to the end face of the alumina bars, followed by a 10-minute room temperature holding period and subsequent drying in an 80°C oven for ~10 minutes. An 80-mesh screen containing 20 μm stainless steel wires at 45° and 14 μm PEF2 emulsion (Sefar Inc; Depew NY, USA) was used. The printed alumina bars were then glued to an alumina substrate using super glue, with a ~350 μm thick silver piece positioned in between the printed layers. The assembled samples were placed in a furnace filled with argon and flowing argon gas at a rate of 20 sccm. NiO pieces were included in the furnace to facilitate the oxidation of carbon from the organic material. The samples underwent heating to ~830°C and were held at this temperature for 2 hours in a carbon-gettered NiO-buffered argon atmosphere. Subsequently, the temperature was raised to ~1025°C and maintained for 30 minutes before cooling to room temperature at a rate of 5 °C/min.

Figure 3-1 shows the schematic of the screen-printing process. The screen contains predesigned pattern that allows the paste to penetrate. The squeegee then moves across the screen, pressing it down to apply the paste and print the pattern onto the substrate.

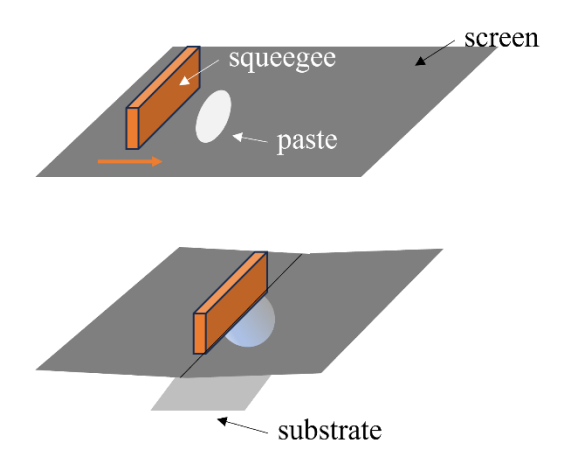


Figure 3-1 Schematic of the screen-printing process. The squeegee moves to apply the paste and print the pattern on the substrates.

Figure 3-2 shows the schematic of the Ag-Ni tensile test sample. This design was selected for evaluating the bonding strength due to the geometry of the alumina bars. The commercial alumina bars are 5 mm thick, which makes it challenging to print the pattern on the 10 mm by 60 mm side. As a result, the tensile test setup was used for this evaluation.

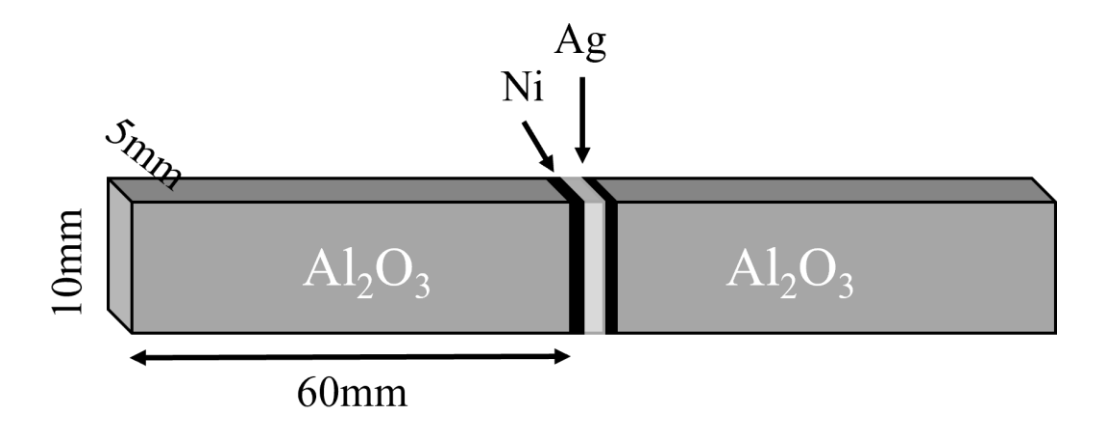


Figure 3-2 Schematic of the Ag-Ni tensile test sample.

Heraeus C8710 tensile test samples were prepared by printing the Heraeus C8710 paste (Heraeus Electronics Thick Film Materials; West Conshohocken PA, USA) onto alumina bars and subsequently sintering it. Initially, 99.6% pure 60mm×10mm×5mm alumina bars (AdValue Technology; Tucson AZ, USA) underwent a 5-minute ultrasonic cleaning in acetone. After cleaning, Heraeus C8710 paste was stirred with a spatula to ensure homogeneity and then printed onto the end face of one alumina bar through 9 passes using the screen printer. The same 80-mesh screen containing 20 µm stainless steel wires at 45° and 14 µm PEF2 emulsion was used. Specifically, 8 layers of Heraeus C8710 were printed on each bar. After each individual pass, the sample was held at room temperature for ~10 minutes to let the paste flow evenly and then placed at a drying oven at 80°C for 10 minutes. This layering process was repeated for a total of 8 layers, with a final layer of Heraeus C8710 silver ink being applied to one of the bars. The alumina bars were affixed to a larger alumina substrate using super glue, aligning the two ink-printed ends with each other. Lastly, another alumina substrate was placed on the opposite side of the alumina bars, forming a sandwich structure with the alumina bars in between. The assembled bars and substrates were placed in an air furnace, with one alumina bar positioned on top of the other, and subjected to heating at a rate of 5°C/min to 850°C, held at 850°C for 10 minutes, returned to 750°C, held at 750°C for 10 hours to densify the paste, and cooled to room temperature at 5 °C/min.

Similarly, the DAD-87 tensile test samples were produced by printing DAD-87 paste (Shanghai Research Institute of Synthesis Resins; Shanghai, China) onto alumina bars and sintering them. The DAD-87 paste was applied to the same alumina bar using a single pass. After assembling the samples in a manner consistent with the Heraeus C8710 samples, they were initially heated to 250°C at a rate of 5°C/min in air and held at this temperature for 1 hour, as per the

manufacturer's instructions. The samples were then subjected to densification at 750°C for 10 hours, followed by cooling to room temperature at a rate of 5°C/min.

The sheet and contact resistivity samples were prepared following a similar procedure. First, nickel inks were screen printed onto either alumina substrates (for sheet resistivity measurements) or lanthanum strontium manganite (LSM) substrates (for contact resistivity measurements). The sapphire substrates (Laserage Technology Corp; Waukegan IL, USA) had a composition of 96.2 wt.% Al<sub>2</sub>O<sub>3</sub>, 2.6wt.% SiO<sub>2</sub>, 0.8 wt.% MgO, 0.2 wt.% CaO, 0.1 wt.% Fe<sub>2</sub>O<sub>3</sub>, and 0.1 wt.% Na<sub>2</sub>O and were used in the as-received state. The LSM pellets had a composition of La<sub>0.8</sub>Sr<sub>0.2</sub>MnO<sub>3-δ</sub> and were produced by uniaxially compacting commercial LSM powder (Praxair Specialty Ceramics; Woodinville WA, USA) in a 25.4 mm diameter stainless steel die at ~1.7 MPa before firing at 1450 °C for 20 hours using nominal heating and cooling rates of 5°C/min. This procedure produced LSM pellets that were >90% dense and were subsequently polished smooth with P4000 SiC sandpaper. Then, 400-mesh 99.8%+ nickel powder (Alfa Aesar; Tewksbury MA, USA) was mixed with Heraeus V737 polymeric vehicle in a 2:1 weight ratio and manually stirred with a stainless-steel rod to produce the nickel paste. The nickel paste was printed onto the alumina or LSM substrates using an CP-885-R screen printer (AMI Presco; Lebanon NJ, USA) with a 400mesh screen containing 12 µm stainless steel wires and a 16 µm thick PEF2 emulsion (Sefar; Depew NY, USA). Three passes of nickel paste were screen printed onto each substrate, with 10 minutes of 80°C drying between each pass. Afterwards, a pure Ag ink was screen printed directly overtop (i.e. using the same screen pattern as) the Ni inks. To produce the Ag ink, 400-mesh 99.9% silver powder (Alfa Aesar; Tewksbury MA, USA) was mixed with Heraeus V737 polymeric vehicle in a 2:1 weight ratio and manually stirred with a stainless-steel rod to produce the silver paste. Six passes of the silver paste were printed on the Ni, with 10 minutes of 80°C drying between

each pass. In a carbon-gettered, NiO-buffered argon flowing across the sample at 20 sccm, the Ag-Ni samples were heated to ~830°C with a nominal 5°C/min heating rate, held at ~830°C for two hours (to sinter the nickel network without melting the silver), heated to ~1025°C with a nominal 5°C/min heating rate, held for 30 minutes at ~1025°C to melt the silver, and cooled to room temperature with a nominal 5°C/min cooling rate.

The Heraeus C8710 and DAD-87 samples were fabricated in a similar manner. Specifically, either Heraeus C8710 or DAD-87 was screen printed, as purchased, onto alumina and LSM substrates using a screen with the same characteristics as the one used for the Ag-Ni circuits. Three passes of either Heraeus C8710 or DAD-87 were printed, with 10 minutes of 80°C drying between each pass. Following the manufacturer-suggested heating schedules, the Heraeus C8710 and DAD-87 samples were heated to 850°C for 10 minutes, and 250°C for 60 minutes, respectively, using 5°C/min heating and cooling rates in 20 sccm of carbon-gettered, NiO-buffered argon (an atmosphere chosen to allow direct comparison with the Ag-Ni samples).

Some Ag-Ni, Heraeus C8710 and DAD-87 samples were then annealed for 10 hours at 750°C in air, using 5°C/min nominal heating and cooling rates. Some Ag-Ni samples were also annealed for 250 hours in 750°C air. For all samples, a NanoMap 500LS profilometer (AEP Technology; Saratoga CA, USA) was used to measure the circuit thickness before and after resistivity measurements.

## 3.1.2 Silver-Based Brazes between Stainless Steels

The braze samples for mechanical test and microstructure analysis were prepared between 441SS (Straub Metal International; Ashley PA, USA) and aluminum containing ferritic stainless steel alloy JFE20-5USR, AFA (JFE Steel Corporation; Tokyo, Japan), which contains 5-6 wt.% aluminum and can form alumina scale for outstanding oxidation resistance at high temperatures.

The braze joints were made by melting silver between pre-printed interlayers. The compositions of these two types of ferritic stainless steel are listed below. Both types have similar chromium concentrations, which would result in comparable coefficients of thermal expansion [125].

Table 1 Chemical compositions of 441SS and AFA (wt.%). AFA data is from [126]. 441 stainless steel data is from [127].

	C	Mn	P	S	Si	Cr	Ni
441SS	<b>≦</b> 0.03	<b>≦</b> 1.00	<b>≦</b> 0.04	<b>≦</b> 0.03	<b>≦</b> 1.0	17.5-19.5	<b>≦</b> 1.00
AFA	<b>≦</b> 0.015	<b>≦</b> 1.0	-	-	<b>≦</b> 1.0	19-21	-
	Nb	N	Ti	Al	La	Fe	
441SS	0.30+9* C-0.90	<b>≦</b> 0.03	0.10-0.50	-	-	Bal.	
AFA	-	-	-	5.0-6.0	0.06-0.12	Bal.	

The Ag-Ni double shear lap samples were prepared between 441SS and AFA substrates. Specifically, 400 mesh 99.8+% nickel powder (Alfa Aesar Inc; Tewksbury MA, USA) and Heraeus V737 polymeric vehicle were mechanically mixed in a 2:1 weight ratio. One pass of the paste was then printed on 240-grit SiC sandpaper polished stainless steel pieces using a 80-mesh screen containing 9.40 μm diameter stainless steel wires at 22° and 27 μm E80 emulsion (Sefar Inc; Depew NY, USA). After printing, the samples were held in a drying oven in air at 80°C for 10 minutes to remove solvent from the ink. Then the stainless steel pieces were surrounded by NiO powder and heated to ~830°C with 5°C/min heating rate and held for 2 hours in 20 sccm carbon gettered argon to sinter the nickel interlayer and further remove the residual carbon in the polymer. After cooling down to room temperature with 5°C/min cooling rate, 12.70 mm × 6.35 mm × 0.08 mm pieces of 99.95% pure silver foil was folded in half and placed between the nickel pads to assemble the double shear lap samples. Figure 3-3 shows the schematic of the double shear lap sample design, where AFA serves as the long bars, and 441SS acts as the side bars. The use of thin

stainless steel pieces enables surface printing. Consequently, the double shear lap sample design was chosen to minimize the likelihood of premature debonding caused by bending or misalignment during testing. The nickel printed stainless steel was pre-heated because this process can better remove the residual carbon than using two-step heating without cooling in between. The samples were heated to ~1025°C with 5°C/min heating rate and held for 30 minutes, while surrounded by NiO powder in 20 sccm of in carbon-gettered Ar gas before cooling to room temperature.

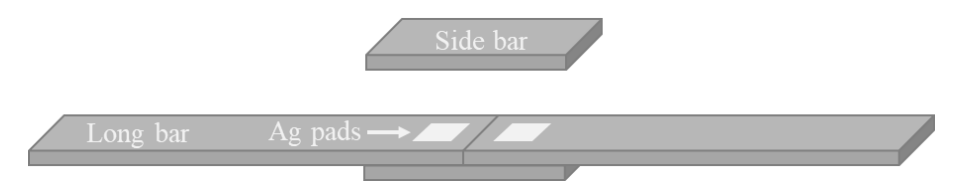


Figure 3-3 Schematic of the double shear lap sample design.

The Ag-Pt double shear lap samples were prepared between 441SS and AFA substrates. Specifically, 325 mesh 99.99% platinum powder (Surepure; Florham Park NJ, USA), 325 mesh 99.9% silver powder and Heraeus V737 polymeric vehicle were mechanically mixed in a 1:3:2 weight ratio. The paste was then printed on 240-grit SiC sandpaper polished stainless steel pieces. An 80-mesh screen containing 9.40 μm diameter stainless steel wires at 22° and 27 μm E80 emulsion (Sefar Inc; Depew NY, USA) was used. After printing, the samples were held in a drying oven at 80°C for 10 minutes to remove solvent from the ink. Then, 12.70 mm × 6.35 mm × 0.08 mm pieces of 99.95% pure silver foil (Surepure; Florham Park NJ, USA) was folded in half and placed between the isolated Pt pads to assemble the sample, with AFA as the long bars and 441SS as the side bars. The samples were heated to ~1025°C with 5°C/min heating rate and held for 30 minutes, while surrounded by NiO powder (to provide enough oxygen to oxidize any residual polymers in the Ag-25Pt paste) in 20 sccm carbon-gettered Ar gas before cooling to room temperature.

The Ag-CuO double shear lap samples were prepared between 441SS and AFA substrates. Specifically, silver-copper alloy powder of 325 mesh with 2.38 wt.%Cu (Morgan Advanced Materials – Wesgo Metals; Hayward CA, USA) was mixed with Heraeus V737 polymeric vehicle in 2:1 weight ratio. Two passes of the paste were printed on 240-grit sandpaper polished stainless steel using the same screen. After each pass printing, the samples were held in a drying oven at 80°C for 10 minutes to remove solvent from the ink. Then,  $4.76 \text{ mm} \times 4.76 \text{ mm} \times 0.08 \text{ mm}$  pieces of 99.95% pure silver foil were placed between the AgCu pads to make the double shear lap samples. This is the best preparation procedure we developed. Other procedures all produced worse samples including using the same amount of Ag as Ag-Pt samples (braze ran out of the gap), using only AgCu paste without Ag foil (two stainless pieces could not be brazed), and adjusting the Ag amount and AgCu paste passes (braze joint formation was bad). The experiments with the as-received AgCu composition failed, mainly due to the excessively good wetting condition. Upon heating, the filler alloy flowed out of the designated gap, resulting in an expanded wetting area and eventual failure. In this present work, the interlayer contained 2.38 wt.% Cu (approximately 4 mol.% CuO after complete oxidation). By diluting it with pure silver filler, the Cu concentration in the joint was reduced to ~1.2 mol.%. Although experiments were also conducted using a larger filler silver piece, the wetting performance was inadequate due to insufficient Cu content. The samples were heated to ~850°C and held for 2 hours, then heated to ~990°C and held for 0.1 hour in static air before cooling to room temperature. The heating and cooling rate was 5°C/min.

The Heraeus C8710 pure silver double shear lap samples were prepared between the 441SS and AFA substrates. Heraeus C8710 pure silver paste was printed through the same screen. Two passes of the paste were printed on the short stainless steel bars, with the first pass dried at 80°C for 10 minutes and the second pass wet. Only one pass of the paste was printed on both sides of

the long stainless steel pieces. The samples were then assembled in the double shear lap form and placed in the furnace. The samples were heated to  $\sim 850^{\circ}$ C and held for 10 minutes in air, and then cooled to  $\sim 750^{\circ}$ C for 10 hour annealing to densify the structure. The heating and cooling rate was 5°C/min.

The contact resistivity between the braze and the substrate was evaluated by measuring the resistance between substrates. The same type of stainless steel (either 441SS and 441SS or AFA and AFA) was used to prepare the resistance measurement samples. The samples were prepared following the same procedure as making the double shear lap samples, but with the use of 0.3 µm Al<sub>2</sub>O<sub>3</sub> polished and P-4000 grit sandpaper treated stainless steel substrates. The Heraeus C8710 double shear lap samples except that two passes (the first pass was dry and the second one was wet) were prepared on both types of 0.3 µm Al<sub>2</sub>O<sub>3</sub> polished and P-4000 grit sandpaper treated stainless steel substrates.

### 3.2 Air Annealing Treatment

The samples were subjected to air annealing in a static air furnace after being prepared. The heating and cooling rates were set at 5°C/min. The treatment temperature and dwelling time were selected according to the specific requirements of each sample.

### 3.3 Reduction-Oxidation Cycling Treatment

During the anticipated operational lifespan of SOFCs, intentional or accidental fuel supply shutdowns can occur [4, 128-131]. In such instances, the local anode environment changes from reducing atmosphere, which is created by the fuel, to an oxidizing atmosphere, which is created by air. Such atmosphere change can induce chemical reactions, microstructural alterations, and performance degradation in the brazed joints. These chemical changes may also lead to the

formation of defects, including cracks and voids, potentially resulting in seal failure and cell malfunction. Additionally, operation shutdowns can cause temperature fluctuations that may further jeopardize the integrity of the cell components. Therefore, experiments were designed to mimic conditions which the samples may experience in the events of shutdowns. It is worth noting that SOFCs generally experience rare fuel shutdowns throughout their lifespan. To assess durability, I conducted 25 cycles involving 12 hours of oxidizing and 12 hours of reducing conditions. Notably, this cycling number surpasses those of similar experiments, which typically utilized fewer than 10 cycles [129, 132-137]. Only a limited number of studies have explored higher cycle counts [138].

The samples were subjected to reduction-oxidation (redox) cycling treatment to test the durability after being prepared. All of the samples used in the redox cycling treatment were initially in the as-produced state prior to the experiment. The mechanical and electrical measurement samples were enclosed in a sealed alumina tube and placed in a furnace. The temperature increased to 650°C at a rate of 5°C/min, and the samples were held at this temperature for approximately 600 hours. During the isothermal aging, the atmosphere alternated between air and 4% hydrogen (nitrogen balanced) every approximately 12 hours. After completing each oxidizing process, the exhaust was sealed, and the air inside the tube was evacuated by running the pump for 30 minutes. Subsequently, 4% hydrogen was introduced to fill the tube until reaching atmospheric pressure. The pumping process was repeated twice, with the first pumping lasting for 10 minutes and the second pumping for 5 minutes, while the venting process remained consistent to ensure the pressure reached atmospheric levels. After each reducing process, the 4% hydrogen was removed by running the pump for 30 minutes, and the air was vented by opening the exhaust. After

undergoing 25 oxidation-reduction cycles, the samples were cooled to room temperature at a rate of 5°C/min.

## 3.4 Extremely Rapid Thermal Cycling Treatment

The samples underwent rapid thermal cycling treatment to assess their durability. To eliminate the impact of nickel oxidation, all samples, including Ag-Ni, Ag-Pt, and Ag-CuO, were initially air annealed at 650°C for 300 hours. Subsequently, the samples were positioned on a movable stage within the rapid thermal cycling test furnace. The stage moved between the heating chamber and the open air to facilitate thermal cycles. Within the heating chamber, the heating and cooling rate was set at 25°C/min. As the temperature dropped to approximately 320°C, the stage descended to the open air, allowing the samples to cool down with the assistance of a fan. After reaching room temperature, the stage ascended back to the heating chamber. This process was repeated for 300 cycles to evaluate the rapid thermal cycling durability. Figure 3-4 shows the temperature profile of the samples.

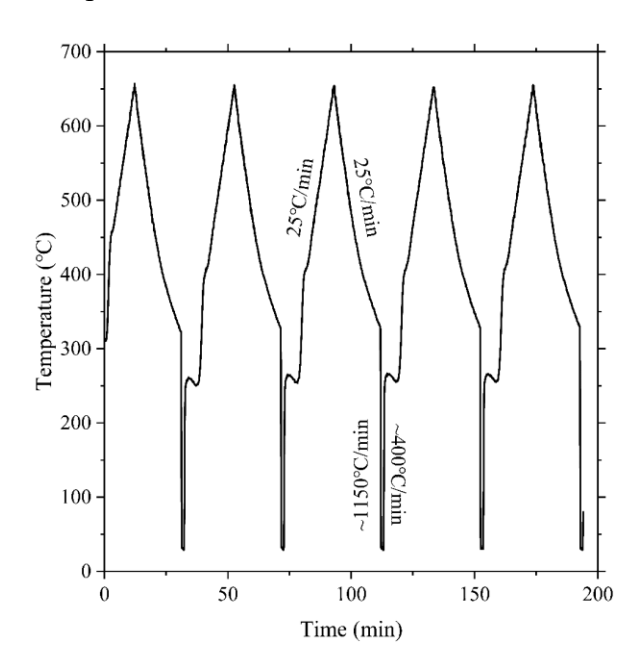


Figure 3-4 Temperature profile of the rapid thermal cycling test. Note, these are the thermocouple temperatures. Due to their thermal mass, the heating/cooling rates of the substrates are likely lower.

It is worth noting that SOFCs may experience more thermal cycles than redox cycles, especially in automotive applications. In such conditions, rapid start-up is necessary, leading to high heating rates. The presented work utilized a similar rate at high temperatures as in previous research [139]. Figure 3-5 shows the temperature profile. However, in the low-temperature region, the cooling rate was more aggressive. In the literature, similar rapid thermal cycling tests have been conducted, with some using rates lower than 50°C/min [140, 141], while others used rates larger than 300°C/min [142, 143]. Therefore, considering the combined effect of the mild rate of 25°C/min at high temperatures and the aggressive ~1000°C/min rate at low temperatures, the entire rapid thermal cycling test can be described as aggressive.

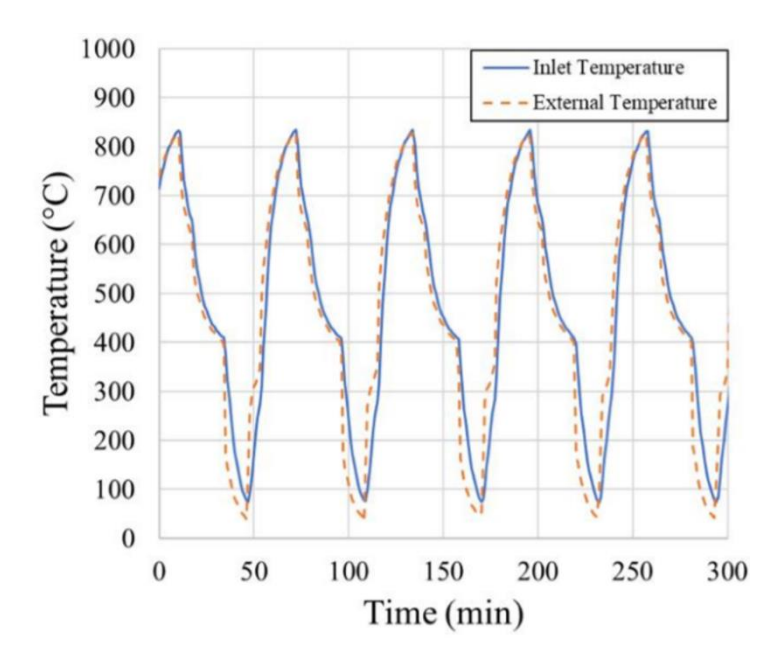


Figure 3-5 Temperature profile of a similar rapid thermal cycling durability test in previous research [139].

## 3.5 Bonding Strength Measurement

The bonding strength of both the silver circuit to the alumina substrate and the braze joint between stainless steel was assessed by the mechanical test to determine their resistance to external forces. The evaluation was performed using a mechanical test machine (SFM-20, United Testing

Systems, Inc.) equipped with a 1000-pound load cell. Adjustable clamps were utilized to align the wedge-shaped load grips along a long iron sheet, and no strain gauge was employed. The samples were subjected to a tensile testing process at a load rate of approximately 37.5µm/min, and the maximum force applied during the test was recorded. Figure 3-6 shows the tensile sample between the grips during the mechanical test.

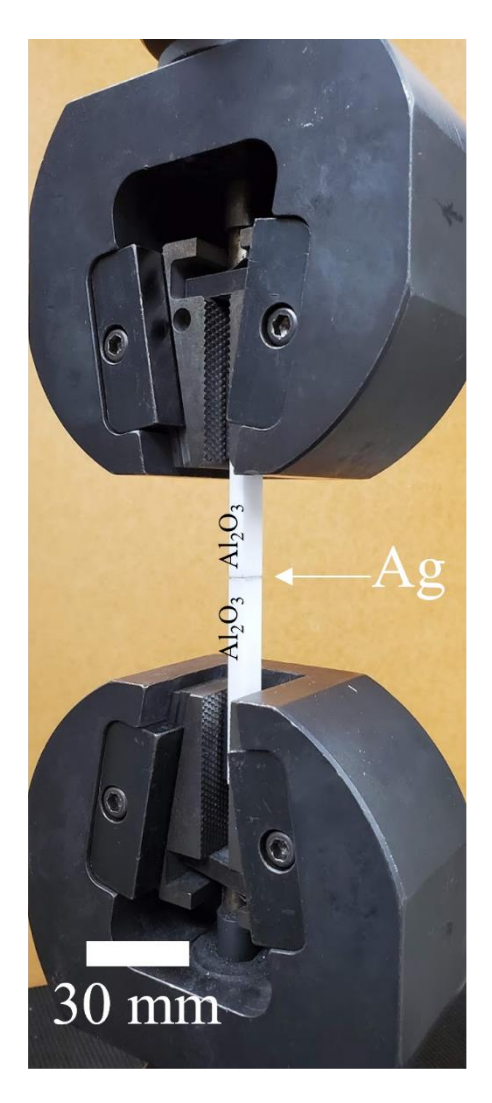


Figure 3-6 A tensile test sample between the grips during the mechanical test, from previously published paper [93].

The tensile strength was determined using the following equation:

$$\sigma_{tensile} = \frac{F_{max}}{A}$$

Here,  $\sigma_{tensile}$  denotes the tensile strength of the tensile test samples.  $F_{max}$  denotes the recorded maximum force. A corresponds to the brazing area of the tensile test sample.

Figure 3-7 shows a double shear lap sample between the grips during the mechanical test.

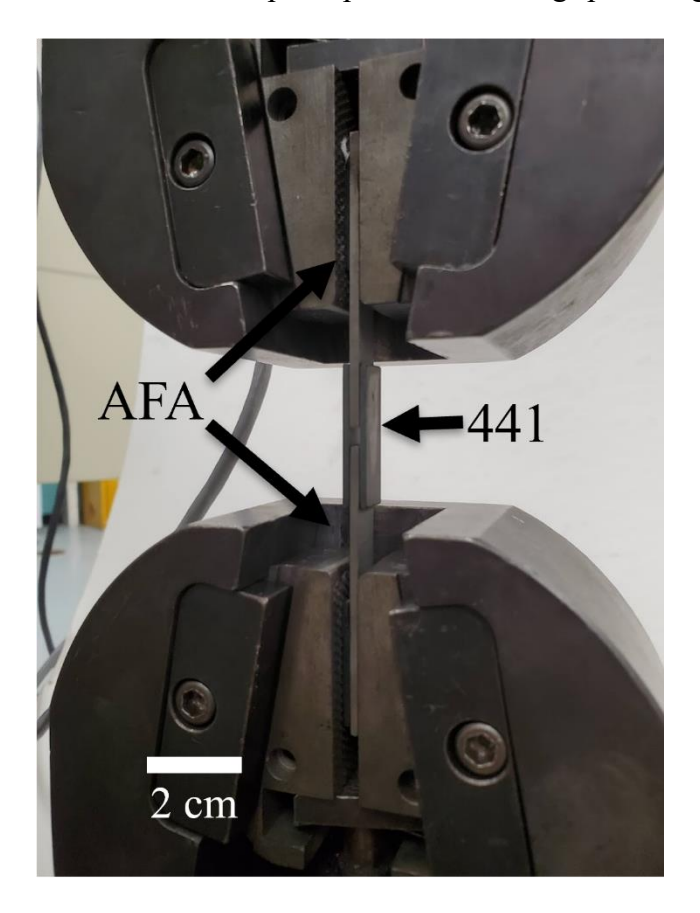


Figure 3-7 A double shear lap sample between the grips during the mechanical test.

The shear strength of the sample was determined using the following equation:

$$\sigma_{shear} = \frac{F_{max}}{A_a + A_b}$$

Here,  $\sigma_{shear}$  denotes the shear strength of the double shear lap samples.  $A_a$  and  $A_b$  are the two areas of the fractured silver pads in the tensile test sample. The specimens were ranked in ascending order of strength as 1, 2, 3, ..., j, j+1, ..., N, where N is the total number of samples. The survival probability of the jth sample is determined using the formula  $S_j = 1 - \frac{j-0.3}{N+0.4}$  [144].

The Weibull plot was generated by plotting the negative double log reciprocal survival probability on the y-axis and the logarithm of the strength on the x-axis.

### 3.6 Resistance Measurement

### 3.6.1 Silver-Based Circuit Sheet and Contact Resistance Measurement

Sheet resistivity measurements were performed using the van der Pauw method [145] on Ag-Ni, Heraeus C8710 and DAD-87 circuits produced with the geometric layout shown in Figure 3-8(a). This circuit geometry ensured that the "point contacts" around the edge of the sample assumed in the van der Pauw technique derivation could be met while ensuring ample room to secure the external leads.

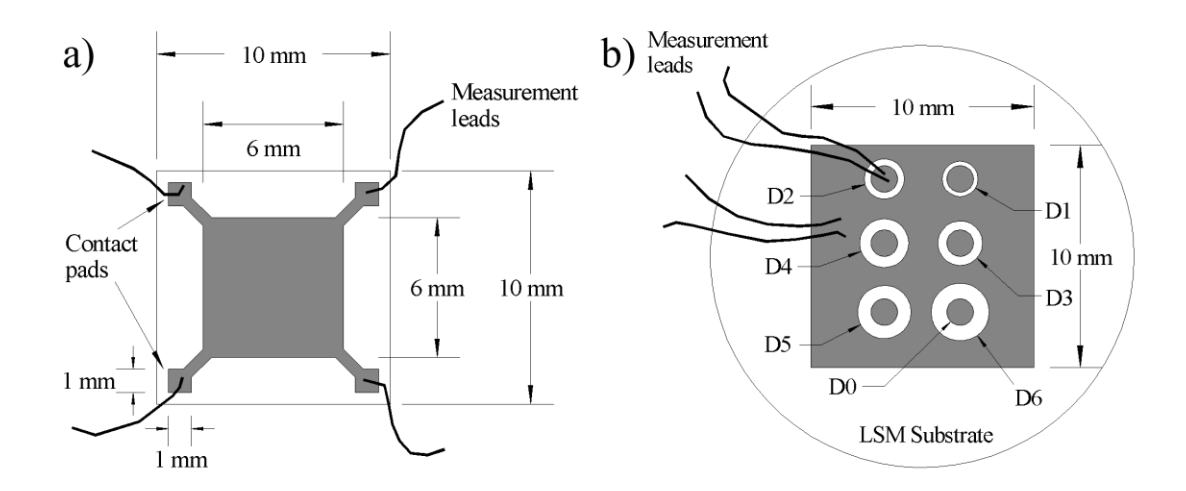


Figure 3-8 Test sample patterns used for the sheet resistivity (a) and contact resistivity (b) measurements. In (b), the center contacts all have the same diameter of D0 = 1.2 mm, and the other indicated diameters are D1 = 1.6 mm, D2 = 1.8 mm, D3 = 2.0 mm, D4 = 2.2 mm, D5 = 2.4 mm, and D6 = 2.6 mm.

The sheet resistivity measurement system included a current source, a voltmeter, a switch system and a temperature regulator. Specifically, the system included a 2400 Series Source Meter (Keithley Instruments, Cleveland OH, USA) to apply current to the specimen, a 2182 Nanovoltmeter (Keithley Instruments, Cleveland OH, USA) to measure the voltage and the resistance of a resistance temperature detector (Omega Engineering, Norwalk CT, USA) used to

help determine the sample temperature, an iSeries CNi32 temperature controller with PID control (Omega Engineering, Norwalk CT, USA) used for accurate temperature regulation, and a 7002 switch system (Keithley Instruments, Cleveland OH, USA) with a 7012-2 4×10 Matrix Card (Keithley Instruments, Cleveland OH, USA) used to connect the contacts to the appropriate equipment.

Contact resistivity measurements were performed using the Circular Transfer Length Method (CTLM) deemed superior to the linear transfer length method (LTLM) by Klootwijk and Timmering [146]. Specifically, as shown in Figure 3-8(b), current was forced to travel from a central pad, across a circuit-LSM interface, through the LSM over a distance controlled by the printed gap spacing, across a second circuit-LSM interface and through the outer portion of the printed circuit. A 4-point probe method was used to avoid contributions from test lead contact resistances. This technique allowed the circuit-LSM contact resistance to be distinguished from resistance caused by electronic transport through the LSM.

The CTLM consists of passing a current of fixed magnitude through a center contact of diameter D0, while monitoring the voltage drop between the center contact and the ground plane [146]. The relationship between the total measured resistance, R<sub>M</sub>, and the dimensions for the smallest gap pattern shown in Figure 3-8(b) is given by:

$$R_{M} = \frac{R_{SH}}{2\pi} \left[ ln \left( \frac{D1}{D0} \right) + \frac{2}{k} \left( \frac{1}{D0} + \frac{1}{D1} \right) \right]$$

where,  $R_{SH}$  is the sheet resistance of the LSM substrate under the contact, k is a constant equal to the square root of the sheet resistance of the LSM substrate over the contact resistivity, and D0 and D1 correspond to the diameters indicated in Figure 3-8(b). A Taylor series approximation can be used to find a correction factor, c, can be used to transform the above equation to a linear relationship between the measured resistance and the gap spacing [147, 148]; specifically:

$$R_M \approx \frac{R_{SH}}{2\pi D0} \left[ (D1 - D0) + \frac{4}{k} \right] c$$

where the correction factor is:

$$c = \left[\frac{D0}{D1 - D0}\right] ln\left(\frac{D1}{D0}\right)$$

The correction factor accounts for current crowding near the contacts. Using this approach, it is necessary to measure the gap-spacing between the inner-circle and the outer ring to calculate the final contact resistivity. Image analysis software ImageJ was used to determine the gap spacing which makes use of spatial calibration to set the scale for gap-spacing measurement. The specific contact resistance was then found by a linear fit to the  $R_M$  vs gap spacing data, where the y-intercept corresponds to a zero gap-spacing (from which twice the contact resistance of the circuit-LSM can easily be found without concern for how much of the underlying LSM volume participates in the bulk LSM electron conduction pathway).

Figure 3-9(a) and Figure 3-9(b) show the DAD-87 on alumina substrate sheet resistance sample and the DAD-87 on LSM contact resistance sample, respectively. Figure 3-9(c) shows the contact resistance sample with wire connection before the measurement.

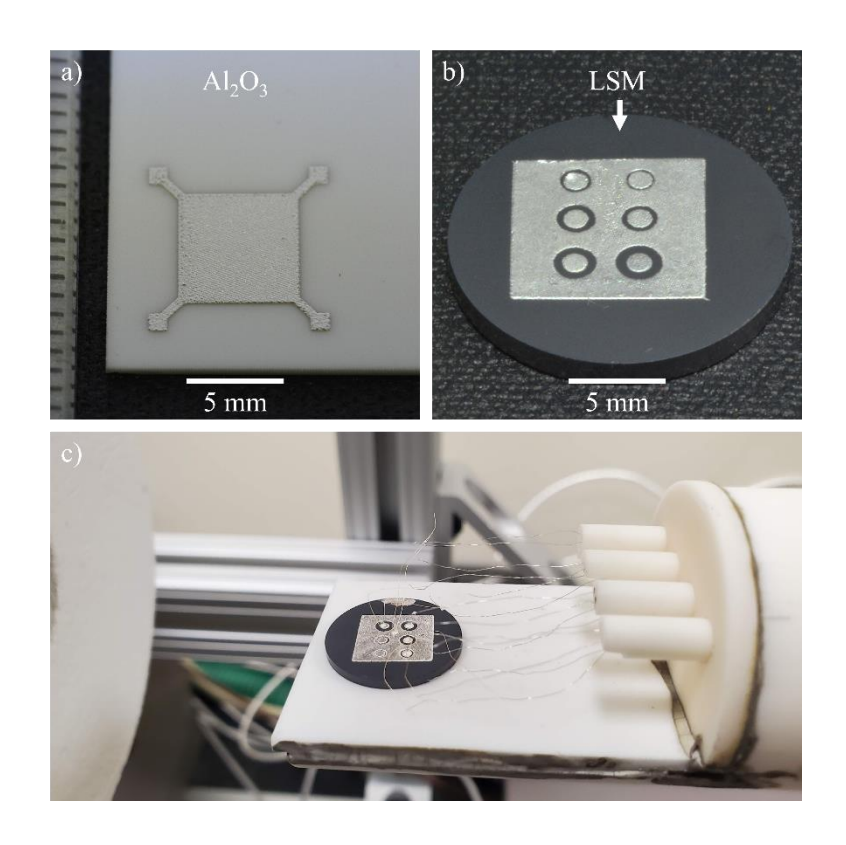


Figure 3-9 (a) DAD-87 on alumina sheet resistance sample photo, (b) DAD-87 on LSM contact resistance sample photo, and (c) contact resistance sample with wire connection before the measurement.

### 3.6.2 Silver Based Braze Contact Resistance Measurement

The interfacial contact resistance was determined to evaluate the resistivity across the interface between braze and the stainless steel. To prepare the resistance measurement samples, the stainless steel surface was treated by sequentially grinding with 240-grit, 600-grit, and 1200-grit SiC sandpaper to remove any oxide scale. After the surface cleaning, four copper wires were affixed to the surface using silver colloidal (Ted Pella; Redding CA, USA). Two wires were attached to the back sides of the samples, which were connected to a Keithley 2400 SourceMeter. The remaining two wires were attached to the bonding sides of the samples, which were connected to a Keithley 2182 Nanovoltmeter. Figure 3-10 shows the resistance sample with four wires connected to the surface. All the wires were connected to 1200-grit polished surfaces. This design is different from the circuit design, as obtaining reliable silver-based circuits on stainless steel

substrates is challenging. The reaction between the interlayer and the stainless steel substrate can result in a rough surface for the silver-based circuits. Consequently, the sandwich structure was chosen for the resistance evaluation. This design creates silver joints between two stainless steel pieces. Therefore, the measured resistance between the stainless steel pieces comprises the combination of resistance across the joint-steel interfaces, along with the assumed negligible resistances through the bulk of the silver joints and the bulk of the stainless steel substrates. The silver joint is ~200  $\mu$ m for the samples, with the contact resistivity of ~10<sup>-8</sup>  $\Omega$ •cm<sup>2</sup> [149]. The AFA substrate is initially 1 mm thick. After surface polishing, assuming no significant thickness change, it contributes approximately ~10<sup>-5</sup>  $\Omega$ •cm<sup>2</sup> to the total contact resistivity [126]. 441 stainless steel contributes similar ~10<sup>-5</sup>  $\Omega$ •cm<sup>2</sup> to the total contact resistivity [150].

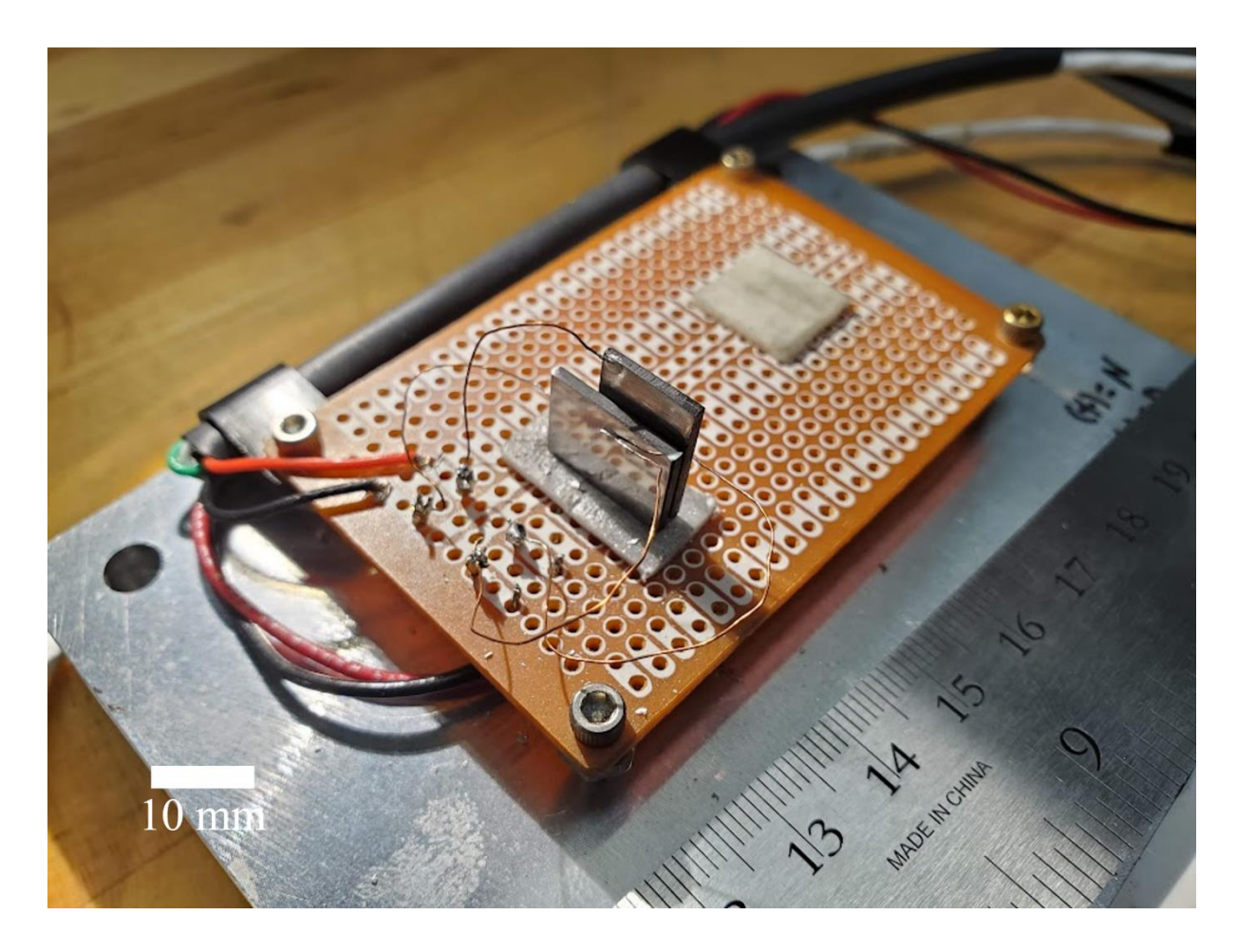


Figure 3-10 Resistance samples measured with 4-point method. All the brazing surfaces were treated uniformly to P4000 grit after polishing with 0.3  $\mu$ m Al<sub>2</sub>O<sub>3</sub> agent. The wires were connected to 1200-grit polished surface.

Initially, a 200mA current was applied to measure the voltage between the bonding sides and estimate the resistance. Subsequently, a sweeping current signal was generated from the SourceMeter, and the corresponding voltage was measured. The current signal was adjusted to ensure the voltage fell within the high precision range. The resistance was determined by calculating the slope of the voltage-current line. The contact resistivity was determined by dividing the resistance with the brazing area, which is 0.4 cm<sup>2</sup>. It is worth noting that all samples exhibited ohmic behavior, characterized by straight voltage-current lines.

## 3.7 Scanning Electron Microscopy

For Scanning Electron Microscopy (SEM) analysis, the braze samples were prepared by cutting them with a low-speed diamond saw to expose the cross-sectional area. Subsequently, the samples were mounted in epoxy (Epofix, Buehler Inc.; Lake Bluff, IL). To achieve the desired surface finish, the samples underwent grinding using SiC sandpaper ranging from 240 to P4000 grit. Finally, they were polished using 0.3 µm and 0.05 µm Al<sub>2</sub>O<sub>3</sub> polishing agent. To ensure optimal electron conductivity, a platinum sputter coating process was employed. The samples were coated with platinum at a current of 30 mA for 20 seconds using a Desk II sputter Coater (Denton Vacuum, LLC), resulting in a surface coating of approximately 5 nm thickness. Following the platinum coating, the samples were characterized using a MIRA3 SEM (Tescan, Inc.) to obtain back-scattered electron images. Additionally, an EVO LS25 SEM (Zeiss, GmbH) was utilized for Energy Dispersive X-Ray Spectroscopy (EDS) analyses.

## 4 Ag-Ni Circuits on Alumina

#### 4.1 Introduction

The utilization of nickel interlayers to enhance silver wetting on ceramic substrates has been established in previous studies. However, the performance of silver-nickel circuits remains unclear, particularly for applications in Solid Oxide Fuel Cells, Solid Oxide Electrolysis Cells, and other high-temperature devices that require reliable adhesion and conductivity for optimal energy efficiency. Therefore, this chapter focuses on the analysis of the bonding strength, sheet resistivity, contact resistivity, and microstructure of silver-nickel circuits, comparing their performance with commercially available silver pastes. The contents in this chapter is from a previously published paper in *Scripta Materialia* [93].

The bonding strength was assessed through mechanical testing of samples, measuring the fracture behavior under quasistatic conditions. Sheet resistivity was evaluated by fabricating circuits on insulating alumina substrates and measuring the sheet resistance. Contact resistivity was determined by creating circuits on conductive LSM substrates and using the Circular Transfer Length Method, as detailed in the Experimental Methods chapter, to measure the contact resistance between the circuit and the LSM substrate. Microstructural analysis was conducted by cutting the samples to reveal cross-sections and examining the polished surfaces under SEM.

## **4.2** Tensile Strength

The evaluation of tensile strength in the silver circuit on alumina substrate was carried out using a series of carefully prepared test samples. Two alumina bars measuring 5 mm × 10 mm × 60 mm were connected in a head-to-head configuration, with the 5 mm × 10 mm surfaces in contact. These samples were subjected to systematic tensile testing to assess their mechanical performance and determine the ultimate tensile strength. The tests were conducted in batches to ensure an

understanding of the statistical failure behavior. Table 2 shows the tensile strength values of air annealed Heraeus C8710, DAD-87, as-produced Ag-Ni, and air annealed Ag-Ni samples. In each group, the samples exhibited varying strength values attributed to differences in printing, bars alignment, or other variations in the manufacturing process. The dissimilar strength levels among the groups can be attributed to the distinct nature of bonding. In the case of Heraeus C8710 and DAD-87 samples, the silver joint displayed weak integrity, resulting in fracture occurring at the silver-alumina interfaces and within the silver itself upon testing. However, for Ag-Ni samples, the fractures predominantly occurred at the silver-alumina interfaces while the silver joint maintained its integrity.

Table 2 The tensile strength values of Heraeus C8710, DAD-87, and Ag-Ni samples.

	Sample 1	Sample 2	Sample 3	Sample 4
10-hour air annealed Heraeus C8710	0.6 MPa	0.7 MPa	1.7 MPa	2.4 MPa
10-hour air annealed DAD-87	1.3 MPa	1.4 MPa	1.9 MPa	N/A
As-produced Ag-Ni	9.0 MPa	10.0 MPa	11.4 MPa	15.8 MPa
250-hour air annealed Ag-Ni	25.0 MPa	29.6 MPa	30.9 MPa	N/A

The failure strength is considered to follow the Weibull distribution, which can be described as

$$S = exp\left[-\left(\frac{\sigma}{\sigma_0}\right)^m\right]$$

Here, S is the survival probability,  $\sigma$  is the failure strength,  $\sigma_0$  is a normalizing parameter, m is a shape factor, usually referred to as the Weibull modulus [144]. The aforementioned equation can be transformed into

$$lnln\frac{1}{S} = mln\sigma - mln\sigma_0$$

Once a batch of samples are tested, the survival probability of each sample can be determined by ranking them in ascending order of strength as 1, 2, 3, ..., j, j+1, ..., N, where N is the total number of samples. The survival probability of the jth sample is determined using the formula  $S_j = 1 - \frac{j-0.3}{N+0.4}$  [144].

Figure 4-1 illustrates the tensile fracture stress Weibull plots, highlighting the superior adhesion strength exhibited by the Ag-Ni circuits on sapphire compared to commercially available Ag circuit pastes. In fact, despite the oxidation of some Ni particles in the Ag-Ni circuits after extended exposure (10 hours) to high temperatures (750°C) in ambient air, the increased oxygen dissolution into the silver results in a stronger interface between Ag and sapphire [78]. The measured data points enable the estimation of the strength distribution, providing the equation for survival probability versus strength. Consequently, the strength at a given survival probability can be determined. Specifically, the annealed C8710, annealed DAD-87, as-produced Ag-Ni, and annealed Ag-Ni circuits on sapphire have 99% Weibull survival probabilities of 0.06, 0.9, 3.7, and 17.2 MPa, respectively. The silver joint thickness of the samples was recorded and indicated on the data points. It was observed that the joint fracture occurred at the silver-alumina interface, indicating that the thickness of the joint does not have a significant impact on its strength as shown by samples with multiple thicknesses appearing on the same Weibull curve in Figure 4-1.

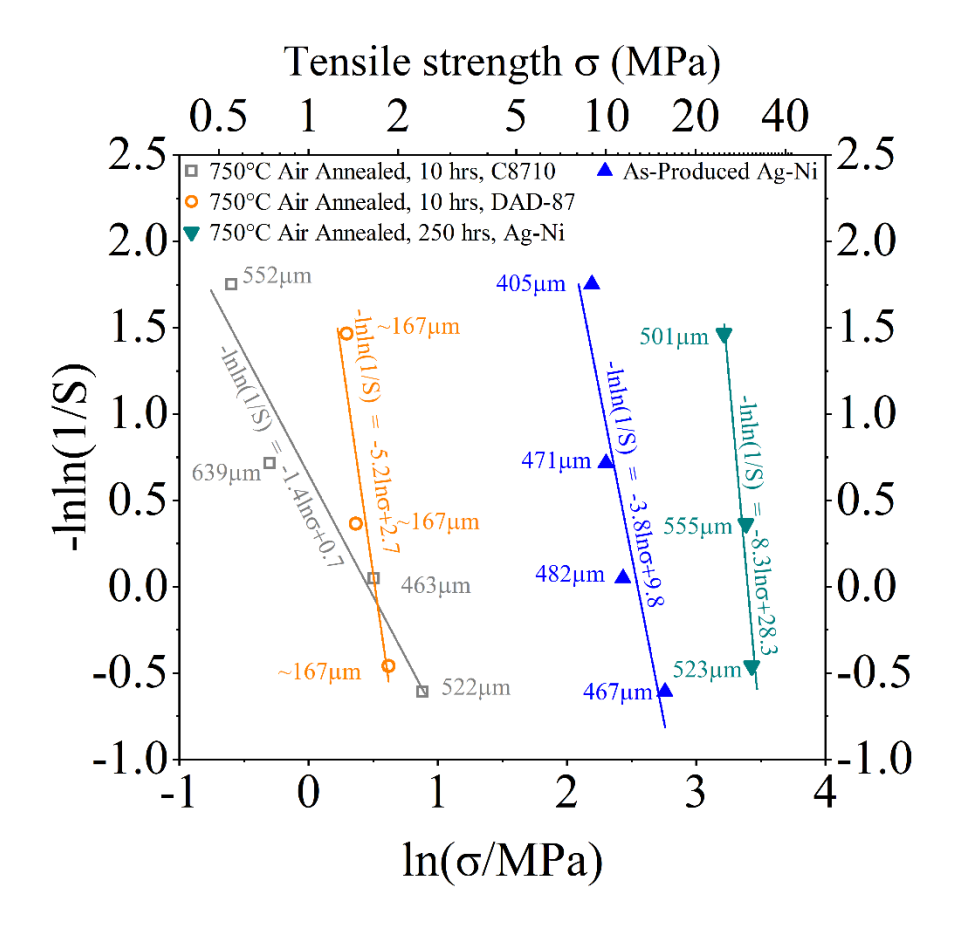


Figure 4-1 Weibull plot of 10-hour air annealed Heraeus C8710, 10-hour air annealed DAD-87, as-produced Ag-Ni, and 250-hour air annealed Ag-Ni samples. Reproduced from [93] with permission via a CC-BY license.

### 4.3 Sheet and Contact Resistivity

Figure 4-2 shows the sheet resistivity of Heraeus C8710, DAD-87, and Ag-Ni circuits on alumina substrates in as-produced and air annealed states at different temperatures. The as-produced C8710 and DAD-87 circuits exhibited higher sheet resistivity compared to the Ag-Ni circuits. However, following air annealing, the sheet resistivity of C8710 and DAD-87 reduced due to microstructure densification, approaching that of the as-produced Ag-Ni sample. Although the sheet resistivity of the Ag-Ni circuits increased due to nickel oxidation after air annealing, it still outperformed commercially available counterparts in the as-produced state. For reference, the temperature-dependent sheet resistivity of pure silver [149, 151] and pure nickel [79, 149] is

included. Notably, the sheet resistivity of both as-produced and air-annealed Ag-Ni circuits is comparable to that of pure silver, indicating excellent electrical conductivity of the circuit.

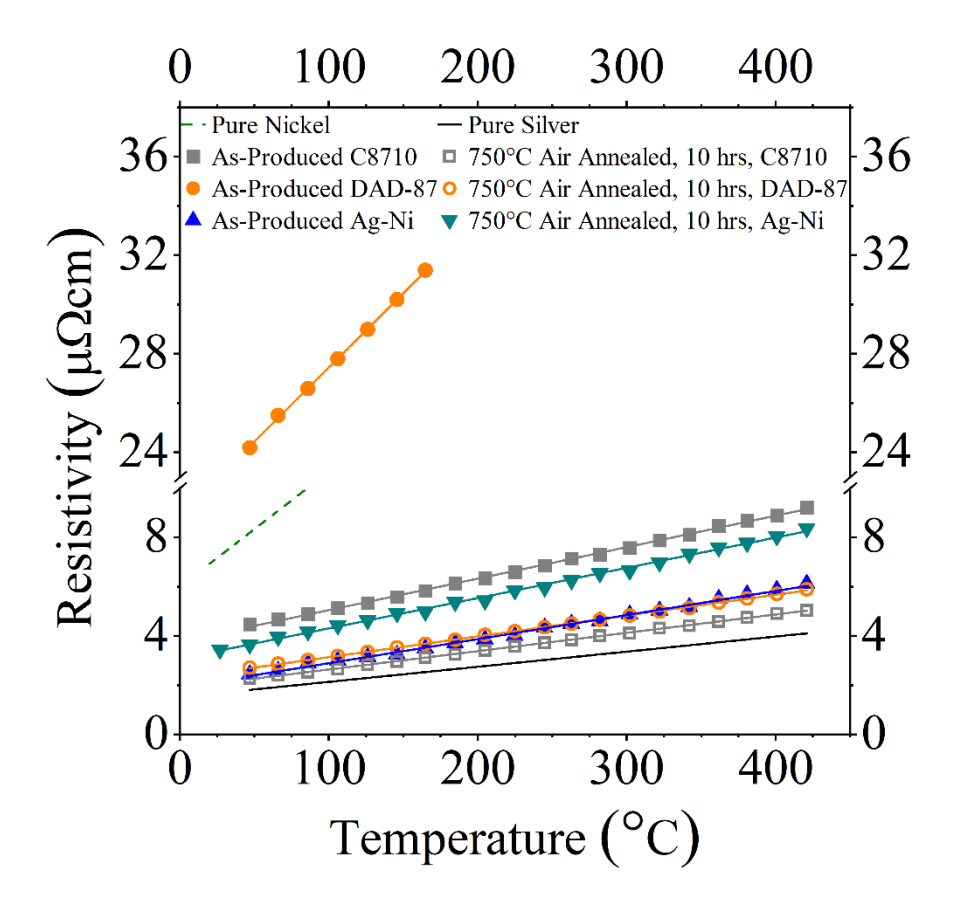


Figure 4-2 Sheet resistivity of Heraeus C8710, DAD-87, Ag-Ni silver circuits in as-produced and air annealed states at different temperatures. Reproduced from [93] with permission via a CC-BY license.

Figure 4-3 shows the contact resistivity of 10-hour air annealed Heraeus C8710, 10-hour air annealed DAD-87, as-produced Ag-Ni, 10-hour air annealed Ag-Ni, and 250-hour air annealed Ag-Ni circuits on polycrystalline La<sub>0.8</sub>Sr<sub>0.2</sub>MnO<sub>3-x</sub> substrates. For all the samples, the contact resistivity increased to the highest near ~60°C and then decreased. This peak in the resistivity curve is attributed to the ferromagnetic-paramagnetic transition occurring at the LSM Curie temperature. Hassini *et al.* [152] reported a Curie temperature of ~60°C for the La<sub>0.8</sub>Sr<sub>0.2</sub>MnO<sub>3-x</sub> substrate used here. Among the samples, the air-annealed Heraeus C8710 circuits exhibited the lowest contact

resistivity, while the air-annealed DAD-87 circuits showed the highest. The as-produced Ag-Ni circuits demonstrated relatively high contact resistivity at lower temperatures. Following air annealing, the contact resistivity decreased in the low-temperature range but increased in high-temperature regions. The resistivity at high temperatures remained stable, as the annealing time did not significantly alter the resistivity.

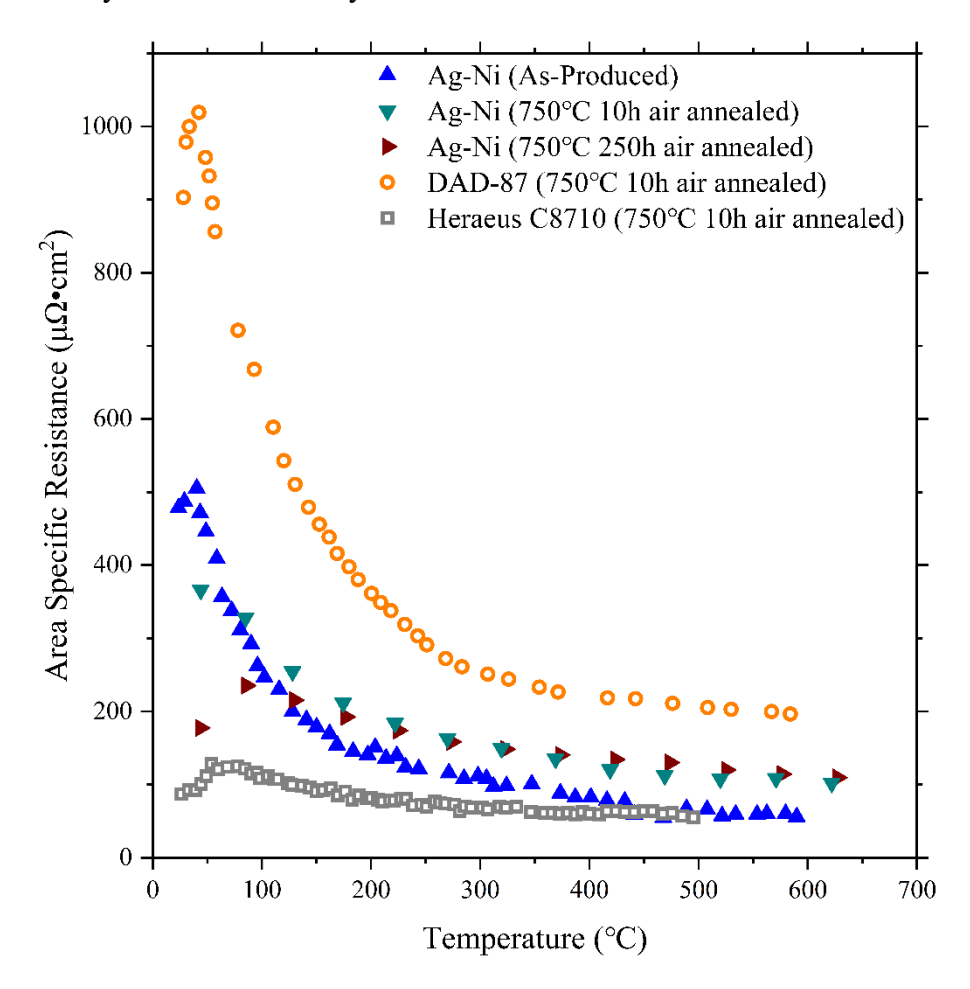


Figure 4-3 The temperature-dependent contact resistivity of various circuits on polycrystalline  $La_{0.8}Sr_{0.2}MnO_{3-x}$  substrates. Reproduced from [153] with permission from the Electrochemical Society.

## 4.4 Microstructure Analysis

Figure 4-4 shows the representative back-scattered electron (BSE) scanning electron microscopy (SEM) cross-section images of Heraeus C8710, DAD-87, and Ag-Ni circuits in asproduced and air annealed states. In the as-produced state, Heraeus C8710 and DAD-87 exhibited porosity with visible individual silver grains after preparation following the manufactures' directions. In comparison, the Ag-Ni circuit displayed a denser microstructure compared to commercially available counterparts. Following a 10-hour air annealing process, both Heraeus C8710 and DAD-87 exhibited increased density; however, some pores were still observed in the microstructure. The Ag-Ni circuit underwent microstructural changes due to nickel oxidation, yet it maintained a dense structure.

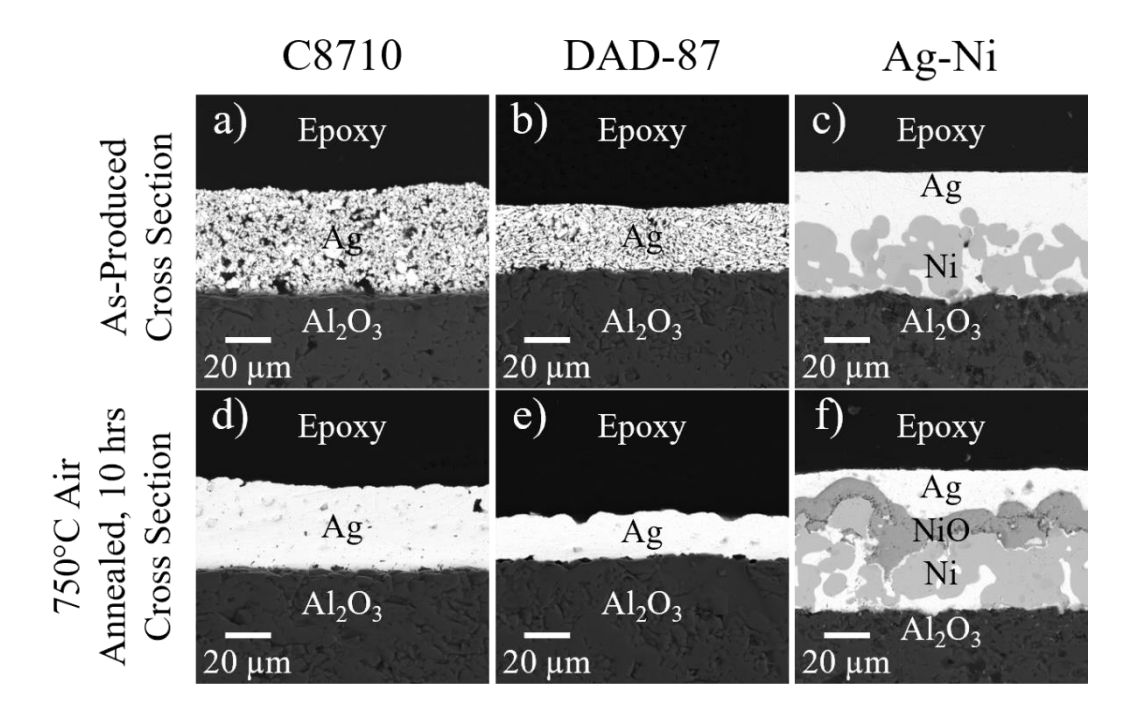


Figure 4-4 Representative back-scattered (BSE) scanning electron microscopy (SEM) cross-section images of as-produced (a) Heraeus C8710, (b) DAD-87, (c) Ag-Ni, and 10-hour air annealed (d) C8710, (e) DAD-87, and (f) Ag-Ni circuits on alumina. Reproduced from [93] with permission via a CC-BY license.

#### 4.5 Discussion

This chapter evaluated the performance of Ag-Ni circuits on alumina substrates and compared their mechanical and electrical characteristics with commercially available silver pastes Heraeus C8710 and DAD-87.

The Ag-Ni samples exhibit higher tensile strength on alumina substrates for two main reasons. Firstly, during the preparation of Ag-Ni samples, the high-temperature melting process for silver ensures a dense microstructure. In contrast, commercially available pastes contain silver particles that may not be fully densified, resulting in a less dense microstructure. This difference allows the silver in Ag-Ni samples to retain its integrity better than the commercial counterparts. Secondly, at the silver-alumina interfaces, the work of adhesion between nickel and the ceramic is higher than that between silver and the ceramic, as observed experimentally [154] and computationally [78]. This enhanced cohesion of silver and improved interfacial bonding contributes to the superior mechanical performance of Ag-Ni samples. Additionally, oxidation introduces more oxygen to the interface, further enhancing the bonding.

Regarding sheet resistivity and contact resistivity, the Ag-Ni samples exhibit comparable values to commercial products. This similarity can be attributed to the fact that the Ag-Ni samples possess a dense microstructure in their as-produced state, while the commercial products have a porous structure. The porous structure of commercial products leads to increased electron scattering and higher resistance. However, after air annealing, the commercial products undergo densification, which helps reduce resistance, while the nickel in the Ag-Ni samples oxidizes, leading to an increase in resistance. As a result, the Ag-Ni samples and commercial products demonstrate comparable resistance properties.

# 4.6 Summary

This study introduces a novel approach for creating electrically conductive circuits on ceramics using a nickel interlayer to enhance the wetting of liquid silver. The Ag-Ni circuit demonstrates comparable low sheet resistivity ( $\sim 10^{-6} \,\Omega$ •cm) and contact resistivity ( $\sim 10^{-4} \,\Omega$ •cm²) on LSM substrates, similar to Heraeus C8710 and DAD-87. Moreover, the Ag-Ni circuit exhibits superior tensile adhesion, around 10 times stronger, on alumina substrates, accompanied by a denser microstructure. These findings suggest the potential utility of Ag-Ni in various high-temperature circuit/current collector applications, including Solid Oxide Fuel Cells, Solid Oxide Electrolysis Cells, and more.

The performance of the Ag-Ni PIDWAS technique on alumina-protected stainless steel will be further evaluated in the subsequent chapter.

## 5 Performance and Durability of Ag-Ni Braze Joints to Dissimilar Stainless Steels

#### 5.1 Introduction

The individual Solid Oxide Fuel Cell consists of the anode, the cathode, and the electrolyte [3, 4]. To achieve higher power output, the cells need to be stacked, which requires durable, stable, and electrically conductive interconnectors between two cells on both the anode and the cathode sides for high temperature applications [155, 156]. To achieve this, brazing techniques have been employed to seal the stack [65, 72, 93, 157, 158].

The successful application of the Ag-Ni PIDWAS brazing technique between 441 stainless steel and YSZ ceramic has been demonstrated in Figure 2-4. 441 stainless steel is often utilized in Solid Oxide Fuel Cells and Solid Oxide Electrolysis Cells because of its matching coefficient of thermal expansion with YSZ (25-750°C: CTE<sub>441SS</sub>=12 ppm/K [159], CTE<sub>YSZ</sub>=9 ppm/K [86]). This CTE match reduces the likelihood of stress-induced cracks. However, the presence of unstable chromium oxide on 441 stainless steel can potentially degrade the performance of the SOCs. To address this issue, aluminum-alloyed stainless steel has been explored as a replacement for 441SS. Consequently, the performance of the Ag-Ni PIDWAS brazing technique on such aluminum-containing stainless steel alloys needs to be assessed.

This chapter analyzes the mechanical and electrical performance, as well as the air annealing, redox and rapid thermal cycling durability, of Ag-Ni brazes applied to aluminum-containing stainless steel. The contents of this chapter were not published before this dissertation was submitted.

## **5.2 Microstructure Analyses**

## 5.2.1 <u>As-Produced Samples</u>

Figure 5-1(a) shows the BSE SEM image of the whole as-produced AFA|Ni|Ag|Ni|441 braze cross-sectional area. The braze joint is dense and crack-free. The molten silver is well-constrained by the porous nickel interlayers.

Figure 5-1(b) shows the BSE SEM image of a representative AFA|braze interfacial area and an energy dispersive x-ray spectroscopy (EDS) line scan in the as-produced sample. This interface consists of multiple layers, specifically: 1) the base AFA (Note, the Cr<sub>2</sub>O<sub>3</sub> spike at ~12 microns in the EDS spectra is a rouge chromia pocket formed in the AFA stainless steel), 2) an Al<sub>2</sub>O<sub>3</sub> layer, 3) a Ni-Al reaction layer, and finally 4) pure Ag. As marked by the translucent green bar, there is a long Al tail into the Ni, but not into the Fe-Cr layer on the other side of the Al<sub>2</sub>O<sub>3</sub> layer, suggesting that the nickel layers were able to getter some, but not all, of the alumina which segregated out of the AFA.

Figure 5-1(c) shows the BSE SEM image of a representative braze|441 interfacial area and an EDS line scan in the as-produced sample. This interface consists of the porous nickel interlayer, nickel-iron-chromium interdiffusion region, and 441 stainless steel substrate. As was observed before [65], the interdiffusion between nickel and the 441 stainless steel result in a strong metallurgical bond. A chromium peak is observed in the EDS spectra as labeled by the translucent green bar and the arrow, which is possibly due to the slight amount of residual chromia that was not completely removed during polishing.

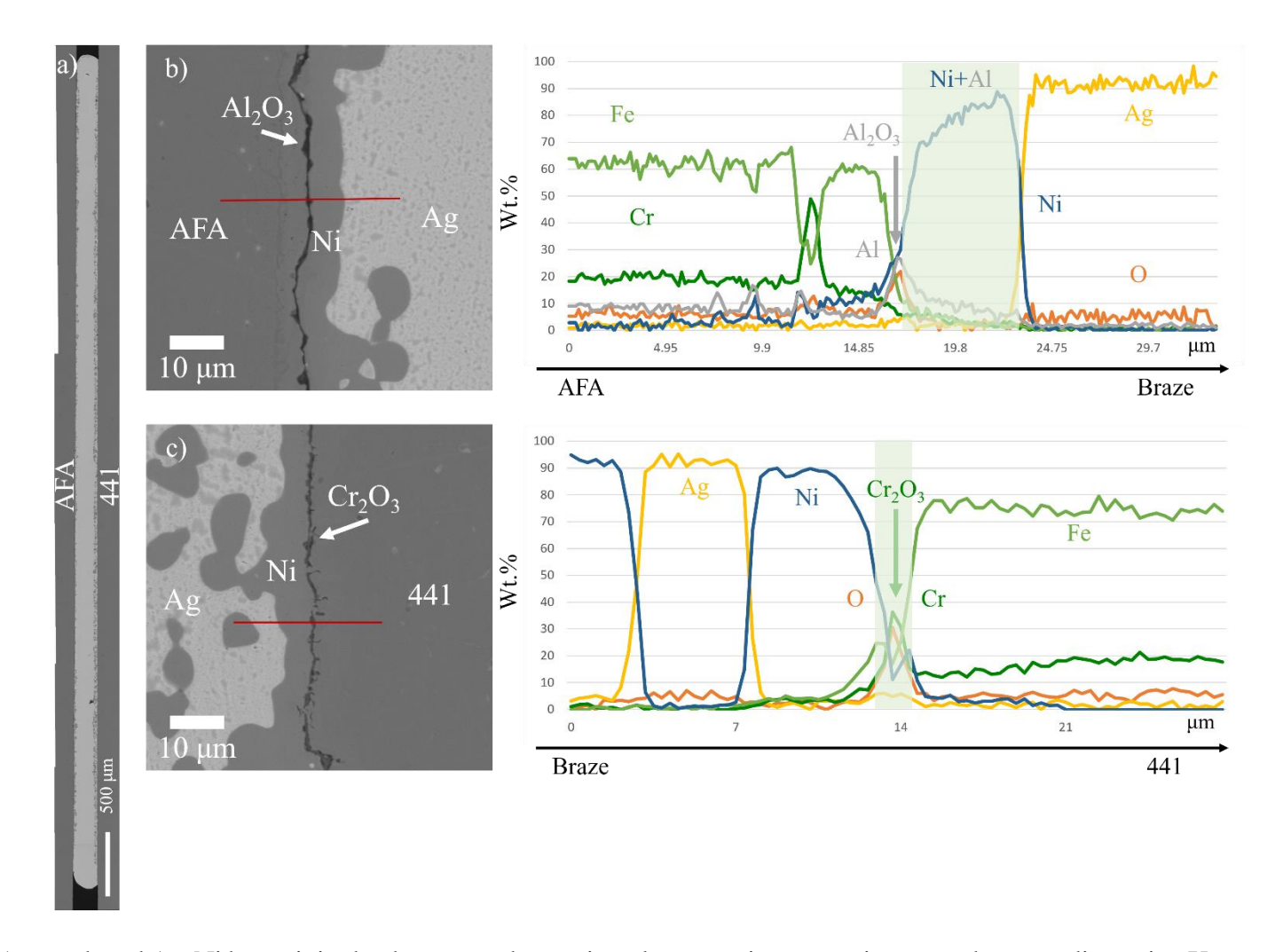


Figure 5-1 As-produced Ag-Ni braze joint back-scattered scanning electron microscopy image and energy dispersive X-ray spectroscopy line scans of (a) the whole joint, (b) the AFA interface, and (c) the 441 interface. The spectra in (b) indicate a spike of Al, and Ni+Al spectrum overlapping. This shows that the dark line is mostly alumina. The spectra in (c) indicate a spike of Cr, which is mostly from  $Cr_2O_3$ .

### 5.2.2 <u>Air Annealed Samples</u>

Figure 5-2(a) shows BSE SEM image of the whole air annealed AFA|Ni|Ag|Ni|441 braze cross-sectional area. The braze microstructure remains mostly unchanged after 300-hour air annealing.

Figure 5-2(b) shows the BSE SEM image of a representative AFA|braze interfacial area and an EDS line scan in the air annealed sample. A thick alumina phase, which is the black line at the interface observed in the SEM, is detected in the EDS line scan. The nickel interlayer adjacent to the alumina remains as metal. The nickel interlayer adjacent to the silver braze is oxidized and porous nickel oxide is observed.

Figure 5-2(c) shows the BSE SEM image of a representative braze|441 interfacial area and an EDS line scan in the air annealed sample. Most of the nickel in the interlayer is oxidized and forms porous nickel oxide. The nickel adjacent to the substrate remains unoxidized. A peak of chromium is observed in the EDS spectra between nickel interlayer and the substrate. This could be the surface scale on 441 stainless steel forms during air annealing.

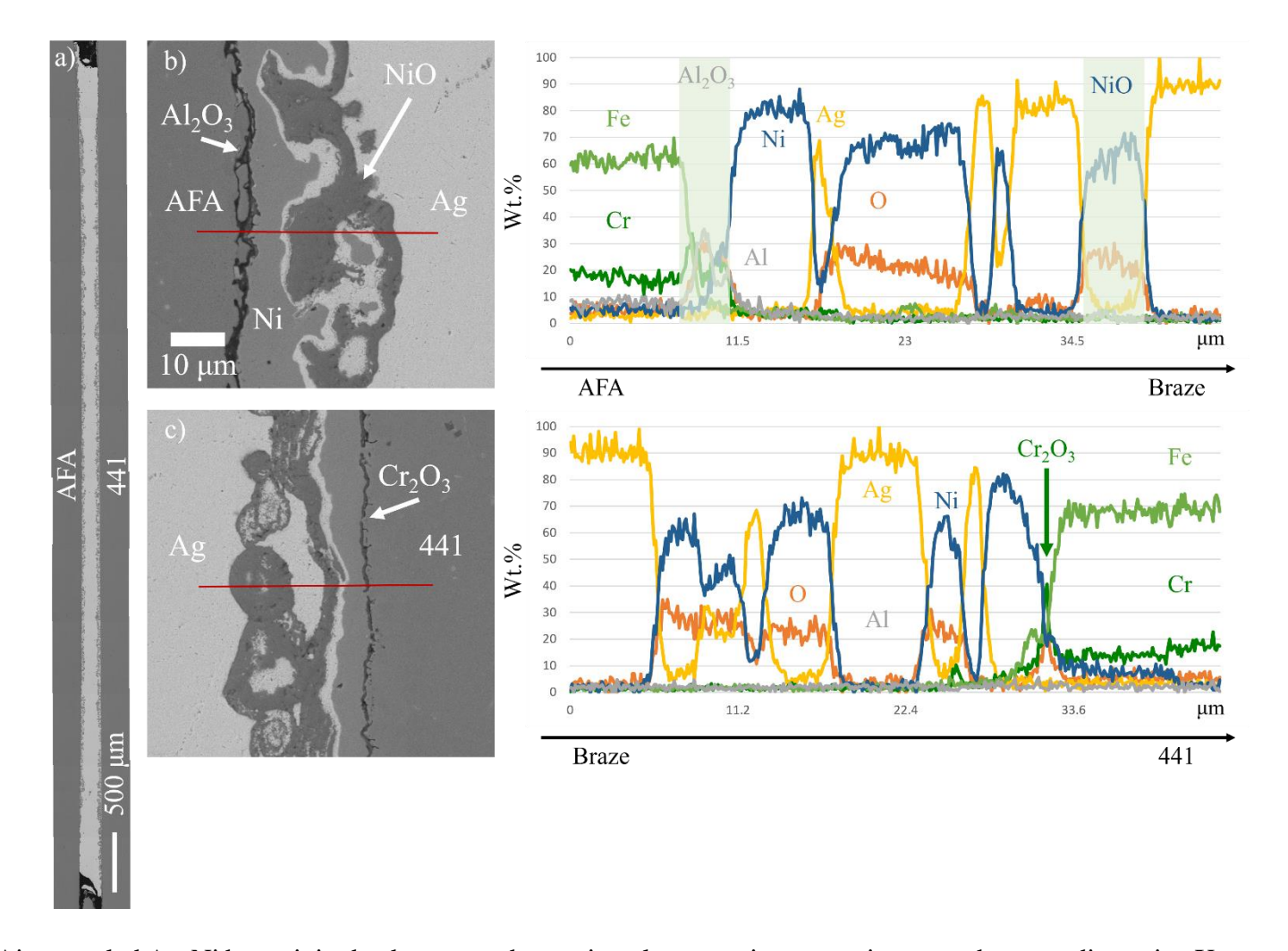


Figure 5-2 Air annealed Ag-Ni braze joint back-scattered scanning electron microscopy image and energy dispersive X-ray spectroscopy line scans of (a) the whole joint, (b) the AFA interface, and (c) the 441 interface. The spectra marked by the translucent green bar in (b) show  $Al_2O_3$ , indicating that in the microstructure, the black phase is the alumina phase at the interface. Similarly, the black line at the interface in (c) is  $Cr_2O_3$ .

### 5.2.3 Redox Cycled Samples

Figure 5-3(a) shows the BSE SEM image of the whole redox cycled AFA|Ni|Ag|Ni|441 braze cross-sectional area. The braze joint had minor structure change. Delamination or cracking is not observed in the cross section.

Figure 5-3(b) shows the BSE SEM image of a representative AFA|braze interfacial area and an EDS line scan in the redox cycled sample. This interface consists of several layers, specifically, 1) the base AFA (with some nickel diffused into the stainless steel), 2) alumina, 3) nickel-aluminum reaction layer, 4) porous nickel, 5) nickel oxide, and 6) the silver braze. The zoomed-in image in the red box in Figure 5-3(b) shows that alumina formed in the porous nickel interlayer near the interface. In comparison to the air annealed sample, the alumina has a net structure, indicating that it formed in multiple oxidation stages and the local topography had considerable changes. Some pores are observed in the silver braze. They are most likely the water pockets that formed during the redox cycling.

Figure 5-3(c) shows the BSE SEM image of a representative braze|441 interfacial area and an EDS line scan in the redox cycled sample. The structure is similar to the air annealed sample other than some pores formed near the nickel interlayer. Specifically, the nickel interlayer shows interdiffusion with 441 stainless steel. Some nickel oxide formed between the interlayer and the silver braze.

The silver in the redox annealed sample is mostly dense. The nickel interlayer reacted with oxygen and was reduced in the next redox stage by hydrogen. The reaction between nickel oxide and the diffused hydrogen would delay the reaction between the dissolved oxygen and the diffused hydrogen. As a result, only tiny amounts of water pocket-induced pores are observed in the microstructure.

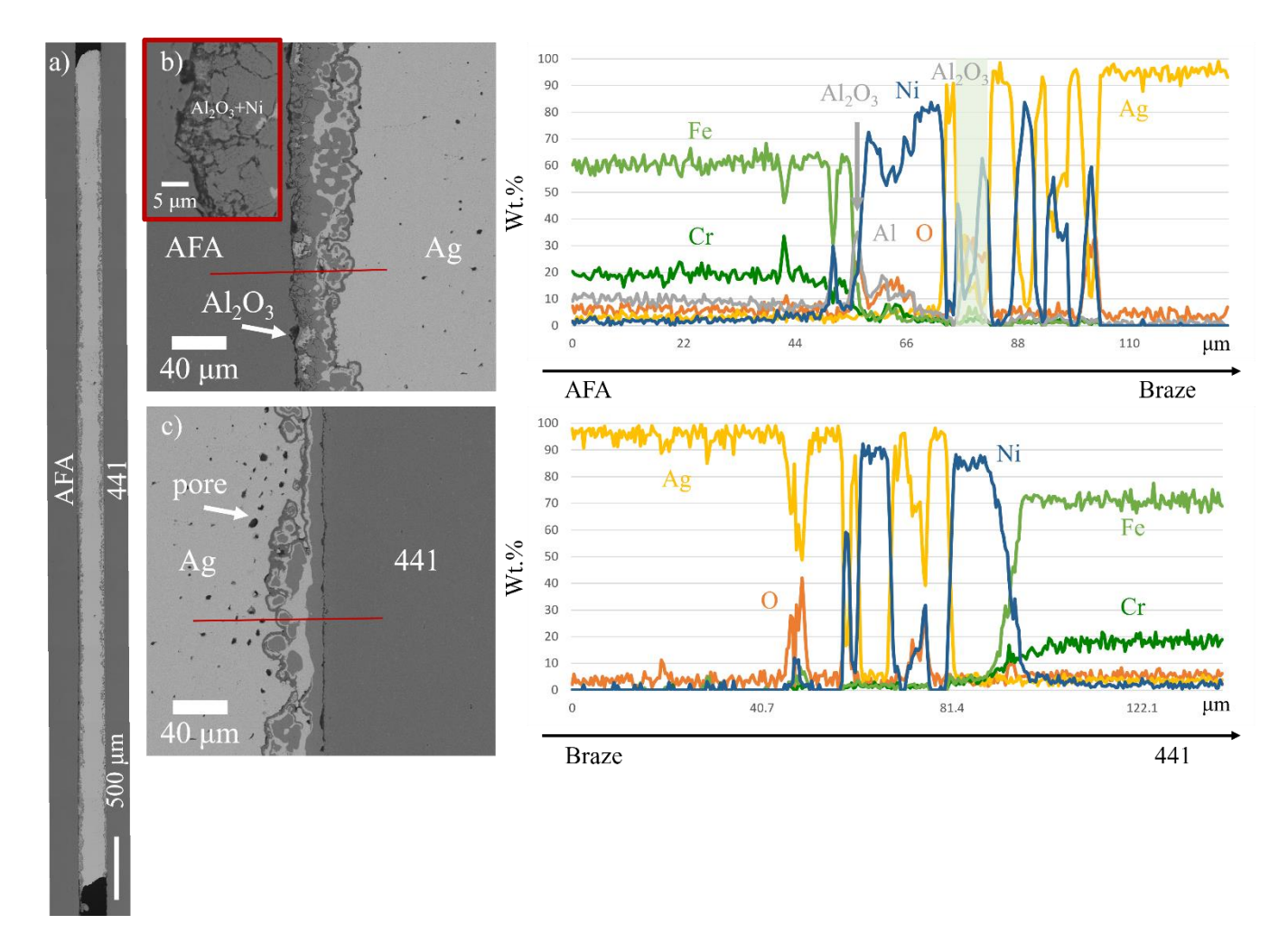


Figure 5-3 Redox cycled Ag-Ni braze joint back-scattered scanning electron microscopy image and energy dispersive X-ray spectroscopy line scans of (a) the whole joint, (b) the AFA interface, and (c) the 441 interface. The red box in (b) shows the net structure of the Al<sub>2</sub>O<sub>3</sub>-Ni. The spectra marked by the translucent green bar show Al-O-Ni overlapping, which supports that alumina formed in the porous nickel interlayer.

### 5.2.4 Extremely Rapid Thermal Cycled Samples

Figure 5-4(a) shows the BSE SEM image of the whole rapid thermal cycled AFA|Ni|Ag|Ni|441 braze joint. Delamination happened during cutting and the AFA substrate was detached from the braze. In the braze joint, some defects were observed.

Figure 5-4(b-d) shows the BSE SEM zoomed-in images of braze joints. Cracks are observed in the silver braze joint along the two end regions, while the majority of the silver remains intact without significant pores or cracks. In the central area of the braze, the joint appears mostly free from defects, indicating the retention of silver in its pure metal form and ductility. This property enables efficient stress release during thermal cycles. However, the interface regions are susceptible to thermal shock due to the presence of brittle nickel oxide and alumina. This rapid thermal cycled sample underwent only an oxidation procedure, indicating that the interface is expected to have a similar composition as the air annealed samples.

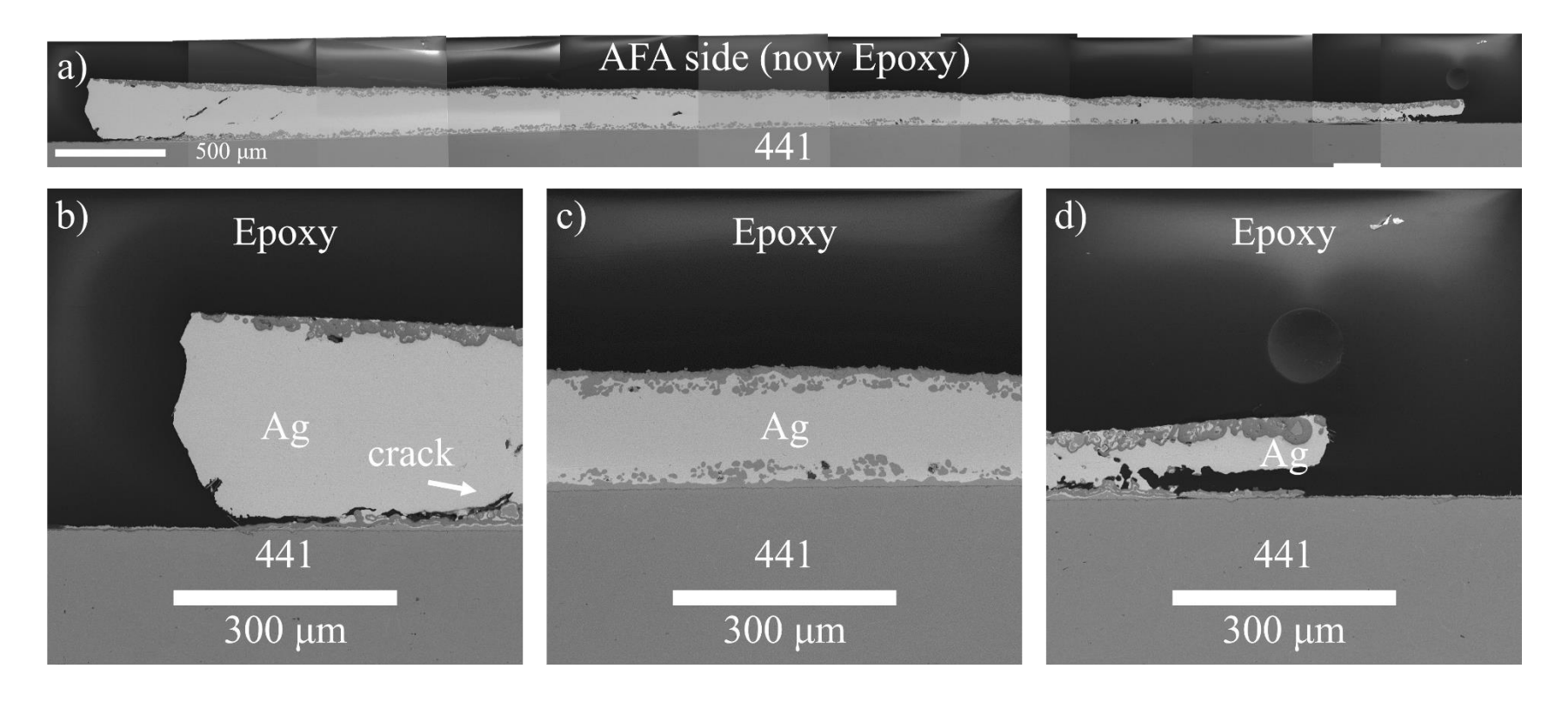


Figure 5-4 Rapid thermal cycled Ag-Ni braze joint back-scattered scanning electron microscopy image of (a) the whole joint, (b) the left end region, (c) the middle region, and (d) the right end region. AFA was detached from the braze during SEM sample preparation. This rapid thermal cycled sample only underwent oxidation procedure. Therefore, the phases near the cracks at the interface should be the same as the interfacial phases in the air annealed sample.

### **5.3 Shear Strength Results**

Table 3 shows the shear strength of Ag-Ni AFA|441 samples in as-produced, 650°C 300-hour air annealed, 25 redox cycled, and 300 rapid thermal cycled states.

Table 3 Shear strength of Ag-Ni AFA|441 samples in different states. Samples in each group are prepared using identical procedures. The numbering merely serves as a means of differentiation between the samples.

Conditions	Shear strength (MPa)					
	Sample1	Sample2	Sample3	Sample4	Sample5	Sample6
As-Produced	12.5	13.7	16.0	N/A	N/A	N/A
Air Annealed	29.9	35.0	38.5	43.6	N/A	N/A
Redox Cycled	16.1	17.7	18.8	19.9	20.3	20.5
Rapid Thermal Cycled	9.8	13.4	16.5	19.8	36.3	37.7

The Ag-Ni braze has a relatively low shear strength in the as-produced condition, with the strongest sample failed at 16.0 MPa. The survival probability of a given sample in a batch can be determined using the method detailed in Subchapter 4.2. Then the strength at a specific survival probability can be determined. The shear strength at 99% survival probability is 8.1 MPa. All of the tested samples failed at the AFA interface with the whole silver braze remaining on 441 stainless steel.

After 300-hour air annealing at 650°C, the shear strength is greatly improved. The strongest sample failed at 43.6 MPa. The shear strength at 99% survival probability is 18.9 MPa. All of the tested samples failed at the AFA interface with the whole silver braze remaining on 441 stainless steel.

After 25 redox cycles, the strength decreases but was still higher than the as-produced samples. The strongest redox cycled sample failed at 20.5 MPa. The shear strength at 99% survival

probability is 13.0 MPa. All of the tested samples failed at the AFA interface with the whole silver braze remaining on 441 stainless steel.

After 300 extremely rapid thermal cycles, the strength distribution exhibits greater variability than the other groups. The strongest sample subjected to rapid thermal cycling failed at 37.7 MPa, the highest among all of the Ag-Ni samples. However, the weakest sample also exhibited lower strength than all of the other Ag-Ni samples, regardless of the heat treatment applied. The shear strength at 99% survival probability is 2.2 MPa. This wide distribution can be attributed to a combination of improved bonding resulting from extended exposure to air and the formation of defects due to thermal shock. Consequently, predicting failures and ensuring quality control become more challenging for real devices that may encounter emergency shutdowns and extremely rapid temperature drops. All the tested samples failed at the AFA interface and the whole silver braze remained on 441 stainless steel.

# **5.4 Contact Resistivity Results**

Table 4 shows the contact resistivity of Ag-Ni braze joints between identical stainless steel substrates (AFA|AFA or 441|441) in as-produced, 650°C 300-hour air annealed, 25 redox cycled, and 300 rapid thermal cycled states.

In the as-produced state, all Ag-Ni samples exhibit contact resistivity in the order of  $10^{-5}$   $\Omega$ •cm<sup>2</sup>. This indicates that Ag-Ni ensures excellent electrical conductivity across the silver-steel interface, regardless of the substrate type. Even in AFA applications where an insulating alumina scale forms to impede electron flow, the presence of Al-Ni intermetallic phases at the interfaces significantly contributes to the low resistivity.

After 300-hour air annealing at 650°C, all AFA joint samples exhibit a slight increase in resistivity, attributed to the formation of thin alumina layers at the interface. One 441 joint sample

shows slightly increased resistivity, while the other two display slightly decreased resistivity. This change can be attributed to interdiffusion between the nickel interlayer and the 441 stainless steel substrate, resulting in a slight reduction in nickel thickness in certain areas of the interface.

Table 4 The contact resistivity of Ag-Ni braze joints between AFA|AFA or 441|441 same type of substrates in different states. Samples in each group are prepared using identical procedures. The numbering merely serves as a means of differentiation between the samples.

	Contact resistivity ( $\Omega \cdot \text{cm}^2$ )						
Conditions	AFA AFA			441 441			
	Sample1	Sample2	Sample3	Sample1	Sample2	Sample3	
As-Produced	6.6×10 <sup>-5</sup>	3.9×10 <sup>-5</sup>	5.9×10 <sup>-5</sup>	2.7×10 <sup>-5</sup>	4.3×10 <sup>-5</sup>	4.0×10 <sup>-5</sup>	
Air Annealed	1.8×10 <sup>-4</sup>	8.7×10 <sup>-5</sup>	7.7×10 <sup>-5</sup>	8.6×10 <sup>-5</sup>	1.6×10 <sup>-5</sup>	1.4×10 <sup>-5</sup>	
Redox Cycled	3.2×10 <sup>-3</sup>	7.0×10 <sup>-4</sup>	$3.0 \times 10^{-3}$	3.7×10 <sup>-6</sup>	1.1×10 <sup>-5</sup>	7.3×10 <sup>-6</sup>	
Rapid Thermal Cycled	5.0×10 <sup>-5</sup>	7.6×10 <sup>-5</sup>	8.5×10 <sup>-5</sup>	1.3×10 <sup>-4</sup>	5.6×10 <sup>-5</sup>	1.4×10 <sup>-5</sup>	

The samples used for the redox cycling durability test were initially in the as-produced state, constituting a separate batch distinct from the other groups. The results of the redox-cycled Ag-Ni joints between AFA|AFA exhibit higher resistivity compared to the as-produced and air annealed samples. This can be attributed to topographical changes in the nickel interlayer during redox cycles, leading to crack formation and subsequent alumina deposition. As a result, thicker alumina layers formed at the interface, increasing the resistivity. In the case of the 441|441 samples, redox cycles partially eliminated the formation of chromium oxide due to the chromia reduction in the reducing stages, which resulted in slightly lower resistivity.

The results for the rapid thermal cycled samples were included; however, they may not accurately reflect the real contact resistivity due to observed delamination in the samples.

Consequently, the severe change in contact area following the rapid thermal cycles could have impacted the measurements.

## **5.5 Competing Brazing Techniques**

### 5.5.1 Ag-CuO

Alternative brazing techniques were assessed and their performance was compared with the Ag-Ni brazing technique. The Ag-CuO samples were examined in as-produced, air annealed, redox cycled, and rapid thermal cycled states.

Figure 5-5(a) shows the back-scattered electron scanning electron microscopy image of the whole as-produced AgCuO braze joint cross-section. The braze joint exhibits an interrupted center with the presence of some pores. This observation aligns with previous findings that indicate the formation of more defects in the Ag-CuO braze joint due to relatively poor silver wetting [65]. The inadequate wetting also hinders silver from covering the entire gap, resulting in a broken braze joint in the center.

Figure 5-5(b) shows the BSE SEM image of a representative AFA|braze interfacial area and an EDS line scan in the as-produced sample. A uniform Al-Cu oxide phase accumulates at the interface. The mixture should be alumina (Al<sub>2</sub>O<sub>3</sub>) and copper aluminate (CuAl<sub>2</sub>O<sub>4</sub>), which was observed in previous study as well [68].

Figure 5-5(c) shows the BSE SEM image of a representative braze|441 interfacial area and an EDS line scan in the as-produced sample. A  $\sim$ 10  $\mu$ m thick, porous reaction layer formed between the pure silver joint and the substrate. The layer consists of iron oxide and chromium oxide from the substrate, and copper oxide from the printed interlayer.

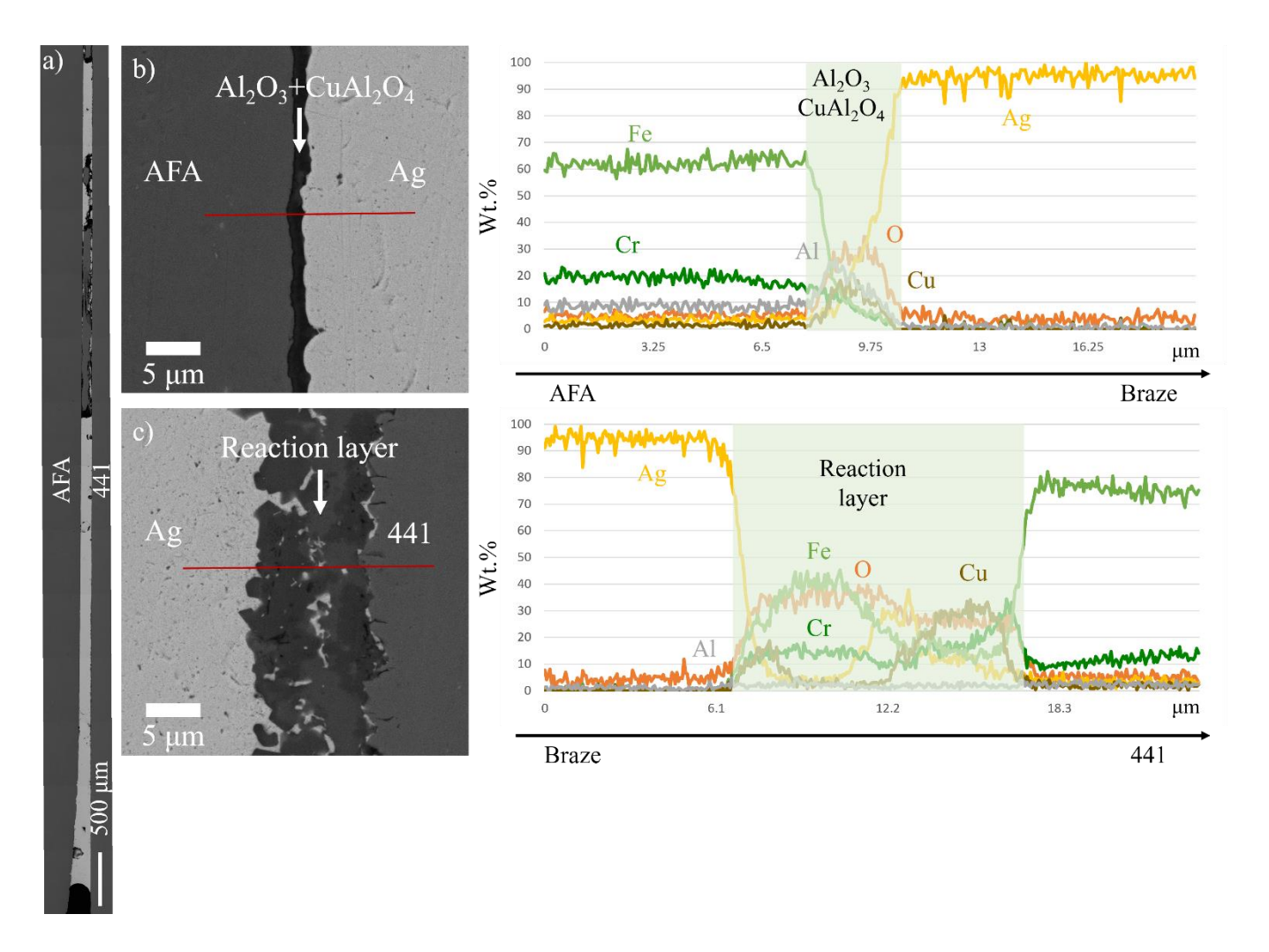


Figure 5-5 As-produced Ag-CuO braze joint back-scattered scanning electron microscopy image and energy dispersive X-ray spectroscopy line scans of (a) the whole joint, (b) the AFA interface, and (c) the 441 interface. The pore in (a) formed due to the inadequate wetting between the filler and the substrate. The black phase between AFA and Ag in (b) is the mixture of Al<sub>2</sub>O<sub>3</sub>+CuAl<sub>2</sub>O<sub>4</sub>, which has the corresponding spectra marked by the translucent green bar. The reaction layer in (c) is the mixture of Fe-Cr-Cu oxide.

Figure 5-6(a) shows the back-scattered electron scanning electron microscopy image of the whole air annealed AgCuO braze joint cross-section. The braze joint is shorter in length than the previous as-produced sample due to the poor silver wetting and broken braze joint.

Figure 5-6(b) shows the BSE SEM image of a representative AFA|braze interfacial area and an EDS line scan in the air annealed sample. A dark reaction layer, approximately 2 μm thick, is observed between AFA and the braze joint. The EDS spectra demonstrate a similar Al<sub>2</sub>O<sub>3</sub>-CuAl<sub>2</sub>O<sub>4</sub> composition to that of the as-produced sample. This suggests that air annealing has minimal effect on the interfacial composition after preparing the samples in air.

Figure 5-6(c) shows the BSE SEM image of a representative braze|441 interfacial area and an EDS line scan in the air annealed sample. A porous reaction layer, approximately 10 μm thick, is observed between the pure silver joint and the substrate. The composition and structure of this reaction layer resemble those observed in the as-produced sample. Annealing merely prolongs the duration of sample exposure to air.

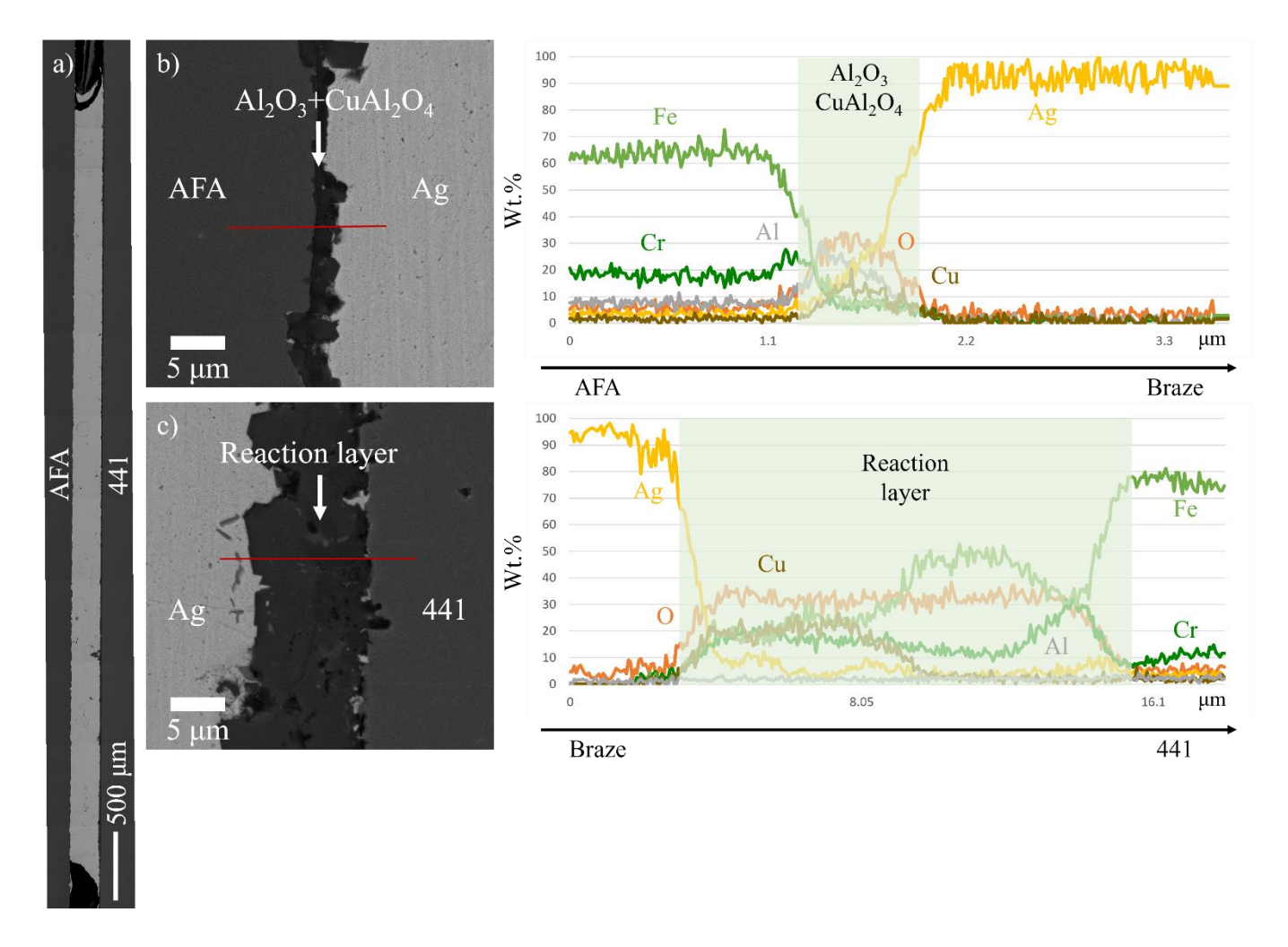


Figure 5-6 Air annealed Ag-CuO braze joint back-scattered scanning electron microscopy image and energy dispersive X-ray spectroscopy line scans of (a) the whole joint, (b) the AFA interface, and (c) the 441 interface. The black phase between AFA and Ag in (b) is the mixture of  $Al_2O_3+CuAl_2O_4$ , which has the corresponding spectra marked by the translucent green bar. The reaction layer in (c) is the mixture of Fe-Cr-Cu oxide.

Figure 5-7(a) shows the back-scattered electron scanning electron microscopy image of the whole redox cycled AgCuO braze joint cross-section. The braze joint exhibits a similar appearance to that in the as-produced state.

Figure 5-7(b-d) shows the BSE SEM zoomed-in images of the braze joints. Pores can be observed at the ends of the silver joint, resulting from the reaction between dissolved oxygen and diffused hydrogen. However, the center region of the braze exhibits minimal water-induced pores. This suggests that redox cycles may give rise to the formation of water pockets within the braze joint, albeit with limited impact.

Figure 5-8(a) shows the back-scattered electron scanning electron microscopy image of the whole rapid thermal cycled AgCuO braze joint cross-section. The braze joint exhibits numerous pores, and delamination occurred at both the AFA and 441 interfaces. The observation of the cross-section suggests a weak connection between the two substrates.

Figure 5-8(b-d) shows the BSE SEM zoomed-in images of braze joints. Delamination is observed between the reaction layer and the silver joint on both sides. It is important to note that the gray dots within the silver joints represent copper originating from the interlayer.

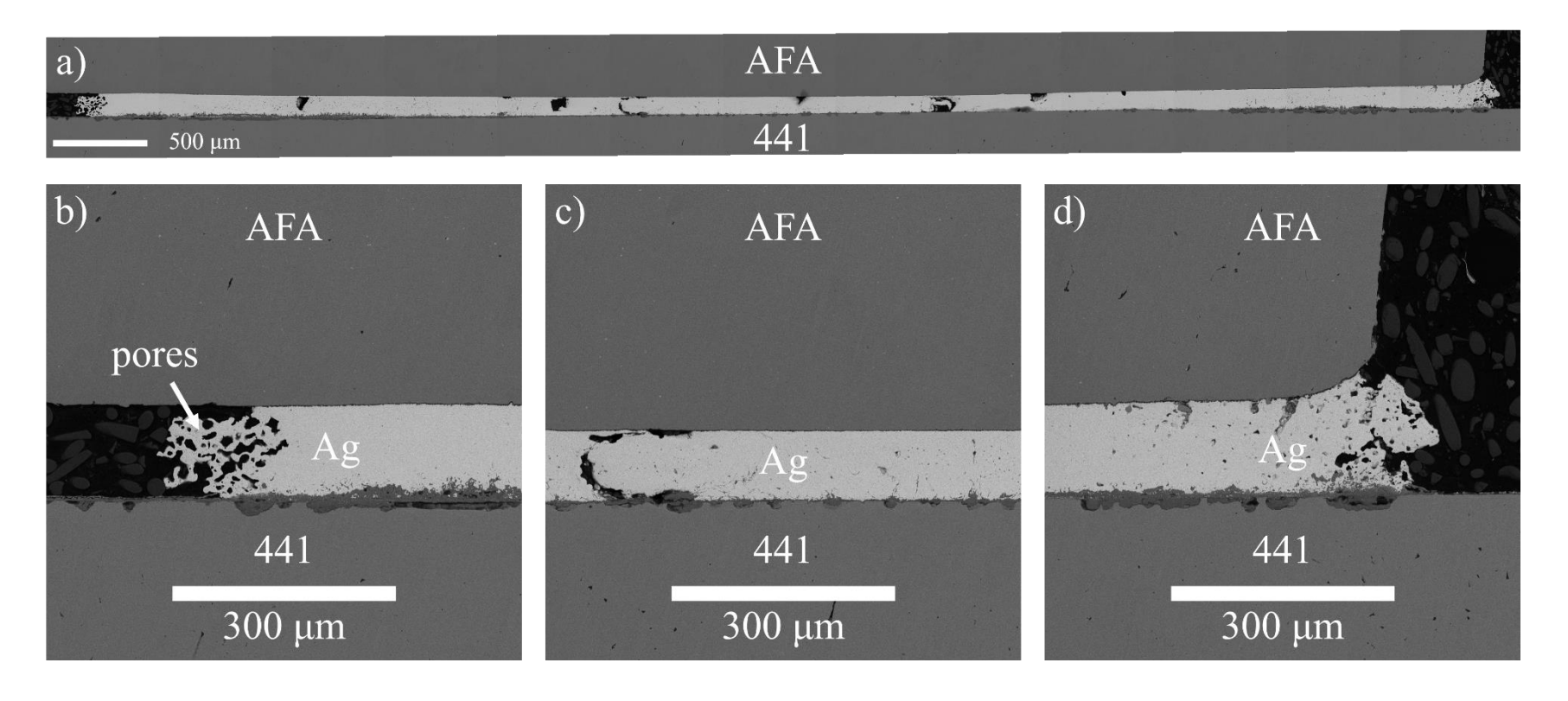


Figure 5-7 Redox cycled Ag-CuO braze joint back-scattered scanning electron microscopy image of (a) the whole joint, (b) the left end region, (c) the middle region, and (d) the right end region. The openings near the end regions are the pores from hydrogen-oxygen reaction. Phases between the silver braze joint and 441 stainless steel are the reaction layer similar to that observed in the air annealed sample.

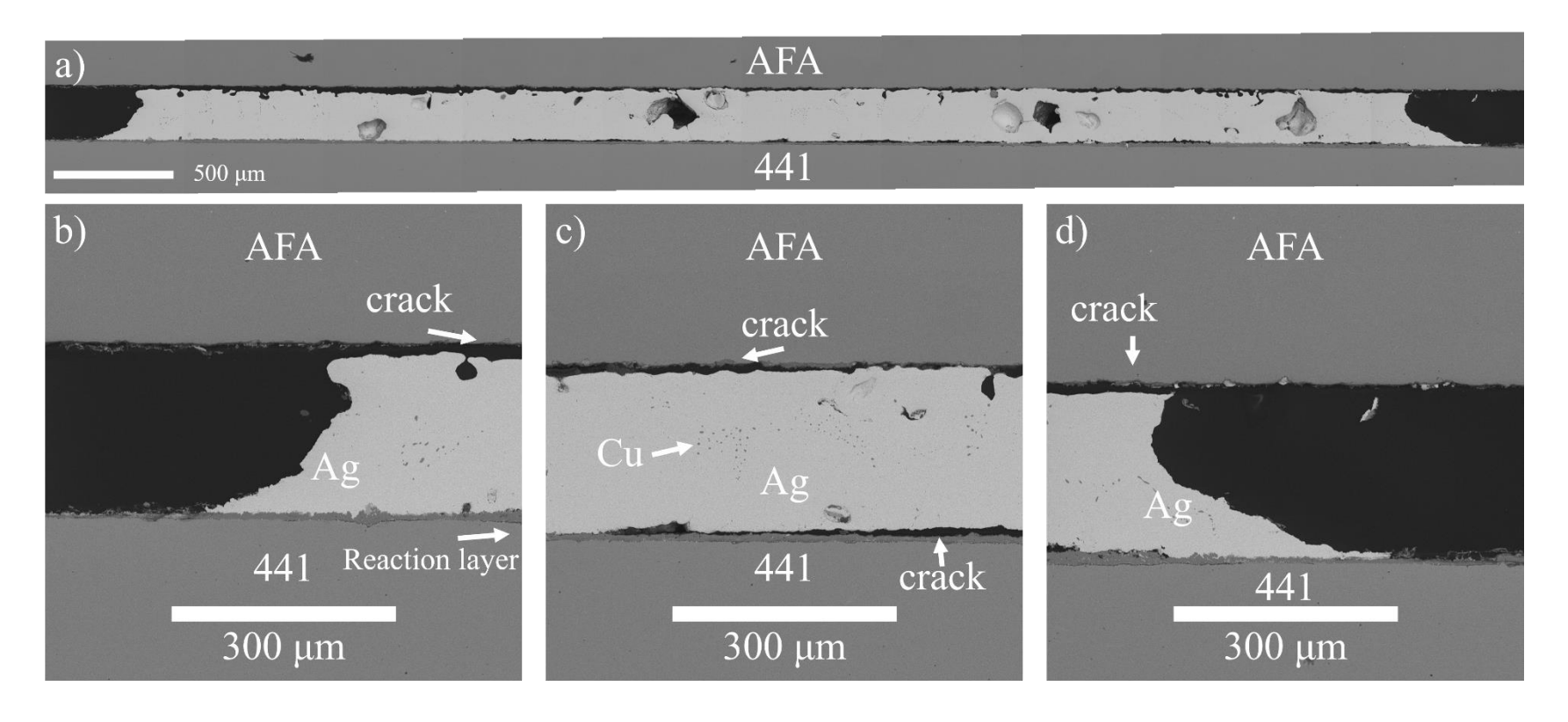


Figure 5-8 Rapid thermal cycled Ag-CuO braze joint back-scattered scanning electron microscopy image of (a) the whole joint, (b) the left end region, (c) the middle region, and (d) the right end region. Cracks exist between the filler and substrates. A reaction layer exists at the interface. The gray dots in the joint are the clusters of copper in the filler metal.

Table 5 shows the shear strength values of Ag-CuO AFA|441 samples under as-produced, air annealed, and redox cycled conditions. The data for the samples subjected to rapid thermal cycling is not available because all the samples in that batch failed prematurely during the loading process onto the tensile test machine, prior to the actual test.

Table 5 Shear strength of Ag-CuO AFA|441 samples in different states. Samples in each group are prepared using identical procedures. The numbering merely serves as a means of differentiation between the samples.

Conditions	Shear strength (MPa)					
	Sample1	Sample2	Sample3	Sample4	Sample5	Sample6
As-Produced	27.5	28.7	34.5	40.4	43.7	43.8
Air Annealed	29.3	37.0	46.8	50.4	52.6	59.4
Redox Cycled	7.7	11.7	12.6	13.4	14.9	17.7
Rapid Thermal Cycled	N/A	N/A	N/A	N/A	N/A	N/A

In the as-prepared condition, the Ag-CuO brazes exhibits high shear strength because they were prepared in air with more oxygen at the interfaces. The strongest as-produced sample failed at 43.8 MPa. The survival probability of a given sample in a batch can be determined using the method detailed in Subchapter 4.2. Then the strength at a specific survival probability can be determined. The shear strength at 99% survival probability is 15.4 MPa. All the samples failed at the AFA interface.

After 300-hour air annealing at 650°C, the shear strength further improves and surpasses that of Ag-Ni brazes. The strongest sample failed at 59.4 MPa, and the shear strength at 99% survival probability is 16.1 MPa. All the samples failed at the 441 interface.

After 25 redox cycles, the strength decreases and becomes weaker than the Ag-Ni samples. The strongest redox cycled sample failed at 17.7 MPa, with a shear strength at 99% survival probability of 4.2 MPa. All the samples failed in the silver braze.

After 300 rapid thermal cycles, all the samples failed at the AFA interface. The utilization of Ag-CuO brazes is recommended for applications involving milder thermal cycles.

Table 6 shows the contact resistivity of Ag-CuO braze joints between identical stainless steel substrates (AFA|AFA or 441|441) under as-produced, 650°C 300-hour air annealed, 25 redox cycled, and 300 rapid thermal cycled conditions. The data for the Ag-CuO 441|441 samples subjected to rapid thermal cycling is not available as all the samples in the batch broke at the interfaces during removing the surface oxide.

Table 6 The contact resistivity of Ag-CuO braze joints between AFA|AFA or 441|441 same type of substrates in different states. Samples in each group are prepared using identical procedures. The numbering merely serves as a means of differentiation between the samples.

	Contact resistivity ( $\Omega \cdot \text{cm}^2$ )						
Conditions	AFA AFA			441 441			
	Sample1	Sample2	Sample3	Sample1	Sample2	Sample3	
As-Produced	1.0	15.4	1.6	0.1	2.0	11.0	
Air Annealed	0.7	0.6	1.4	11.2	13.8	15.6	
Redox Cycled	0.7	1.6	3.1	0.5	4.3	3.6	
Rapid Thermal Cycled	1.5	1.1	3.8	N/A	N/A	N/A	

In the as-produced state, the Ag-CuO AFA|AFA samples exhibit contact resistivity ranging from 1.0 to 15.4  $\Omega$ •cm<sup>2</sup>. These values are approximately five orders of magnitude higher than those observed in the Ag-Ni samples between the same substrates. Similarly, the Ag-CuO 441|441 samples exhibit contact resistivity ranging from 0.1 to 11.0  $\Omega$ •cm<sup>2</sup>, which is approximately four

orders of magnitude higher than the Ag-Ni samples between the same substrates. These results indicate that Ag-CuO brazes exhibit high interfacial resistivity in both AFA or 441 applications due to the presence of oxide at the AFA interface or the formation of a thick porous reaction layer at the 441 interface.

After 300-hour air annealing at 650°C, all Ag-CuO AFA|AFA samples exhibit a slight decrease in resistivity. This resistivity change can be attributed to the air annealing, which densifies the silver joint and eliminates pores because of creep deformation. Conversely, the Ag-CuO 441|441 samples show increased resistivity. This change can be attributed to the increased reaction layer thickness at the 441 stainless steel interface.

The samples used for the redox cycling durability test were initially in the as-produced state, constituting a separate batch distinct from the other groups. The results of the redox-cycled Ag-CuO joints between AFA|AFA exhibited similar resistivity to the air annealed samples. The reducing stages in the redox cycles were unable to reduce the alumina at the AFA interface, leading to an unchanged resistivity. Because the oxygen partial pressure to reduce alumina at 650°C needs to be 10<sup>-50</sup>, while the oxygen pressure set by the 4% hydrogen (considering 1ppm of water) can only reach 10<sup>-33</sup> [160]. In the case of the 441|441 samples, redox cycles partially eliminated the formation of chromium oxide, similar to the results observed in the Ag-Ni 441|441 samples, leading to a reduction in resistivity.

The results for the rapid thermal cycled AFA|AFA samples are included; however, they may not accurately reflect the real contact resistivity due to the observed delamination in the samples. In the measured results, the results are similar to the air annealed samples, indicating that once prepared in air, the resistivity remains stable due to the presence of stable alumina at the

interface. No data could be obtained for the 441|441 samples because all the samples broke during the removal of surface oxide using sandpaper.

#### 5.5.2 Heraeus C8710

The Heraeus C8710 brazing technique was examined in both the as-produced and air annealed states. However, the results obtained from microstructural analyses, shear strength, and contact resistivity indicated poor performance in these conditions. Consequently, the evaluation of this brazing technique under redox cycled and rapid thermal cycled conditions was not conducted.

Figure 5-9(a) shows the BSE SEM image of the whole as-produced Heraeus C8710 braze joint cross-section. A significant crack can be observed in the silver joint. This crack resulted from the manufacturing process, where two wet printed silver pads were joined together to form the joint. Due to incomplete bonding between the two silver paste pads, a cohesive structure could not be achieved. As a result, certain regions remained detached, leading to the formation of the crack, even after 10 hours of annealing.

Figure 5-9(b) shows the representative cross-sectional BSE microstructural and EDS compositional analyses of the AFA interface. Aluminum from the substrate segregated to the surface, forming aluminum oxide. A piece of the reaction layer debris from the substrate became embedded within the silver, forming gray dots as observed in the SEM image. This debris is attributed to the rough surface of the substrates. During screen printing or firing process, hills of the rough surface reacted with aluminum and became detached to the substrate.

Figure 5-9(c) shows the representative cross-sectional BSE microstructural and EDS compositional analyses of the 441 interface. Chromium from the substrate segregated to the surface, resulting in the formation of chromium oxide. A reaction layer is observed between the chromium oxide and the 441 stainless steel substrate.

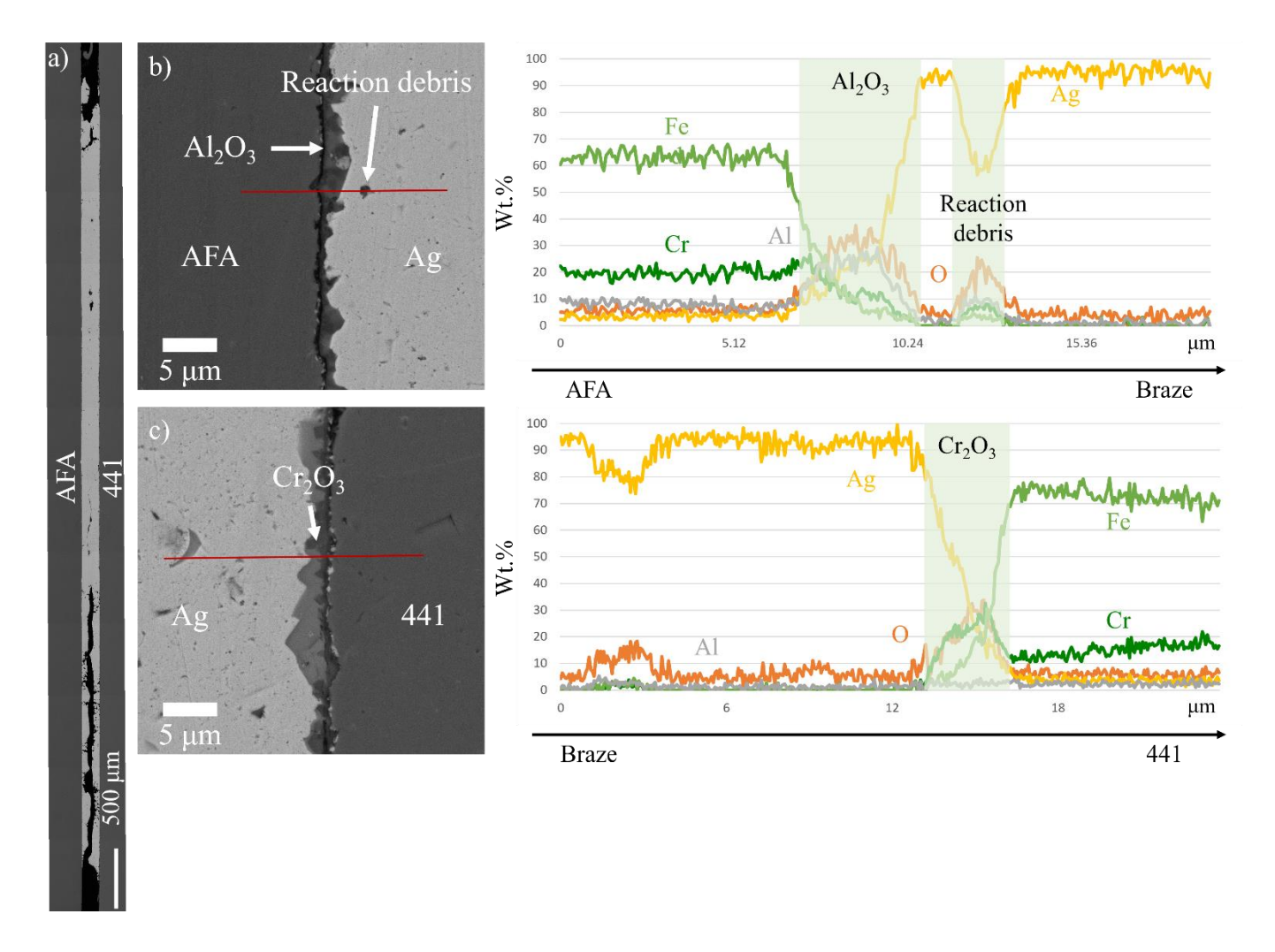


Figure 5-9 As-produced Heraeus C8710 braze joint back-scattered scanning electron microscopy image and energy dispersive X-ray spectroscopy line scans of (a) the whole joint, (b) the AFA interface, and (c) the 441 interface. An alumina layer formed between AFA and the braze joint as shown in (b), with the corresponding spectra marked by the translucent green bar. A small reaction debris detached from the layer and was stuck in silver. A chromia layer formed between the braze joint and 441 stainless steel as shown in (c), with the corresponding spectra marked by the translucent green bar.

Figure 5-10(a) shows the BSE SEM image of the whole air annealed Heraeus C8710 braze joint cross-section. Cracks and pores from the preparation process can still be observed after 300 hour of air annealing. In part of the braze joint, the structure is mostly dense and uniform.

Figure 5-10(b) shows the representative cross-sectional BSE microstructural and EDS compositional analyses of the AFA interface. A  $\sim$ 2  $\mu$ m thick dark layer is observed between the AFA and the braze joint. The EDS compositional analysis shows that this layer is a mixture of aluminum oxide, iron oxide and chromium oxide. Therefore, this is the oxide formed on the surface of the AFA.

Figure 5-10(c) shows the representative cross-sectional BSE microstructural and EDS compositional analyses of the 441 interface. Chromium oxide formed at the interface. A reaction layer formed between the chromium oxide and the 441 stainless steel substrate.

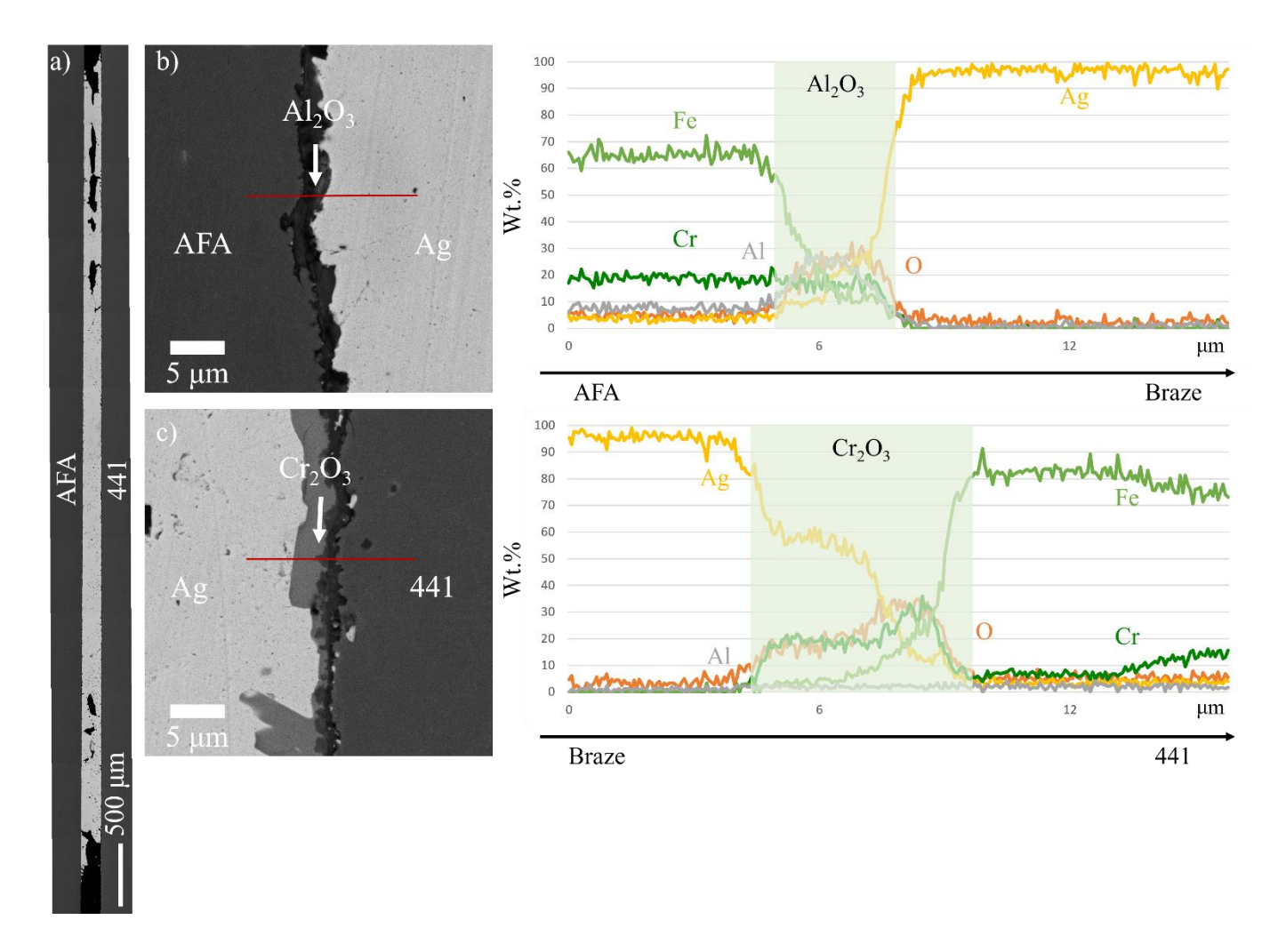


Figure 5-10 Air annealed Heraeus C8710 braze joint back-scattered scanning electron microscopy image and energy dispersive X-ray spectroscopy line scans of (a) the whole joint, (b) the AFA interface, and (c) the 441 interface. An alumina layer formed between AFA and the braze joint as shown in (b), with the corresponding spectra marked by the translucent green bar. A chromia layer formed between the braze joint and 441 stainless steel as shown in (c), with the corresponding spectra marked by the translucent green bar.

Table 7 shows the shear strength of Heraeus C8710 AFA|441 sample in as-produced and air annealed states.

Table 7 Shear strength of Heraeus C8710 AFA|441 samples in as-produced and air annealed states. Samples in each group are prepared using identical procedures. The numbering merely serves as a means of differentiation between the samples.

Conditions	Shear strength (MPa)						
	Sample1	Sample2	Sample3	Sample4	Sample5	Sample6	
As-Produced	6.5	7.3	9.2	10.4	12.8	15.5	
Air Annealed	10.7	10.8	15.8	16.3	22.0	N/A	

The shear strength of the Heraeus sample is relatively low. The strongest as-produced sample failed at 15.5 MPa. The survival probability of a given sample in a batch can be determined using the method detailed in Subchapter 4.2. Then the strength of a specific survival probability can be determined. The shear strength at 99% survival probability is only 2.6 MPa. The strongest air annealed sample failed at 22.0 MPa. The shear strength at 99% survival probability is only 4.0 MPa. The samples failed between two printed Heraeus pads. The mechanical test results are consistent with the microstructure analysis that the crack existed in the as-produced and air annealed samples.

Table 8 shows the contact resistivity of Heraeus C8710 braze joint between the same type of stainless steel (AFA|AFA or 441|441). The contact resistivity of Heraeus between AFA|AFA shows minimal changes before and after air annealing, remaining in the range of 1-10  $\Omega$ •cm² in both as-produced and air annealed conditions. The contact resistivity of Heraeus between 441|441 exceeded 100  $\Omega$ •cm² in the as-produced condition. After air annealing, the contact resistivity decreased to lower than 1  $\Omega$ •cm². This reduction can be attributed to the observed microstructural densification, which has been previously reported in Heraeus C8710 silver paste [93].

Table 8 The contact resistivity of Heraeus C8710 braze joints between AFA|AFA or 441|441 same type of substrates in different states. Samples in each group are prepared using identical procedures. The numbering merely serves as a means of differentiation between the samples.

	Contact resistivity (Ω•cm²)						
Conditions	AFA AFA			441 441			
	Sample1	Sample2	Sample3	Sample1	Sample2	Sample3	
As-Produced	0.5	3.2	1.3	$2.1 \times 10^2$	$5.4 \times 10^2$	$2.6 \times 10^2$	
Air Annealed	1.6	2.7	4.2	0.2	0.7	1.6	

# 5.6 Discussion

Figure 5-11 presents a Weibull plot comparing the shear strength of as-produced and air annealed Ag-Ni, Ag-CuO, and Heraeus C8710 double shear samples. In the as-produced state, the Ag-Ni samples exhibit higher shear strength and a more concentrated strength distribution compared to the Heraeus C8710 samples. But Ag-Ni samples exhibit lower shear strength than the Ag-CuO samples. After air annealing, the shear strength of the Ag-Ni samples is comparable to that of the Ag-CuO samples and much stronger than the slightly improved Heraeus C8710 samples.

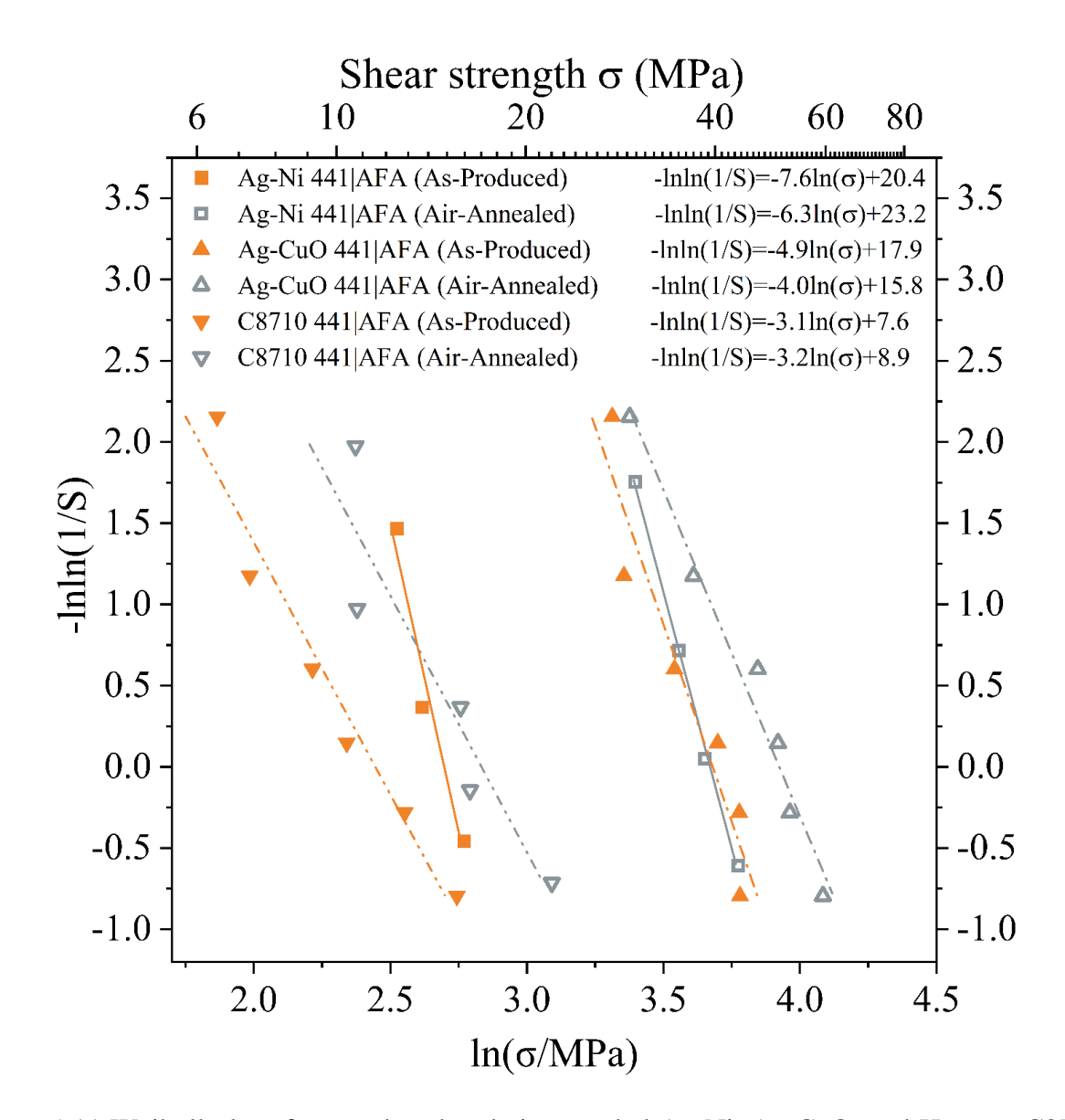


Figure 5-11 Weibull plot of as-produced and air annealed Ag-Ni, Ag-CuO, and Heraeus C8710 double shear lap samples between AFA and 441. Ag-Ni exhibits higher shear strength than Heraeus C8710 and lower shear strength than Ag-CuO. After air annealing, Ag-Ni exhibits comparable shear strength with Ag-CuO and much better strength than Heraeus C8710.

Based on the previous microstructural analyses, it was observed that the Ag-Ni samples exhibit dense microstructures. In contrast, the Heraeus C8710 samples show poor adhesion between two printed silver paste pads, resulting in the presence of cracks. These cracks make delamination inside the silver joint more likely, leading to weaker bonding compared to the Ag-Ni samples. The Ag-CuO samples were prepared in air, resulting in an increased presence of

oxygen at the interface. This increased oxygen content contributes to higher work of adhesion and stronger bonding. Similarly, after air annealing, both the Ag-Ni and Ag-CuO samples experience improved bonding due to the additional oxygen present.

Conversely, the Heraeus C8710 samples also benefit from the increased oxygen during air annealing. However, the presence of cracks in these samples limits the extent of bonding improvement.

Figure 5-12 presents the contact resistivity of as-produced and air annealed Ag-Ni, Ag-CuO, and Heraeus C8710 samples between same stainless steel substrates. In both the as-produced and air annealed states, the Ag-Ni samples exhibit low contact resistivity, while the Ag-CuO and Heraeus C8710 samples display significantly higher resistivity. It is worth noting that for the overall Solid Oxide Fuel Cell components, the desired contact resistivity is below 0.5  $\Omega$ •cm², ideally approaching 0.1  $\Omega$ •cm² [161]. The maximum allowable resistivity for the components, set at 0.3  $\Omega$ •cm², is indicated by the red horizontal line in the figure. Considering that reducing the resistivity of electrodes and electrolytes is more challenging, a benchmark of 1% of the maximum tolerable resistivity is chosen for evaluating the performance of the braze joints. In this regard, the Ag-Ni samples exhibit lower resistivity than the benchmark value. However, both the Ag-CuO and Heraeus C8710 samples demonstrate higher resistivity values, indicating that they may not meet the desired criteria for optimal performance in terms of contact resistivity.

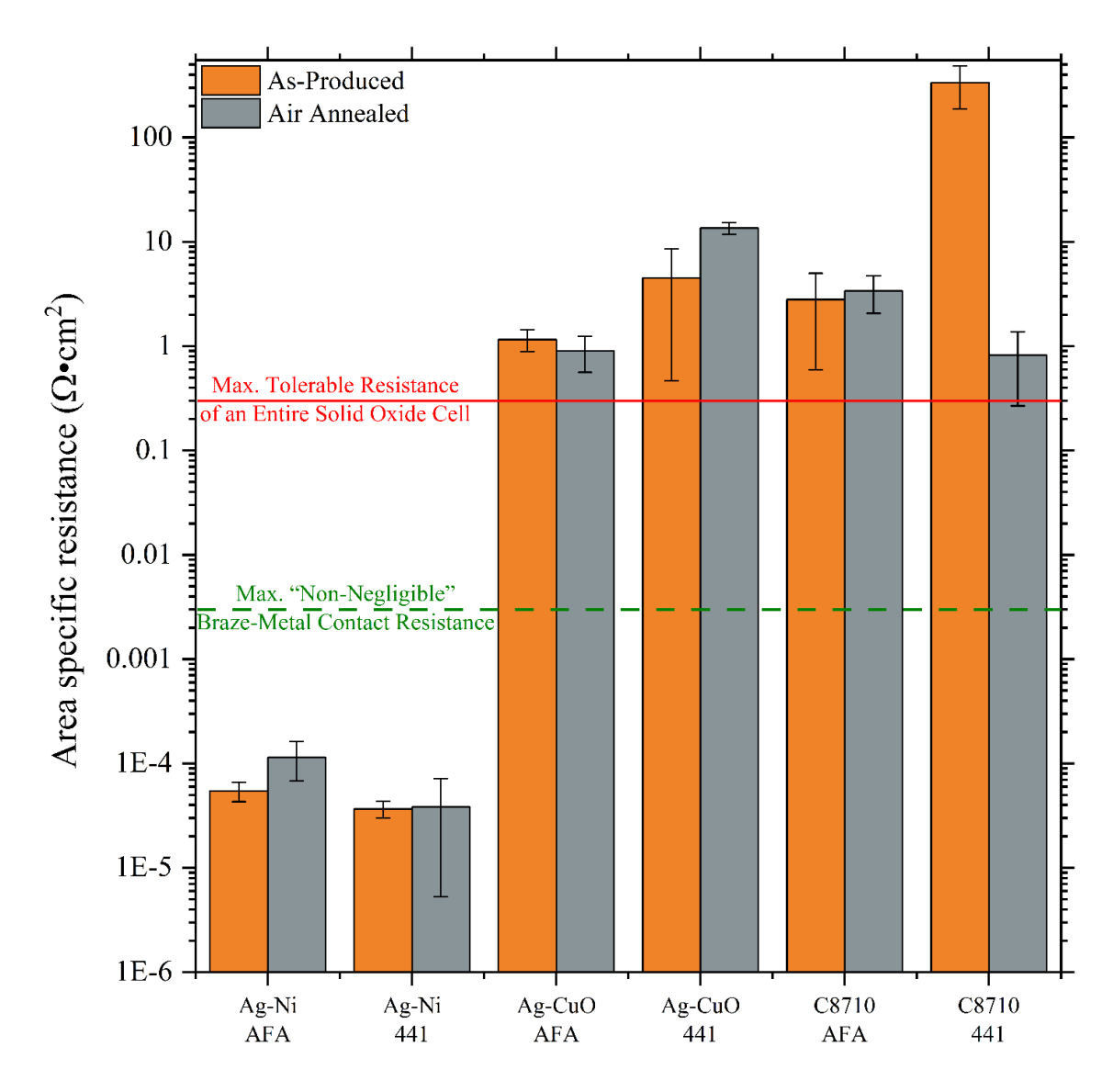


Figure 5-12 Contact resistivity of as-produced and air annealed Ag-Ni, Ag-CuO, and Heraeus C8710 samples between the same stainless steel substrates. Ag-Ni samples show similar resistivity in as-produced and air annealed conditions. In both conditions, Ag-Ni samples show much lower resistivity than Ag-CuO and Heraeus C8710.

Based on the previous microstructural analyses, it was observed that in the Ag-Ni samples, most of the aluminum from the AFA substrates coexists with nickel. The presence of nickel prevents the formation of alumina at the interlayer. Additionally, nickel and 441 stainless steel can form metallurgical bonding due to interdiffusion, leading to low resistivity in both applications between AFA|AFA and 441|441.

On the other hand, thick oxide layers were observed at the interfaces of the Ag-CuO and Heraeus C8710 samples. These oxide layers contribute to higher resistivity in these samples, resulting in less favorable electrical performance.

# **5.7 Summary**

Chapter 5 focuses on the evaluation of microstructure, shear strength, and contact resistivity of Ag-Ni brazes for AFA and 441 bonding applications.

It is found that despite low bonding strength in the as-produced state, Ag-Ni braze joint between AFA and 441 exhibits good mechanical bonding, achieving over 40 MPa. It is comparable to the currently widely used brazing technique Ag-CuO in the SOFC community. In applications requiring electron conductivity through stainless steel substrates, Ag-Ni braze joints show superior electrical performance to Ag-CuO and commercial product Heraeus C8710. The contact resistivity is  $\sim 10^{-4} \, \Omega^{\bullet} \text{cm}^2$ , orders of magnitude lower than the competing techniques. The findings from this study are valuable to researchers in this field, enabling them to select appropriate brazing techniques suitable for specific environments.

In the subsequent chapter, a performance comparison after redox cycling and rapid thermal cycling will be presented.

## 6 Performance and Durability of Ag-Pt Braze Joints to Dissimilar Stainless Steels

## 6.1 Introduction and Rationale of Ag-Pt Brazing

The Particle Interlayer Directed Wetting and Spreading (PIDWAS) technique has demonstrated its capability to achieve wetting of conventionally unwettable surfaces using a nickel interlayer in various materials [65, 78, 93, 94]. The advantages of incorporating aluminum-containing stainless steel in Solid Oxide Fuel Cell stacks have been discussed, as it can mitigate chromium volatilization and prevent the detrimental chromium poisoning effect that could negatively impact SOFC performance.

However, during initial tests involving the introduction of small amounts of aluminum into the 441-441 silver braze joints, the occurrence of cracks was observed. Even with a 0.5wt.% aluminum-alloyed silver joint, severe cracks were observed after the joint formation process. Figure 6-1 shows the BSE SEM and EDS line scan of the braze joint between two 441 stainless steel substrates using Ag-0.5wt.%Al alloy. The cracks were found to be associated with the presence of brittle intermetallic compounds formed between nickel and aluminum. These results highlight that under extreme conditions, where excessive aluminum dissolves into the silver joint, the formation of cracks becomes possible. This emphasizes the importance of careful alloy design and optimization to avoid detrimental effects on the integrity of the brazed joints.

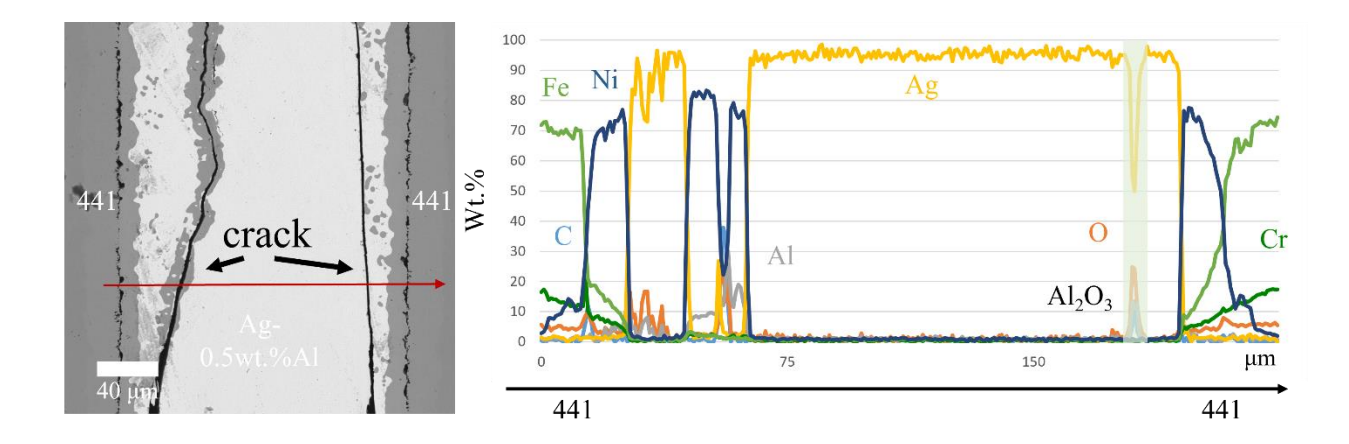


Figure 6-1 As-produced Ag-0.5wt.%Al-Ni 441|441 braze joint back-scattered scanning electron microscopy image and energy dispersive X-ray spectroscopy line scan. Cracks exist in the joint, which is attributed to the Al-Ni reaction product and alumina from the 0.5wt.% aluminum in the filler metal.

Therefore, it becomes imperative to explore the viability of utilizing an alternative element as the PIDWAS interlayer for forming silver brazes between substrates. The aim is to identify an element that can deliver comparable performance to Ag-Ni braze joints while addressing the issue of cracks resulting from the brittle Ni-Al intermetallic compound.

The desired candidate element should possess the following characteristics:

- Higher melting point than silver to remain in solid form when silver melts to control the wetting pattern or restrain the wetting area.
- Ability to form aluminide phases that can capture aluminum and hinder oxide formation.
- Potential formation of ductile aluminide phases to mitigate the occurrence of cracks.
- Possibility of wetting by silver.
- Partial solubility in silver, rather than complete solubility.

Upon careful evaluation of elements in the periodic table, platinum emerges as a promising candidate that fulfilled the specified criteria. Figure 6-2 shows the search criteria and the corresponding results obtained for various elements in the periodic table.

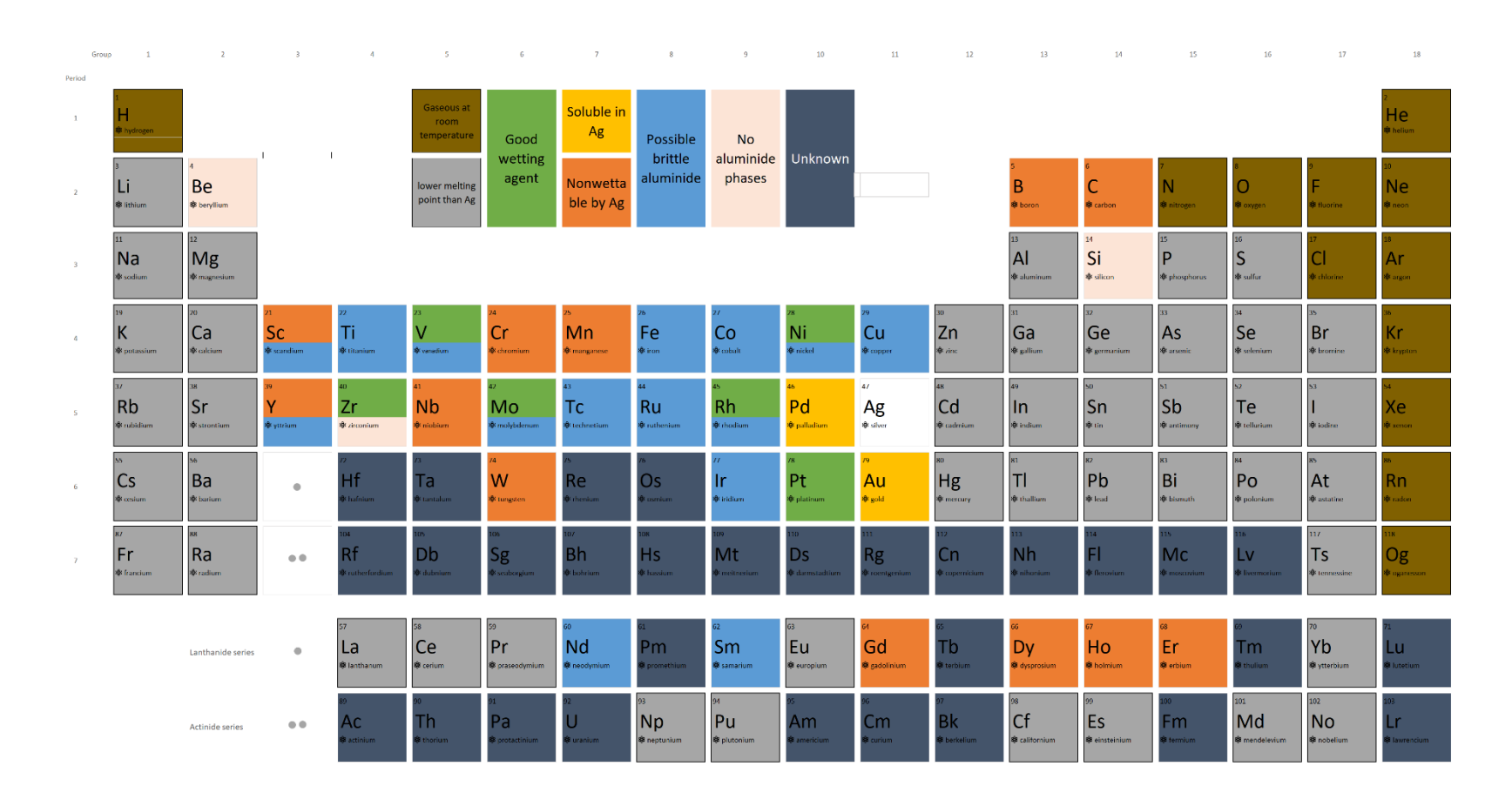


Figure 6-2 Candidate element search criteria and results labeled in the periodic table.

Figure 6-3 shows the phase diagrams of Ag-Ni [92], Ag-Pt [162, 163], Ag-Pd [164], and Ag-Cr [165] systems. As discussed in Section 2.1.2, when silver melts, there is approximately 1 wt.% of silver dissolving in nickel, leading to the formation of a reaction layer between silver and nickel. This reaction enhances the work of adhesion between the two materials. In the silverplatinum phase diagram, it is observed that there is solubility of silver in platinum, implying that when silver undergoes melting, it partially dissolves into the platinum interlayer, promoting favorable wetting behavior similar to the Ag-Ni system. Because silver and platinum do not exhibit complete mutual solubility, the majority of the silver filler material remains within the joint gap, while the platinum interlayer primarily remains in its solid state. On the other hand, as shown in the silver-palladium phase diagram in Figure 6-3(c), silver and palladium are inter-soluble to each other. Therefore, when silver melts, palladium cannot remain as a solid and restrain the designed wetting pattern. Figure 6-3(d) shows the phase diagram between silver and chromium, indicating little to no solubility of silver in chromium. Consequently, based on the phase diagram, chromium is not considered a suitable interlayer material for promoting wetting. The determination of whether other elements can serve as viable wetting promotion interlayers was also conducted by analyzing the respective phase diagrams.

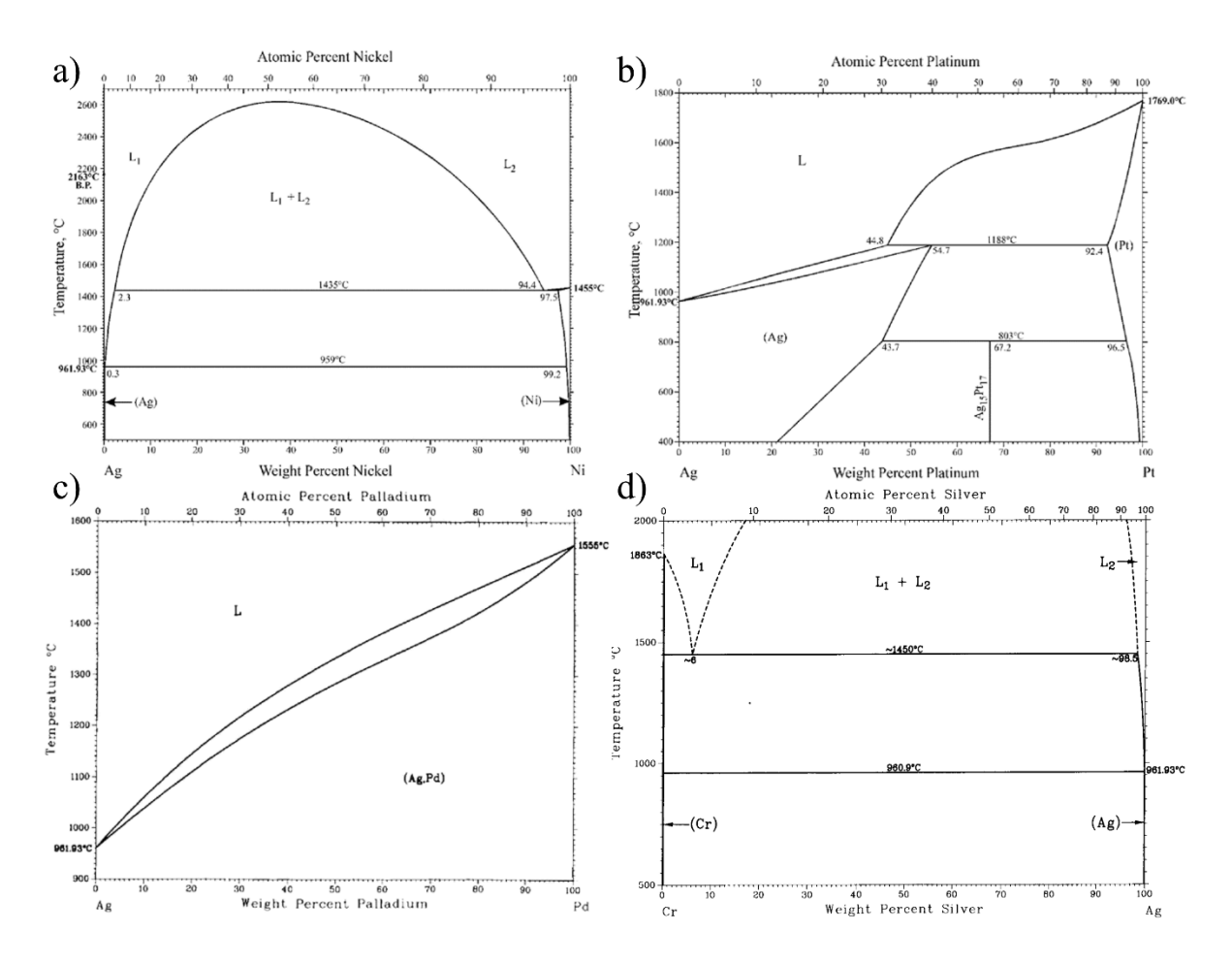


Figure 6-3 Phase diagrams of (a) Ag-Ni [92], (b) Ag-Pt [162, 163], (c) Ag-Pd [164], and (d) Ag-Cr [165] systems. In the Ag-Ni and Ag-Pt systems, there is a certain amount of silver dissolving in the other element, facilitating wetting while not forming a complete solid solution. Ag-Pd, however, can form a complete solid solution, leading to the removal of Pd if used as the interlayer. Considering that Ag does not dissolve in Cr, it is concluded that the wetting is poor.

Figure 6-4 shows the correlation between the normalized Cauchy pressure (obtained by dividing the Cauchy pressure (C<sub>12</sub>-C<sub>44</sub>) by the Young's modulus E) and Pugh's modulus ratio G/B, as described by Niu *et al.* [166]. Among the platinum aluminide phases with available elasticity data, it can be observed that they exhibit greater ductility compared to nickel, which has been established as a favorable interlayer material [65, 93, 94]. Therefore, employing platinum as a wetting interlayer on aluminum-coated/containing stainless steel is expected to yield the advantage of forming ductile platinum aluminide phases. This characteristic can help mitigate the challenge

of insulating alumina formation. For a detailed explanation of this ductility analysis diagram, please refer to APPENDIX B: METAL-ALUMINIDE DUCTILITY DETERMINATION.

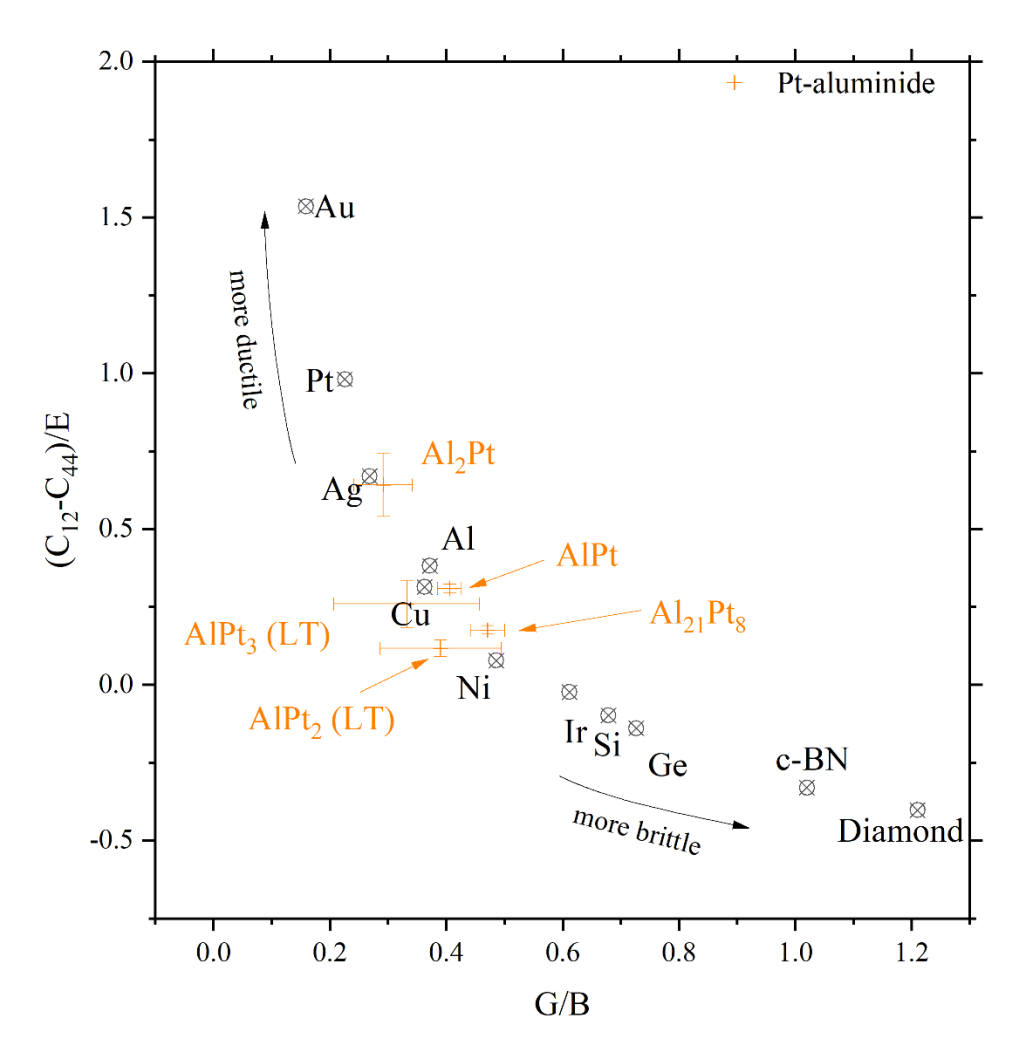


Figure 6-4 The ductility analysis diagram of platinum aluminide phases Al<sub>2</sub>Pt, AlPt, low temperature AlPt<sub>2</sub>, low temperature AlPt<sub>3</sub>, Al<sub>21</sub>Pt<sub>8</sub>. The phases towards the top left corner are more ductile. The phases towards the lower right corner are more brittle. The error bars associated with the platinum aluminide phases represent the data range resulting from the upper and lower limits of the moduli.

Hence, this chapter aims to analyze the mechanical and electrical performance, as well as the air annealing, redox and rapid thermal cycling durability, of Ag-Pt brazes applied to aluminum-containing stainless steel. The contents of this chapter were not published before this dissertation was submitted.

# **6.2 Microstructure Analyses**

### 6.2.1 <u>As-Produced Samples</u>

Figure 6-5(a) shows the back-scattered electron scanning electron microscopy image of the whole as-produced Ag-Pt braze joint cross-section. These samples were prepared by melting pure silver between Ag-Pt-mixed-particle-printed stainless steel substrates. Besides some pores near the ends of the braze at the 441 interfaces (which were due to reduced Pt particle densities resulting from imperfect screen printing), these samples are dense and crack-free. This shows that the silver platinum in the interlayer can help molten silver wet the stainless steel substrates and form good braze joints.

Figure 6-5(b) shows the representative cross-sectional BSE microstructural and EDS compositional analyses of the AFA interface. Three layers of phases exist between the AFA substrate and the silver braze. Specifically, a thin black phase is adjacent to the substrate, which is a mixture of aluminum oxide, iron oxide and chromium oxide based on the compositional line scan. Farther away from the AFA substrate, a platinum-rich phase retains near the interface. This platinum-rich phase is iron-doped platinum-aluminum intermetallic Fe-Pt<sub>2</sub>Al<sub>3</sub>. This is determined by the element ratio from the EDS spectra. Closer to the braze joint, a platinum-rich band exists, brighter than the iron-doped intermetallic, which is the Pt<sub>2</sub>Al<sub>3</sub> phase. This phase has a boundary with increased silver concentration, showing good wetting for molten silver.

The microstructural and compositional analyses show that the platinum in the interlayer can getter the aluminum in the aluminum-containing substrate to form intermetallic phases. The product can stabilize most of the aluminum and prevent the formation of excess insulating aluminum oxide.

Figure 6-5(c) shows the representative cross-sectional BSE microstructural and EDS compositional analyses of the 441 interface. Two layers of phases exist between the silver braze and 441 substrate. The platinum-aluminum intermetallic phase is adjacent to the silver braze joint. A metallurgical bond formed between the Pt-Al intermetallic phase and the substrate, with a gradual change of brightness and hence, the platinum and iron concentration. It is worth noting that some stainless steel diffused into the silver braze joint. This phenomenon was observed in other silver based stainless steel braze joint samples as well. It is attributed to the detachment of the hills of the rough stainless steel surface.

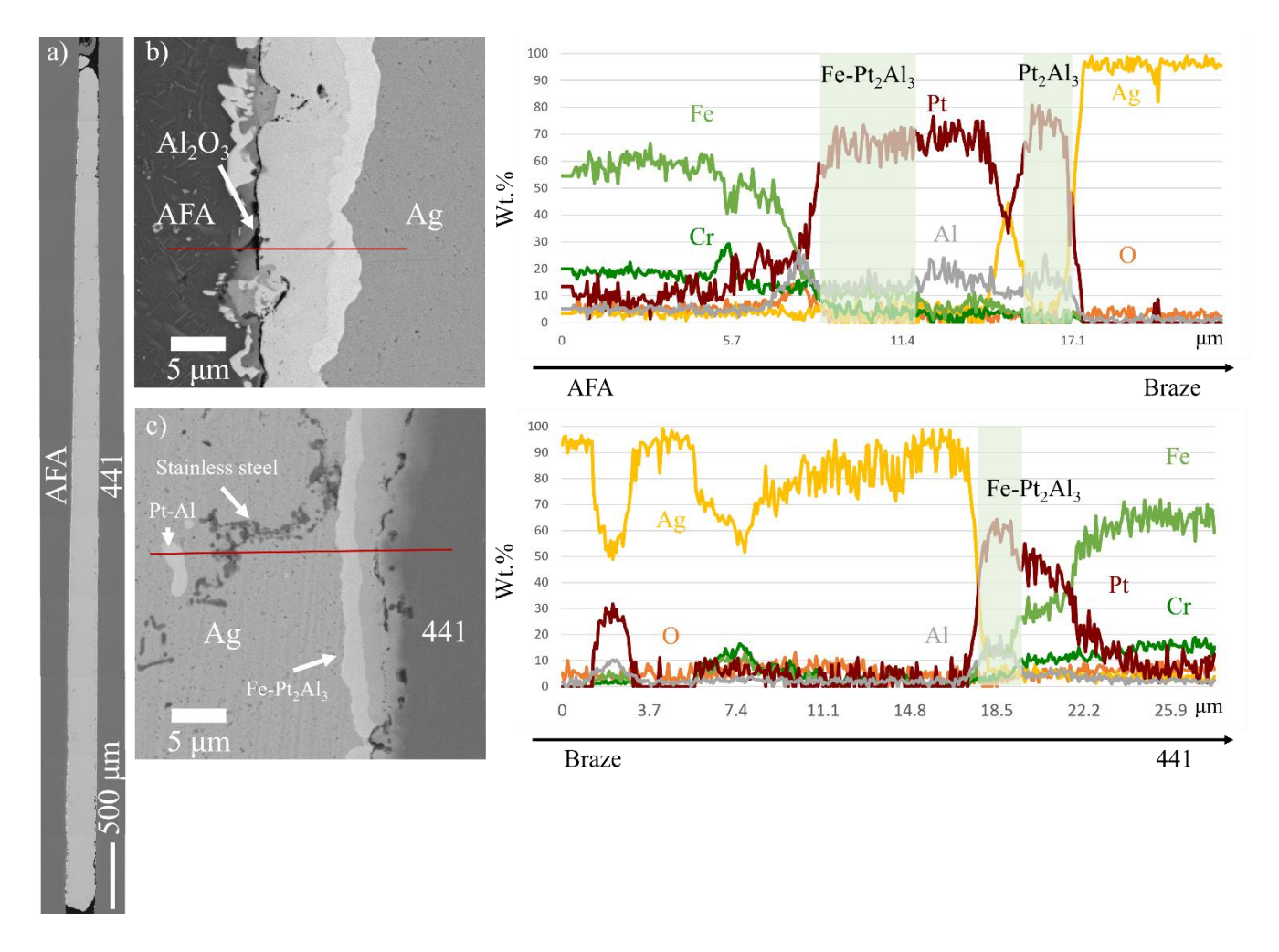


Figure 6-5 As-produced Ag-Pt braze joint back-scattered scanning electron microscopy image and energy dispersive X-ray spectroscopy line scans of (a) the whole joint, (b) the AFA interface, and (c) the 441 interface. In (b), an alumina phase exists between the AFA substrate and the braze joint. The Fe-Pt<sub>2</sub>Al<sub>3</sub> band and Pt<sub>2</sub>Al<sub>3</sub> band getter most of the aluminum. In (c), some aluminum diffuses and reacts with platinum in this interlayer.

### 6.2.2 Air Annealed Samples

Figure 6-6(a) shows the back-scattered scanning electron microscopy image of the whole air annealed Ag-Pt braze joint cross-section. The braze joint remains mostly dense and well adhered to both substrates. Some pores exist on the 441 side, which was also observed in the asproduced samples. These defects are attributed to the reduced platinum density during screen printing in the paste near the edge of the pattern.

Figure 6-6(b) shows the representative cross-sectional BSE microstructural and EDS compositional analyses of the AFA interface. The platinum rich cluster has the same composition as the as-produced sample. A black line is observed between the platinum rich phase and the silver braze joint, which has the composition of aluminum oxide. Some stainless steel pieces are also detected in the silver joint. This air annealed result shows that the aluminum gettering is stable. After 300 hours of air annealing, only a thin layer of aluminum oxide forms. Most of the aluminum phase is still stabilized in the Pt<sub>2</sub>Al<sub>3</sub> phase.

Figure 6-6(c) shows the representative cross-sectional BSE microstructural and EDS compositional analyses of the 441 interface. A continuous layer of aluminum oxide forms between silver and the original interlayer. The Pt-Al and stainless steel reaction layer transferred to Pt-Fe-Cr mixture and aluminum oxide. An aluminum oxide layer forms at the interface between the original interlayer and the substrate, separating the two layers. The results show that on the 441 stainless steel side, the gettering is less stable. The metallurgical bond between Pt<sub>2</sub>Al<sub>3</sub> and stainless steel will decompose to form aluminum oxide after air annealing. The electrical measurement results will be presented for the evaluation of the composition and aluminum oxide formation.

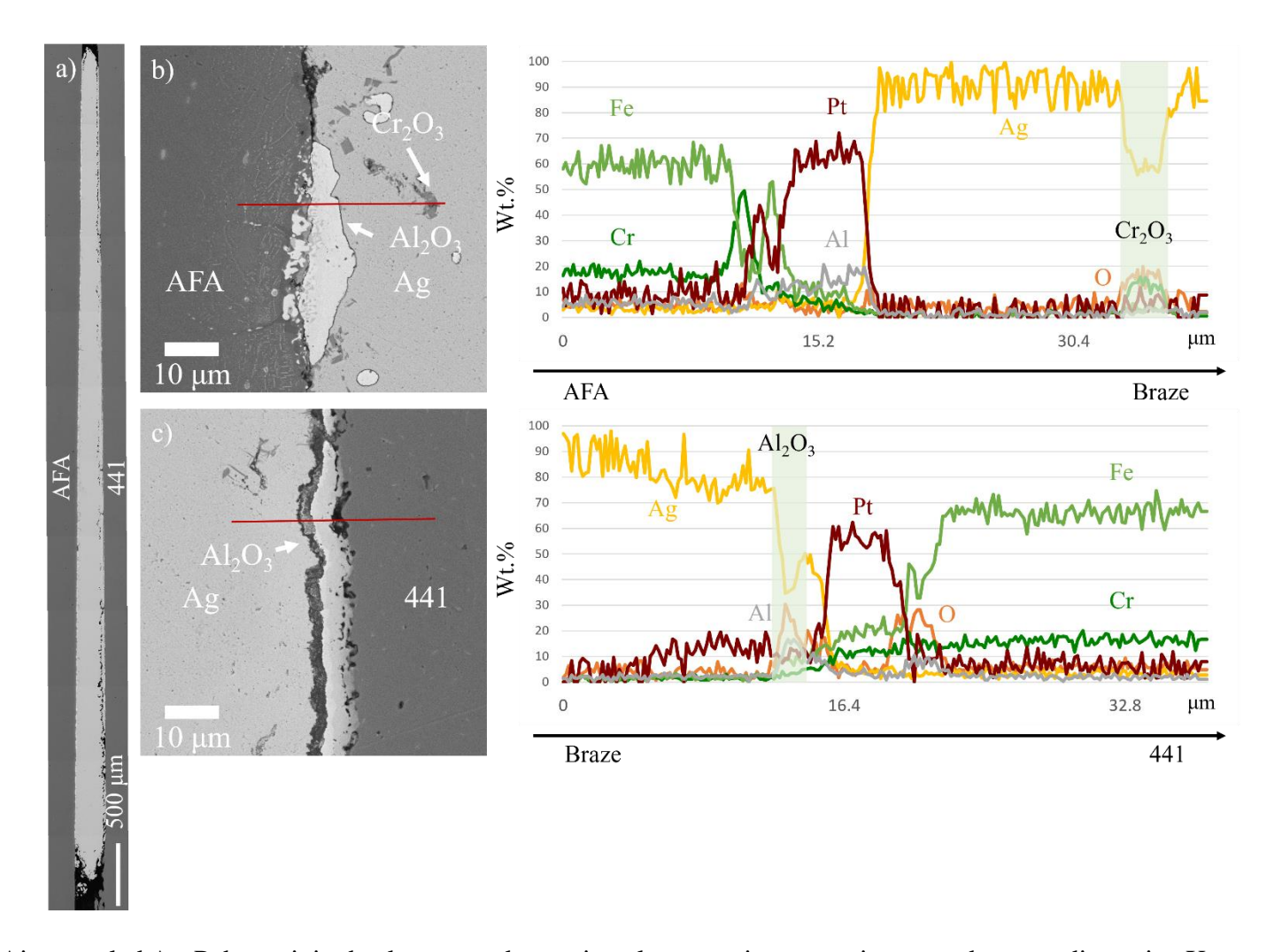


Figure 6-6 Air annealed Ag-Pt braze joint back-scattered scanning electron microscopy image and energy dispersive X-ray spectroscopy line scans of (a) the whole joint, (b) the AFA interface, and (c) the 441 interface. A thin black line exists in (b) between silver and the Pt-rich phase. It is a thin layer of alumina, which is too thin to be detected by the EDS line scan. No significant alumina phase is detected in the spectra.

## 6.2.3 Redox Cycled Samples

Figure 6-7(a) shows the BSE SEM image of the whole redox cycled AFA|Pt|Ag|Pt|441 braze cross-sectional area. The braze is totally detached from the 441 stainless steel due to the vibration during cutting. The braze is mostly detached from the AFA substrate. The bent structure indicates ductility in the silver-based joint; however, the interfaces exhibit weakness and lead to delamination. The silver braze is broken with interconnected voids. Figure 6-7(c-d) shows the zoomed in microstructure. This phenomenon was first observed by Klueh and Mullins [80]. The hydrogen diffused into the silver and reacted with the dissolved oxygen at the silver grain boundaries. Therefore, after 25 redox cycles, water pockets form at the grain boundaries and coalesce into interconnected voids, which eventually led to structural degradation.

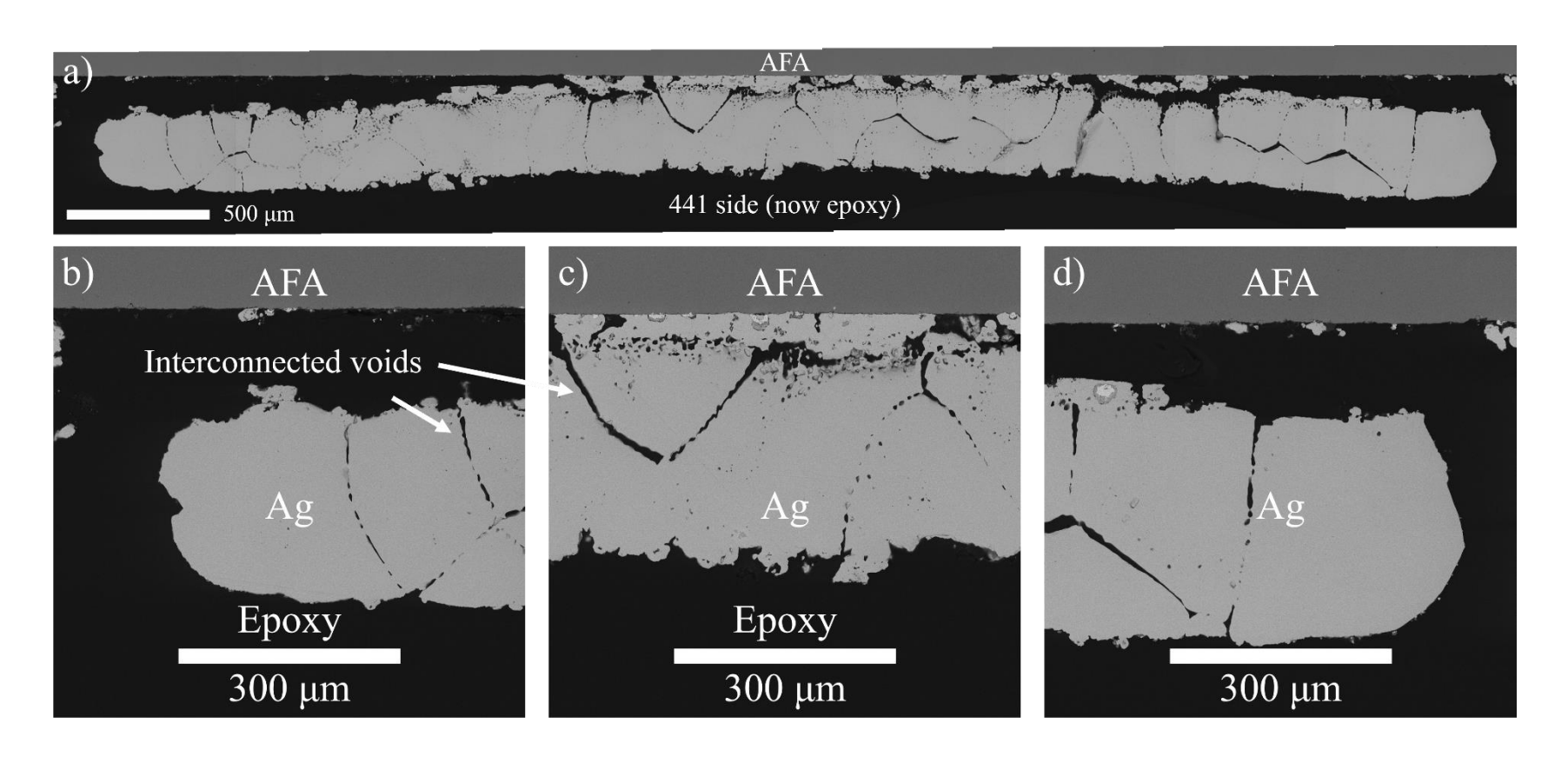


Figure 6-7 Redox cycled Ag-Pt braze joint back-scattered scanning electron microscopy image of (a) the whole joint, (b) the left end region, (c) the middle region, and (d) the right end region. The silver joint is full of interconnected voids.

# 6.2.4 Extremely Rapid Thermal Cycled Samples

Figure 6-8 shows the BSE SEM image of the whole rapid thermal cycled AFA|Pt|Ag|Pt|441 braze cross-sectional area. The silver brazing material exhibit severe fragmentation between the substrates, with only a small fraction remaining attached. The majority of the silver detach completely from the substrate. These findings indicate that the extremely rapid thermal cycles subjected to the samples induce significant thermal shock, resulting in a substantial degradation of the microstructure integrity. Chou and Stevenson [167] observed that the leak rate of a silver seal was found to deteriorate with thermal cycling. This deterioration was attributed to the development of cracks along the grain boundaries.

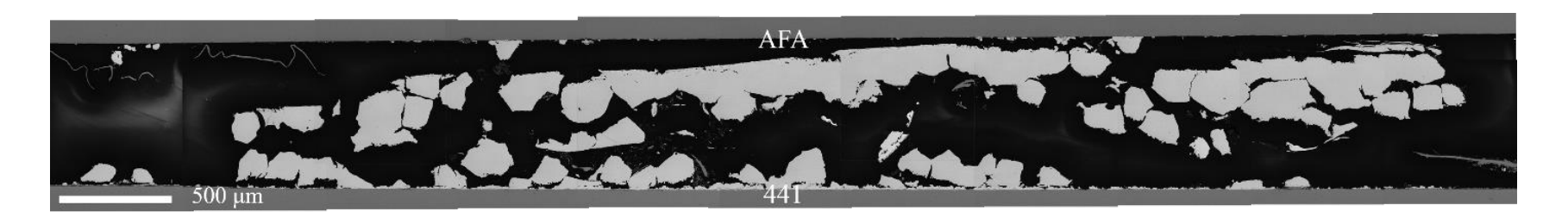


Figure 6-8 Rapid thermal cycled Ag-Pt braze joint back-scattered scanning electron microscopy image of the whole joint. The silver joint breaks into clusters of isolated silver pieces due to the extremely rapid thermal cycles.

### **6.3 Shear Strength Results**

Table 9 shows the shear strength of Ag-Pt AFA|441 samples in as-produced, 650°C 300-hour air annealed, 25 redox cycled, and 300 rapid thermal cycled states.

Table 9 Shear strength of Ag-Pt AFA|441 samples in different states. Samples in each group are prepared using identical procedures. The numbering merely serves as a means of differentiation between the samples.

Conditions	Shear strength (MPa)						
	Sample1	Sample2	Sample3	Sample4	Sample5	Sample6	
As-Produced	15.7	16.6	16.9	17.0	17.4	22.6	
Air Annealed	42.6	48.3	64.5	69.7	N/A	N/A	
Redox Cycled	18.3	20.8	22.2	23.5	25.4	N/A	
Rapid Thermal Cycled	5.9	6.2	12.2	25.4	28.6	N/A	

In the as-produced state, the Ag-Pt braze exhibit consistent mechanical performance. The shear strength values display a relatively centered distribution, with the highest value recorded as 22.6 MPa and the lowest value as 15.7 MPa. The survival probability of a given sample in a batch can be determined using the method detailed in Subchapter 4.2. Then the strength of a specific survival probability can be determined. The shear strength at 99% survival probability is determined to be 9.4 MPa. Failure of the as-produced samples primarily occurred at the braze-substrate interface, with a higher frequency at the 441 interface compared to the AFA interface.

After air annealing, the strength significantly increases, with the highest recorded value reaching 69.7 MPa. The shear strength at 99% survival probability is 20.6 MPa. Most of the air annealed samples experienced failure within the silver braze, with two instances of delamination occurring at the 441 interface.

After 25 redox cycles, the strength exhibits a decrease compared to the air annealed samples but remains higher than the as-produced state. The strongest sample from the redox cycled group failed at 25.4 MPa, while the shear strength at 99% survival probability is determined as 13.4 MPa. Similar to the air annealed samples, failure mostly occurred within the silver braze, with two instances of delamination observed at the AFA interface.

After 300 rapid thermal cycles, a broad distribution of strength is observed. The highest strength recorded was 28.6 MPa, which is over four times higher than the weakest sample. Consequently, the shear strength at 99% survival probability is calculated as 0.5 MPa. 70% of the failures occurred within the braze, with the remaining 30% attributed to failures at the AFA interface.

# **6.4 Contact Resistivity Results**

Table 10 shows the contact resistivity of Ag-Pt braze joints between the same type of stainless steel substrates.

Table 10 The contact resistivity of Ag-Pt braze joints between AFA|AFA or 441|441 same type of substrates in different states. Samples in each group are prepared using identical procedures. The numbering merely serves as a means of differentiation between the samples.

	Contact resistivity ( $\Omega \cdot \text{cm}^2$ )					
Conditions	AFA AFA			441 441		
	Sample1	Sample2	Sample3	Sample1	Sample2	Sample3
As-Produced	3.6×10 <sup>-5</sup>	3.5×10 <sup>-5</sup>	3.4×10 <sup>-5</sup>	1.3×10 <sup>-5</sup>	1.6×10 <sup>-5</sup>	6.3×10 <sup>-5</sup>
Air Annealed	$3.4 \times 10^{-3}$	$2.0 \times 10^{-3}$	$1.0 \times 10^{-2}$	1.1×10 <sup>-3</sup>	5.0×10 <sup>-4</sup>	1.3×10 <sup>-4</sup>
Redox Cycled	4.2×10 <sup>-4</sup>	5.6×10 <sup>-4</sup>	7.8×10 <sup>-4</sup>	$1.9 \times 10^{-3}$	$1.5 \times 10^{-3}$	1.1×10 <sup>-3</sup>
Rapid Thermal Cycled	1.2×10 <sup>-4</sup>	1.8×10 <sup>-4</sup>	1.0×10 <sup>-3</sup>	8.0×10 <sup>-4</sup>	1.1×10 <sup>-3</sup>	1.5×10 <sup>-4</sup>

The contact resistivity of Ag-Pt between AFA|AFA and 441|441 are similar in the asproduced condition. They were both between  $10^{-5}$ - $10^{-4} \Omega \cdot \text{cm}^2$ .

After air annealing, the resistivity between the substrates increases for both cases. However, the resistivity between 441|441 is smaller compared to the AFA|AFA counterpart. Specifically, after air annealing, the contact resistivity between AFA|AFA increases to a value larger than  $10^{-3}$   $\Omega$ •cm<sup>2</sup>, while the contact resistivity between 441|441 increases to a value larger than  $10^{-4}$   $\Omega$ •cm<sup>2</sup>. This indicates that the formation of aluminum oxide in the AFA interface poses a greater challenge compared to the formation of chromium oxide in the 441 interface.

After redox cycling, the contact resistivity in both groups is observed to be around  $10^{-3}$   $\Omega$ •cm<sup>2</sup>. This suggests that despite the presence of interconnected voids, which may lead to more electron scattering, the interfacial resistivity remains low after undergoing redox cycling.

After rapid thermal cycling, the contact resistivity in both groups range between  $10^{-4}$  and  $10^{-3} \ \Omega$ •cm<sup>2</sup>. Despite the occurrence of delamination and a fractured silver microstructure, the resistivity remained low.

# 6.5 Ag-Pt Joints for Ceramic-Steel Brazing

Other than the application for aluminum-containing stainless steel brazing, silver-platinum can also be utilized for ceramic-stainless steel brazing applications.

The Ag-Pt YSZ-441 stainless steel samples were prepared and characterized by melting silver foil between silver-platinum-printed commercial 8mol.% yttria-stabilized zirconia (8YSZ) and 441 stainless steel. Specifically, silver-platinum paste was prepared by mixing 325 mesh 99.99% platinum powder, 325 mesh 99.9% silver powder, and Heraeus V737 polymeric vehicle in a 1:3:2 weight ratio. The paste was printed on 240-grit-silicon-carbide-polished YSZ (AdValue Tech;

Tucson AZ, USA) and 441SS. The platinum printed YSZ was pre-sintered and then the braze assembles were fired to melt silver.

Figure 6-9 shows the fractured as-produced YSZ-441 samples on the test machine. The samples fractured within the YSZ bars, which indicates that the braze is stronger than 11 MPa.

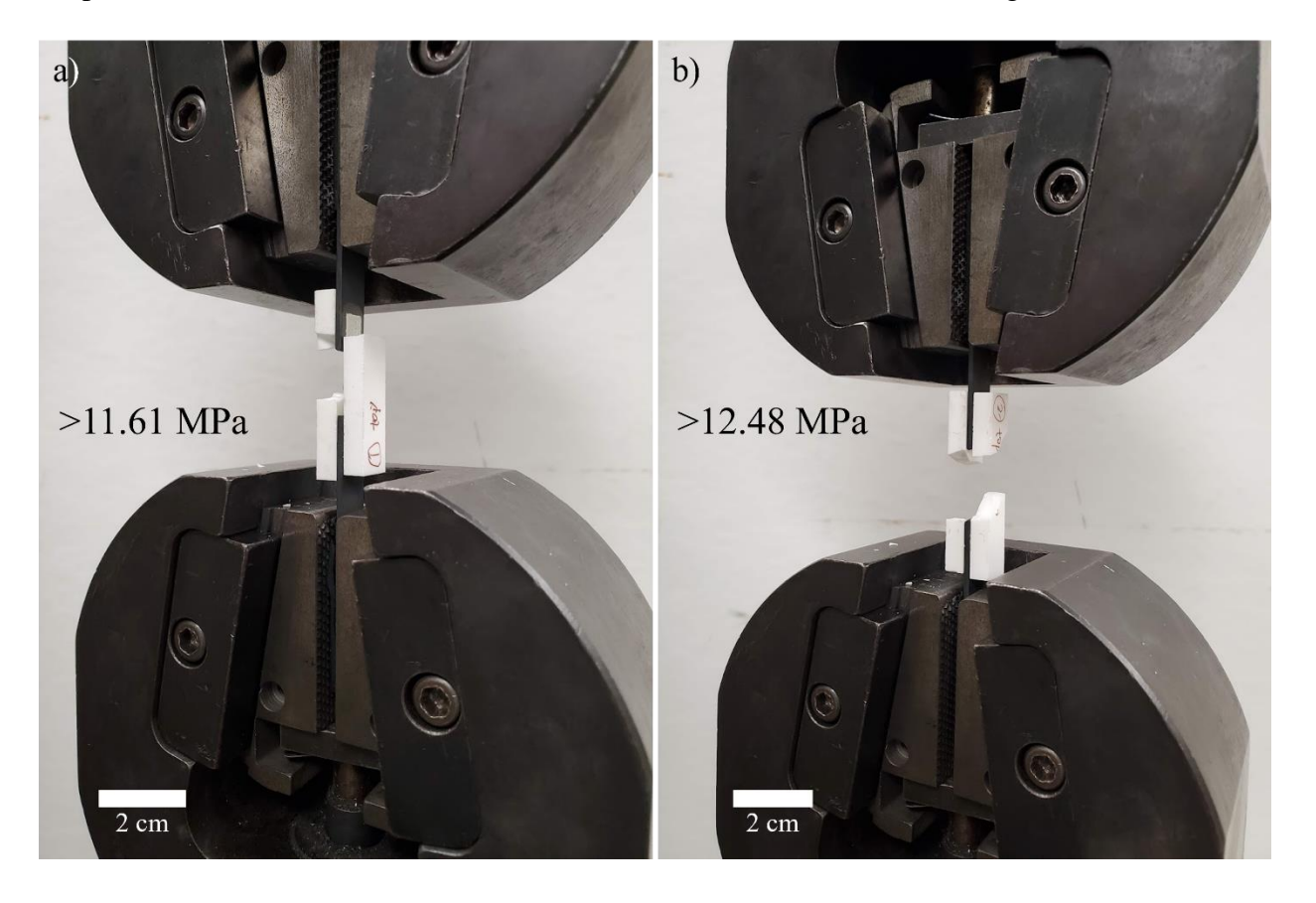


Figure 6-9 Fractured as-produced 441-YSZ double shear lap samples.

Figure 6-10 shows the cross-sectional BSE SEM images and energy-dispersive x-ray spectroscopy line scans of the Ag-Pt YSZ-441 sample. The braze is dense. Platinum segregates to the 441 interface and forms PtZr<sub>2</sub>-(FeCr)<sub>x</sub>. The results show that platinum can be used as the interlayer material to produce dense silver-based brazes between stainless steel and ceramic. This braze exhibits higher bonding strength than the base YSZ substrate.

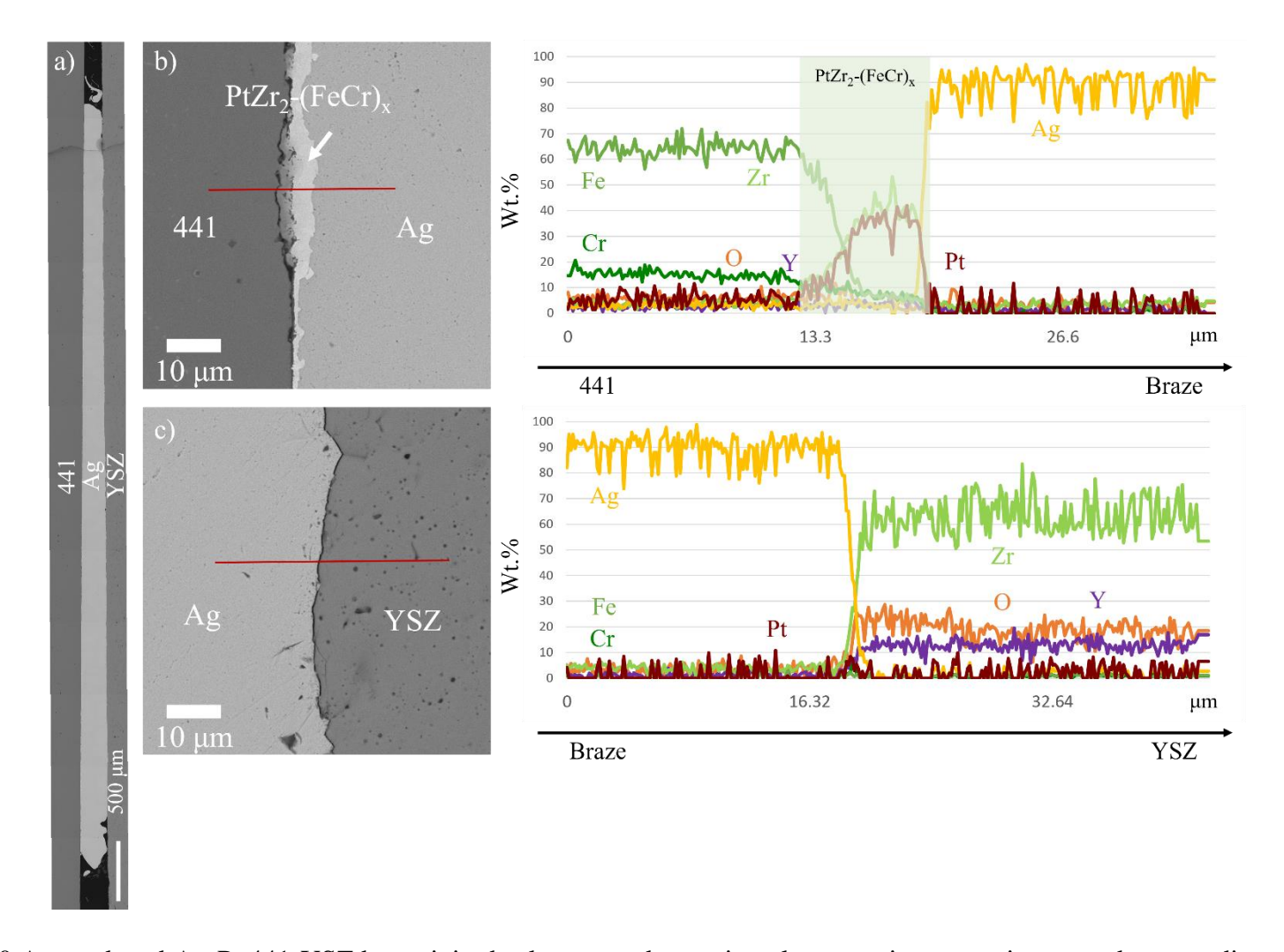


Figure 6-10 As-produced Ag-Pt 441-YSZ braze joint back-scattered scanning electron microscopy image and energy dispersive X-ray spectroscopy line scan of (a) the whole joint, (b) the 441 interface, and (c) the YSZ interface. The bright phase in (b) is the reaction product between Pt in the interlayer and Zr from the YSZ substrate.

# 6.6 Discussion

Figure 6-11 shows a Weibull plot comparing the shear strength of as-produced, air annealed, redox cycled, and rapid thermal cycled Ag-Ni, Ag-Pt, and Ag-CuO samples.

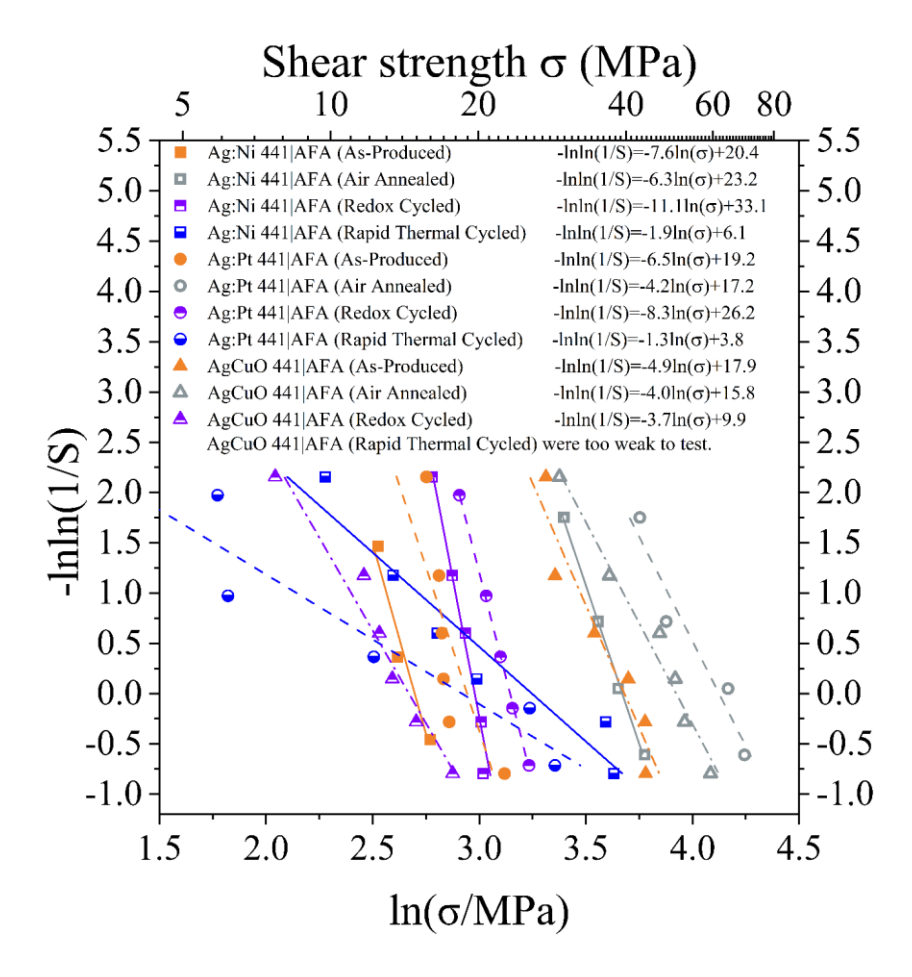


Figure 6-11 Weibull plot of Ag-Ni, Ag-Pt, and Ag-CuO AFA|441 braze samples in as-produced, air annealed, redox cycled, and rapid thermal cycled conditions.

In the as-produced state, the strength of Ag-Pt samples surpasses that of Ag-Ni samples, yet remains weaker compared to the Ag-CuO samples. Ag-Pt samples exhibit higher strength than Ag-Ni samples mainly due to the higher work of adhesion between platinum and the substrate than that between nickel and the substrate. Figure 6-12 shows the measured work of adhesion and calculated van der Waals energy of eight FCC metals on alumina. Platinum has a higher work of adhesion than nickel. While this result was observed on alumina, it is reasonable to assume that

when applied to aluminum-containing stainless steel, the surface will possess an alumina scale. Consequently, the work of adhesion between platinum and the substrate is higher than that between nickel and the substrate. Ag-Pt samples exhibit lower strength than Ag-CuO samples because Ag-CuO samples are prepared in air, which contain more oxygen at the interface than the Ag-Pt samples.

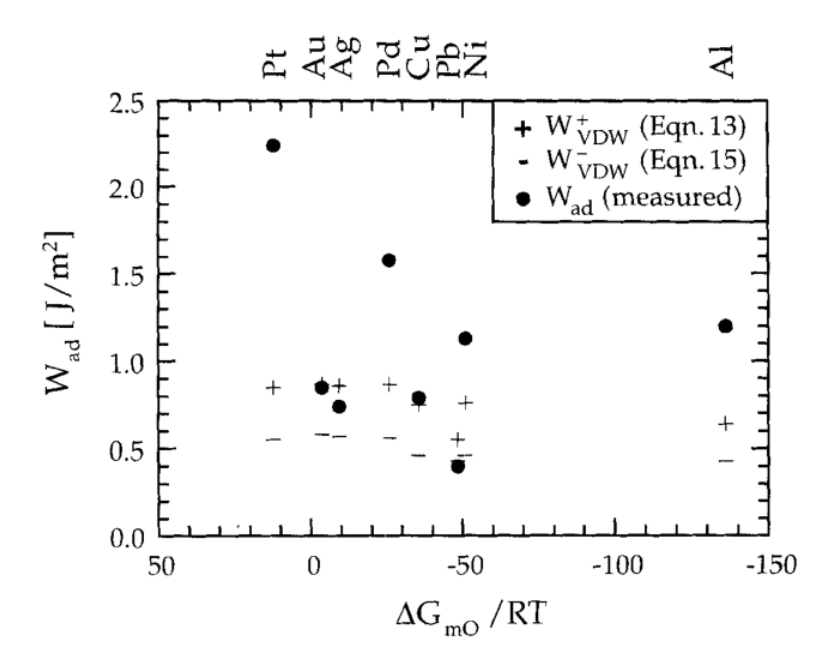


Figure 6-12 Measured work of adhesion and calculated van der Waals energy of eight FCC metals on alumina substrate. The x-axis denotes the chemical activity of FCC metal oxide formation [154].

After air annealing, the Ag-Pt samples exhibit superior strength compared to all other samples, including the robust air annealed Ag-CuO samples. This can be attributed to the high work of adhesion between platinum and the substrate.

After redox cycling, the shear strength slightly decreases compared to the as-produced and air annealed conditions but remains superior to Ag-Ni and Ag-CuO samples under the same conditions. This change is attributed to the initially high bonding strength between Ag-Pt joints and the substrates. Despite the deteriorated microstructure after redox cycling as shown in Figure

6-7, the strength can remain high. It is worth noting that further cycles may lead to strength deterioration based on the microstructure analysis.

Regarding the shear strength after rapid thermal cycles, caution is advised when considering applications that require extremely rapid thermal cycling. The presence of fractured silver in the microstructure is observed as shown in Figure 6-8, which is attributed to the high solubility of platinum in silver. This solid solution formation renders the material more brittle compared to pure silver. Further analysis and investigation are essential to comprehend the implications of this fractured microstructure and its potential impact on the long-term performance and reliability of the brazed joints.

Figure 6-13 shows the contact resistivity of as-produced, air annealed, redox cycled, and rapid thermal cycled Ag-Ni, Ag-Pt, and Ag-CuO samples between same stainless steel substrates. In all four conditions, the Ag-Pt samples displayed low resistivity, particularly in the case of 441 stainless steel bonding.

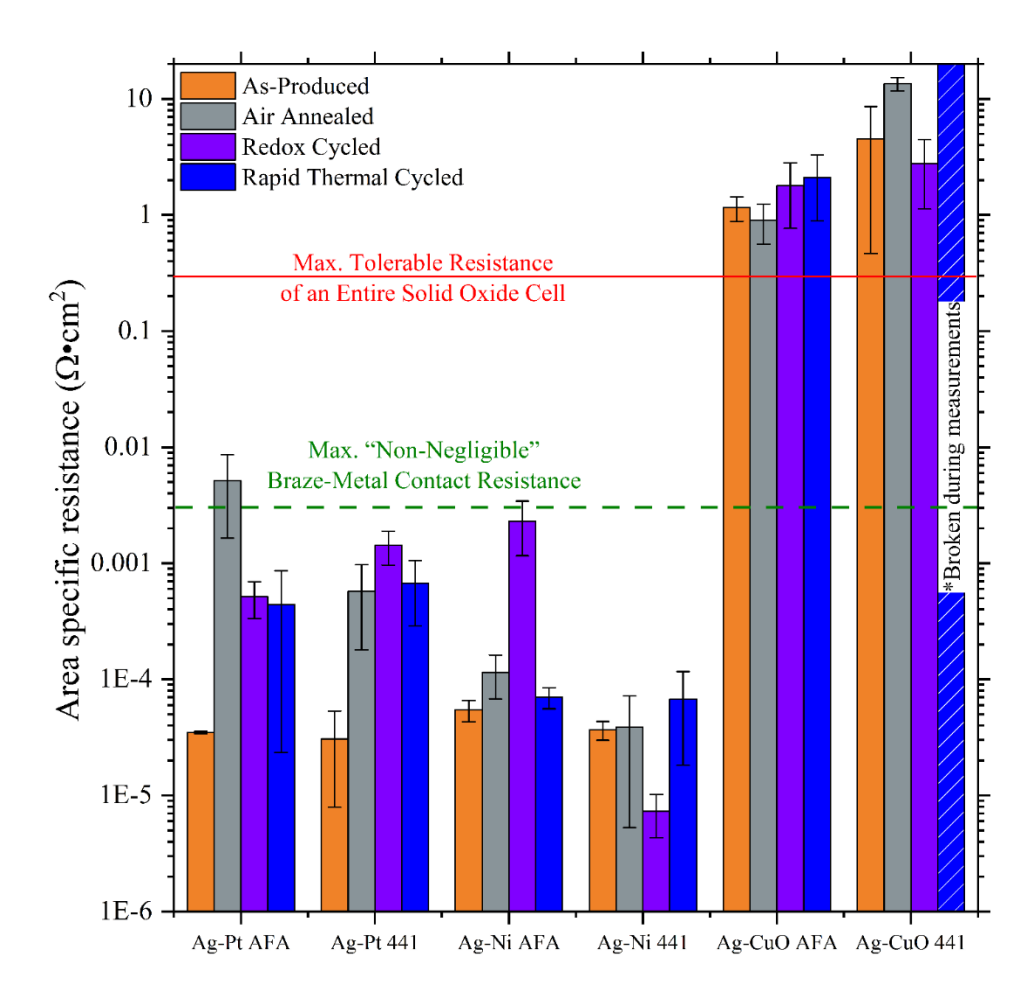


Figure 6-13 Contact resistivity of as-produced, air annealed, redox cycled, and rapid thermal cycled Ag-Ni, Ag-Pt, and Ag-CuO samples between same stainless steel substrates. All the Ag-CuO 441-441 samples broke during removing the surface oxide.

The low resistivity observed in the Ag-Pt samples is primarily attributed to the effective and stable aluminum gettering effect. This effect prevents the formation of insulating alumina, enhancing the electrical conductivity. After air annealing, only a thin black line was observed, indicating that a significant portion of the aluminum remains in the platinum-rich phase. Similarly to the Ag-Ni samples, a metallurgical bond is also formed on the 441 stainless steel side, ensuring good electron conductivity in the joint. The combination of these factors contributes to the favorable electrical properties exhibited by the Ag-Pt samples, making them promising candidates for high-performance applications in oxidizing environments.

## **6.7 Summary**

Chapter 6 focuses on the evolution of microstructure, shear strength, and contact resistivity of Ag-Pt brazes for AFA and 441 bonding applications. The chapter also explores the application of brazing ceramic and stainless steel materials with Ag-Pt brazes.

Remarkably, the Ag-Pt brazing technique demonstrates superior shear strength compared to its counterparts, namely Ag-Ni, Ag-CuO, and Heraeus C8710 techniques, particularly in the airannealed condition. Moreover, it exhibits an aluminum getter effect, effectively eliminating insulating alumina when applied to aluminum-containing stainless steel. This gettering effect remains stable, resulting in consistently low resistivity between substrates with Ag-Pt joints, regardless of whether they are in as-produced, air-annealed, redox cycled, or rapid thermal cycled conditions. These findings are highly valuable for researchers seeking a durable, well-adhered, and highly conductive brazing solution suitable for oxidizing environments.

#### 7 Conclusions

In summary, this dissertation investigated the mechanical and electrical performance of Ag-Ni brazes and interconnects made with the Particle Interlayer Directed Wetting and Spreading technique. When applied to aluminum containing stainless steel, the new benefit of Ag-Ni braze is that it can stably getter aluminum from the substrate and enhance the contact resistivity. The research also investigated a new novel Ag-Pt brazing technique. The shear strength, contact resistivity, and microstructure change in as-produced, air annealed, redox cycled, and rapid thermal cycled conditions were evaluated.

The Ag-Ni circuits demonstrated comparable sheet resistivity on alumina and contact resistivity on LSM, in comparison to commercially available silver paste products. Notably, the Ag-Ni circuits exhibited significantly improved bonding strength compared to their counterparts, making them a promising solution for high-performance circuits and current collectors in high-temperature devices.

This research showed that the Ag-Ni braze can effectively getter aluminum from the substrate and prevent the insulating alumina scale, providing an added advantage in applications involving aluminum containing stainless steel. The double shear lap shear strength, contact resistivity, and microstructure changes of Ag-Ni brazes between AFA and 441 stainless steel under different conditions was investigated in as-produced, air annealed, redox cycled, and rapid thermal cycled states. Comparative evaluations were also conducted with Ag-CuO brazes (in the aforementioned conditions) and Heraeus C8710 brazes (as-produced and air annealed). The results demonstrated that Ag-Ni brazes exhibited satisfactory mechanical strength and low contact resistivity across all tested conditions. The stability of the microstructure was generally maintained, except in severe rapid thermal cycling, where interfacial cracking and delamination happened.

These findings highlight the potential of the Ag-Ni brazing technique in mitigating the chromium poisoning issue in applications requiring aluminum-containing stainless steel.

The dissertation examined a novel Ag-Pt brazing technique and investigated its shear strength, contact resistivity, and microstructure changes in as-produced, air annealed, redox cycled, and rapid thermal cycled conditions. The findings revealed that Ag-Pt brazes exhibited improved mechanical performance in oxidized environments compared to Ag-Ni brazes. The resistivity remained consistently low across all test conditions. However, it was observed that reducing environments could lead to the formation of pores. Moreover, caution was advised in applications requiring rapid thermal cycling, as Ag fracture was observed under such conditions.

In conclusion, this dissertation provides insights into the performance and suitability of different brazing techniques. Ag-Ni brazes demonstrated superior bonding strength to commercial products and comparable resistivity, while Ag-Pt brazes showed enhanced mechanical performance in oxidized environments.

For applications requiring excellent mechanical and electrical performance in reducing environments, the Ag-Ni brazing technique is recommended. Its superior bonding strength and comparable resistivity make it a suitable choice for a wide range of applications. In contrast, for applications that demand good mechanical and electrical performance in oxidizing environments, the Ag-Pt brazing technique offers significant advantages. Its improved mechanical performance in such environments ensures the reliability and longevity of bonded structures.

The findings of the dissertation contribute significantly to the understanding of brazing materials and their application considerations. The insights gained from this research will facilitate the development of advanced bonding solutions for various applications, including SOFCs, SOECs, aerospace turbine blades, solar cells, and other devices. By improving the longevity and

reliability of these devices, the research findings hold promise for the generation of clean energy and may also offer a potential solution for providing oxygen in human extraterrestrial exploration scenarios.

#### **BIBLIOGRAPHY**

- 1. United Nations. *Ensure Access to Affordable, Reliable, Sustainable and Modern Energy*. 2023; Available from: <a href="https://www.un.org/sustainabledevelopment/energy/">https://www.un.org/sustainabledevelopment/energy/</a>.
- 2. United Nations. *Causes and Effects of Climate Change*. 2023; Available from: <a href="https://www.un.org/en/climatechange/science/causes-effects-climate-change">https://www.un.org/en/climatechange/science/causes-effects-climate-change</a>.
- 3. J.D. Nicholas, *Highlights from the 2013 National Science Foundation Solid Oxide Fuel Cell Promise, Progress, and Priorities (SOFC-PPP) Workshop.* The Electrochemical Society Interface, 2013. **22**(4): p. 49-54 DOI: <a href="https://doi.org/10.1149/2.F04134if">https://doi.org/10.1149/2.F04134if</a>.
- 4. Z. Gao, L.V. Mogni, E.C. Miller, J.G. Railsback, and S.A. Barnett, *A Perspective on Low-Temperature Solid Oxide Fuel Cells*. Energy Environmental Science, 2016. **9**(5): p. 1602-1644 DOI: <a href="https://doi.org/10.1039/C5EE03858H">https://doi.org/10.1039/C5EE03858H</a>.
- 5. K.W. Bedringås, I.S. Ertesvåg, S. Byggstøyl, and B.F. Magnussen, *Exergy Analysis of Solid-Oxide Fuel-Cell (SOFC) Systems*. Energy, 1997. **22**(4): p. 403-412 DOI: https://doi.org/10.1016/S0360-5442(96)00119-3.
- 6. S.H. Chan, C.F. Low, and O.L. Ding, *Energy and Exergy Analysis of Simple Solid-Oxide Fuel-Cell Power Systems*. Journal of Power Sources, 2002. **103**(2): p. 188-200 DOI: https://doi.org/10.1016/S0378-7753(01)00842-4.
- 7. K. Hosoi and M. Nakabaru, *Status of National Project for SOFC Development in Japan*. ECS Transactions, 2009. **25**(2): p. 11 DOI: <a href="https://doi.org/10.1149/1.3205503">https://doi.org/10.1149/1.3205503</a>.
- 8. S.C. Kaushik, V.S. Reddy, and S.K. Tyagi, *Energy and Exergy Analyses of Thermal Power Plants: A Review*. Renewable and Sustainable Energy Reviews, 2011. **15**(4): p. 1857-1872 DOI: <a href="https://doi.org/10.1016/j.rser.2010.12.007">https://doi.org/10.1016/j.rser.2010.12.007</a>.
- 9. E.D. Wachsman and K.T. Lee, *Lowering the Temperature of Solid Oxide Fuel Cells*. Science, 2011. **334**(6058): p. 935-939 DOI: <a href="https://doi.org/10.1126/science.1204090">https://doi.org/10.1126/science.1204090</a>.
- 10. S. McIntosh and R.J. Gorte, *Direct Hydrocarbon Solid Oxide Fuel Cells*. Chemical Reviews, 2004. **104**(10): p. 4845-4866 DOI: <a href="https://doi.org/10.1021/cr020725g">https://doi.org/10.1021/cr020725g</a>.
- 11. A. Choudhury, H. Chandra, and A. Arora, *Application of Solid Oxide Fuel Cell Technology for Power Generation—A Review*. Renewable and Sustainable Energy Reviews, 2013. **20**: p. 430-442 DOI: https://doi.org/10.1016/j.rser.2012.11.031.
- 12. O. Yamamoto, *Solid Oxide Fuel Cells: Fundamental Aspects and Prospects*. Electrochimica Acta, 2000. **45**(15): p. 2423-2435 DOI: <a href="https://doi.org/10.1016/S0013-4686(00)00330-3">https://doi.org/10.1016/S0013-4686(00)00330-3</a>.
- 13. Y. Zhang and J.D. Nicholas, *Updating the Notion that Poor Cathode Performance Typically Dominates Overall Solid Oxide Fuel Cell Response.* Journal of The

- Electrochemical Society, 2021. **168**(3): p. 034513 DOI: <a href="https://doi.org/10.1149/1945-7111/abed21">https://doi.org/10.1149/1945-7111/abed21</a>.
- 14. R. Vinoth Kumar and A.P. Khandale, *A Review on Recent Progress and Selection of Cobalt-Based Cathode Materials for Low Temperature-Solid Oxide Fuel Cells*. Renewable and Sustainable Energy Reviews, 2022. **156**: p. 111985 DOI: <a href="https://doi.org/10.1016/j.rser.2021.111985">https://doi.org/10.1016/j.rser.2021.111985</a>.
- 15. K. Ding, M. Zhu, Z. Han, V. Kochetov, L. Lu, and D. Chen, *Momentum-Species-Heat-Electrochemistry Distribution Characteristics within Solid Oxide Fuel Cell Stack with Complex Inter-Digital Fuel Channels*. Ionics, 2020. **26**(9): p. 4567-4578 DOI: <a href="https://doi.org/10.1007/s11581-020-03602-9">https://doi.org/10.1007/s11581-020-03602-9</a>.
- 16. A.S. Deepi, S. Dharani Priya, A. Samson Nesaraj, and A.I. Selvakumar, *Component Fabrication Techniques for Solid Oxide Fuel Cell (SOFC) A Comprehensive Review and Future Prospects*. International Journal of Green Energy, 2022. **19**(14): p. 1600-1612 DOI: https://doi.org/10.1080/15435075.2021.2018320.
- 17. S.M. Jamil, M.H.D. Othman, M.A. Rahman, J. Jaafar, A.F. Ismail, and K. Li, *Recent Fabrication Techniques for Micro-Tubular Solid Oxide Fuel Cell Support: A Review.* Journal of the European Ceramic Society, 2015. **35**(1): p. 1-22 DOI: <a href="https://doi.org/10.1016/j.jeurceramsoc.2014.08.034">https://doi.org/10.1016/j.jeurceramsoc.2014.08.034</a>.
- 18. M.Z. Khan, A. Iltaf, H.A. Ishfaq, F.N. Khan, W.H. Tanveer, R.-H. Song, M.T. Mehran, M. Saleem, A. Hussain, and Z. Masaud, *Flat-Tubular Solid Oxide Fuel Cells and Stacks: A Review*. Journal of Asian Ceramic Societies, 2021. **9**(3): p. 745-770 DOI: <a href="https://doi.org/10.1080/21870764.2021.1920135">https://doi.org/10.1080/21870764.2021.1920135</a>.
- 19. N.P. Brandon and M.A. Parkes, *Fuel Cells: Materials ☆*, in *Encyclopedia of Materials: Metals and Alloys*, F.G. Caballero, Editor. 2016, Elsevier: Oxford. p. 377-382.
- 20. S. Zarabi Golkhatmi, M.I. Asghar, and P.D. Lund, *A Review on Solid Oxide Fuel Cell Durability: Latest Progress, Mechanisms, and Study Tools*. Renewable and Sustainable Energy Reviews, 2022. **161**: p. 112339 DOI: https://doi.org/10.1016/j.rser.2022.112339.
- 21. R. Wang, M. Würth, U.B. Pal, S. Gopalan, and S.N. Basu, *Roles of Humidity and Cathodic Current in Chromium Poisoning of Sr-Doped LaMnO3-Based Cathodes in Solid Oxide Fuel Cells*. Journal of Power Sources, 2017. **360**: p. 87-97 DOI: <a href="https://doi.org/10.1016/j.jpowsour.2017.06.005">https://doi.org/10.1016/j.jpowsour.2017.06.005</a>.
- 22. K. Kendall and M. Kendall, *High-Temperature Solid Oxide Fuel Cells for the 21st Century:* Fundamentals, Design and Applications. 2015: Elsevier.
- 23. F. Wang, H. Kishimoto, T. Ishiyama, K. Develos-Bagarinao, K. Yamaji, T. Horita, and H. Yokokawa, *A Review of Sulfur Poisoning of Solid Oxide Fuel Cell Cathode Materials for Solid Oxide Fuel Cells*. Journal of Power Sources, 2020. **478**: p. 228763 DOI: https://doi.org/10.1016/j.jpowsour.2020.228763.

- 24. F. Wang, H. Kishimoto, K. Develos-Bagarinao, K. Yamaji, T. Horita, and H. Yokokawa, *Interrelation between Sulfur Poisoning and Performance Degradation of LSCF Cathode for SOFCs*. Journal of The Electrochemical Society, 2016. **163**(8): p. F899 DOI: <a href="https://doi.org/10.1149/2.1151608jes">https://doi.org/10.1149/2.1151608jes</a>.
- 25. C.C. Wang, S. He, K. Chen, M.R. Rowles, S. Darvish, Y. Zhong, and S.P. Jiang, *Effect of SO2 Poisoning on the Electrochemical Activity of La0.6Sr0.4Co0.2Fe0.8O3-δ Cathodes of Solid Oxide Fuel Cells*. Journal of The Electrochemical Society, 2017. **164**(6): p. F514 DOI: https://doi.org/10.1149/2.0421706jes.
- 26. B. Koo, K. Kim, J.K. Kim, H. Kwon, J.W. Han, and W. Jung, *Sr Segregation in Perovskite Oxides: Why It Happens and How It Exists.* Joule, 2018. **2**(8): p. 1476-1499 DOI: https://doi.org/10.1016/j.joule.2018.07.016.
- 27. Y. Zhang, Y. Wen, K. Huang, and J.D. Nicholas, *Atomic Layer Deposited Zirconia Overcoats as On-Board Strontium Getters for Improved Solid Oxide Fuel Cell Nanocomposite Cathode Durability*. ACS Applied Energy Materials, 2020. **3**(4): p. 4057-4067 DOI: <a href="https://doi.org/10.1021/acsaem.0c00558">https://doi.org/10.1021/acsaem.0c00558</a>.
- 28. K. Park, S. Yu, J. Bae, H. Kim, and Y. Ko, Fast Performance Degradation of SOFC Caused by Cathode Delamination in Long-Term Testing. International Journal of Hydrogen Energy, 2010. **35**(16): p. 8670-8677 DOI: <a href="https://doi.org/10.1016/j.ijhydene.2010.05.005">https://doi.org/10.1016/j.ijhydene.2010.05.005</a>.
- 29. S.P. Jiang and X. Chen, *Chromium Deposition and Poisoning of Cathodes of Solid Oxide Fuel Cells A Review*. International Journal of Hydrogen Energy, 2014. **39**(1): p. 505-531 DOI: https://doi.org/10.1016/j.ijhydene.2013.10.042.
- 30. S.C. Paulson and V.I. Birss, *Chromium Poisoning of LSM-YSZ SOFC Cathodes: I. Detailed Study of the Distribution of Chromium Species at a Porous, Single-Phase Cathode.* Journal of The Electrochemical Society, 2004. **151**(11): p. A1961 DOI: <a href="https://doi.org/10.1149/1.1806392">https://doi.org/10.1149/1.1806392</a>.
- 31. L. Zhou, J.H. Mason, W. Li, and X. Liu, Comprehensive Review of Chromium Deposition and Poisoning of Solid Oxide Fuel Cells (SOFCs) Cathode Materials. Renewable and Sustainable Energy Reviews, 2020. **134**: p. 110320 DOI: <a href="https://doi.org/10.1016/j.rser.2020.110320">https://doi.org/10.1016/j.rser.2020.110320</a>.
- 32. B. Butz, P. Kruse, H. Störmer, D. Gerthsen, A. Müller, A. Weber, and E. Ivers-Tiffée, *Correlation between Microstructure and Degradation in Conductivity for Cubic Y2O3-Doped ZrO2*. Solid State Ionics, 2006. **177**(37): p. 3275-3284 DOI: <a href="https://doi.org/10.1016/j.ssi.2006.09.003">https://doi.org/10.1016/j.ssi.2006.09.003</a>.
- 33. M. Hattori, Y. Takeda, Y. Sakaki, A. Nakanishi, S. Ohara, K. Mukai, J.-H. Lee, and T. Fukui, *Effect of Aging on Conductivity of Yttria Stabilized Zirconia*. Journal of Power Sources, 2004. **126**(1): p. 23-27 DOI: <a href="https://doi.org/10.1016/j.jpowsour.2003.08.018">https://doi.org/10.1016/j.jpowsour.2003.08.018</a>.

- 34. N. Brandon, *Solid Oxide Fuel Cell Lifetime and Reliability: Critical Challenges in Fuel Cells*. 2017: Academic Press.
- 35. I. Jang, S. Kim, C. Kim, H. Lee, H. Yoon, T. Song, and U. Paik, *Interface Engineering of Yttrium Stabilized Zirconia/Gadolinium Doped Ceria Bi-Layer Electrolyte Solid Oxide Fuel Cell for Boosting Electrochemical Performance*. Journal of Power Sources, 2019. **435**: p. 226776 DOI: <a href="https://doi.org/10.1016/j.jpowsour.2019.226776">https://doi.org/10.1016/j.jpowsour.2019.226776</a>.
- 36. J.W. Fergus, *Electrolytes for Solid Oxide Fuel Cells*. Journal of Power Sources, 2006. **162**(1): p. 30-40 DOI: https://doi.org/10.1016/j.jpowsour.2006.06.062.
- 37. A. Selçuk, G. Merere, and A. Atkinson, *The Influence of Electrodes on the Strength of Planar Zirconia Solid Oxide Fuel Cells*. Journal of Materials Science, 2001. **36**(5): p. 1173-1182 DOI: https://doi.org/10.1023/A:1004833909780.
- 38. T. Parhizkar and R. Roshandel, *Long Term Performance Degradation Analysis and Optimization of Anode Supported Solid Oxide Fuel Cell Stacks*. Energy Conversion and Management, 2017. **133**: p. 20-30 DOI: <a href="https://doi.org/10.1016/j.enconman.2016.11.045">https://doi.org/10.1016/j.enconman.2016.11.045</a>.
- 39. B. Shri Prakash, S. Senthil Kumar, and S.T. Aruna, *Properties and Development of Ni/YSZ as an Anode Material in Solid Oxide Fuel Cell: A Review.* Renewable and Sustainable Energy Reviews, 2014. **36**: p. 149-179 DOI: <a href="https://doi.org/10.1016/j.rser.2014.04.043">https://doi.org/10.1016/j.rser.2014.04.043</a>.
- 40. F. Wang, Y. Lyu, D. Chu, Z. Jin, G. Zhang, and D. Wang, *The Electrolyte Materials for SOFCs of Low-Intermediate Temperature: Review.* Materials Science and Technology, 2019. **35**(13): p. 1551-1562 DOI: https://doi.org/10.1080/02670836.2019.1639008.
- 41. Y. Xiang, Y. Da, N. Shikazono, and Z. Jiao, *Quantitative Study on Solid Oxide Fuel Cell Anode Microstructure Stability Based on 3D Microstructure Reconstructions.* Journal of Power Sources, 2020. **477**: p. 228653 DOI: <a href="https://doi.org/10.1016/j.jpowsour.2020.228653">https://doi.org/10.1016/j.jpowsour.2020.228653</a>.
- 42. M.Z. Khan, M.T. Mehran, R.-H. Song, J.-W. Lee, S.-B. Lee, and T.-H. Lim, *A Simplified Approach to Predict Performance Degradation of a Solid Oxide Fuel Cell Anode*. Journal of Power Sources, 2018. **391**: p. 94-105 DOI: <a href="https://doi.org/10.1016/j.jpowsour.2018.04.080">https://doi.org/10.1016/j.jpowsour.2018.04.080</a>.
- 43. V. Subotić, C. Schluckner, H. Schroettner, and C. Hochenauer, *Analysis of Possibilities for Carbon Removal from Porous Anode of Solid Oxide Fuel Cells after Different Failure Modes.* Journal of Power Sources, 2016. **302**: p. 378-386 DOI: <a href="https://doi.org/10.1016/j.jpowsour.2015.10.071">https://doi.org/10.1016/j.jpowsour.2015.10.071</a>.
- 44. H. Timmermann, W. Sawady, D. Campbell, A. Weber, R. Reimert, and E. Ivers-Tiffée, *Coke Formation and Degradation in SOFC Operation with a Model Reformate from Liquid Hydrocarbons*. Journal of The Electrochemical Society, 2008. **155**(4): p. B356 DOI: <a href="https://doi.org/10.1149/1.2838909">https://doi.org/10.1149/1.2838909</a>.

- 45. T.M. Gür, *Critical Review of Carbon Conversion in "Carbon Fuel Cells"*. Chemical Reviews, 2013. **113**(8): p. 6179-6206 DOI: <a href="https://doi.org/10.1021/cr400072b">https://doi.org/10.1021/cr400072b</a>.
- 46. T. Kim, G. Liu, M. Boaro, S.I. Lee, J.M. Vohs, R.J. Gorte, O.H. Al-Madhi, and B.O. Dabbousi, *A Study of Carbon Formation and Prevention in Hydrocarbon-Fueled SOFC*. Journal of Power Sources, 2006. **155**(2): p. 231-238 DOI: <a href="https://doi.org/10.1016/j.jpowsour.2005.05.001">https://doi.org/10.1016/j.jpowsour.2005.05.001</a>.
- 47. H. Kan and H. Lee, *Sn-Doped Ni/YSZ Anode Catalysts with Enhanced Carbon Deposition Resistance for an Intermediate Temperature SOFC*. Applied Catalysis B: Environmental, 2010. **97**(1): p. 108-114 DOI: https://doi.org/10.1016/j.apcatb.2010.03.029.
- 48. W. Liu, X. Sun, L.R. Pederson, O.A. Marina, and M.A. Khaleel, *Effect of Nickel–Phosphorus Interactions on Structural Integrity of Anode-Supported Solid Oxide Fuel Cells*. Journal of Power Sources, 2010. **195**(21): p. 7140-7145 DOI: <a href="https://doi.org/10.1016/j.jpowsour.2010.06.015">https://doi.org/10.1016/j.jpowsour.2010.06.015</a>.
- 49. C.A. Coyle, O.A. Marina, E.C. Thomsen, D.J. Edwards, C.D. Cramer, G.W. Coffey, and L.R. Pederson, *Interactions of Nickel/Zirconia Solid Oxide Fuel Cell Anodes with Coal Gas Containing Arsenic*. Journal of Power Sources, 2009. **193**(2): p. 730-738 DOI: <a href="https://doi.org/10.1016/j.jpowsour.2009.04.042">https://doi.org/10.1016/j.jpowsour.2009.04.042</a>.
- 50. O.A. Marina, L.R. Pederson, C.A. Coyle, E.C. Thomsen, and D.J. Edwards, *Polarization-Induced Interfacial Reactions Between Nickel and Selenium in Ni/Zirconia SOFC Anodes and Comparison with Sulfur Poisoning*. Journal of The Electrochemical Society, 2011. **158**(1): p. B36 DOI: <a href="https://doi.org/10.1149/1.3505936">https://doi.org/10.1149/1.3505936</a>.
- 51. K. Sasaki, K. Haga, T. Yoshizumi, D. Minematsu, E. Yuki, R. Liu, C. Uryu, T. Oshima, T. Ogura, Y. Shiratori, K. Ito, M. Koyama, and K. Yokomoto, *Chemical Durability of Solid Oxide Fuel Cells: Influence of Impurities on Long-Term Performance*. Journal of Power Sources, 2011. **196**(22): p. 9130-9140 DOI: <a href="https://doi.org/10.1016/j.jpowsour.2010.09.122">https://doi.org/10.1016/j.jpowsour.2010.09.122</a>.
- 52. E.M. Ryan, W. Xu, X. Sun, and M.A. Khaleel, A Damage Model for Degradation in the Electrodes of Solid Oxide Fuel Cells: Modeling the Effects of Sulfur and Antimony in the Anode. Journal of Power Sources, 2012. 210: p. 233-242 DOI: <a href="https://doi.org/10.1016/j.jpowsour.2012.02.091">https://doi.org/10.1016/j.jpowsour.2012.02.091</a>.
- 53. J.P. Trembly, A.I. Marquez, T.R. Ohrn, and D.J. Bayless, *Effects of Coal Syngas and H2S on the Performance of Solid Oxide Fuel Cells: Single-Cell Tests*. Journal of Power Sources, 2006. **158**(1): p. 263-273 DOI: <a href="https://doi.org/10.1016/j.jpowsour.2005.09.055">https://doi.org/10.1016/j.jpowsour.2005.09.055</a>.
- 54. X. Lu, T.M.M. Heenan, J.J. Bailey, T. Li, K. Li, D.J.L. Brett, and P.R. Shearing, *Correlation between Triple Phase Boundary and the Microstructure of Solid Oxide Fuel Cell Anodes: The Role of Composition, Porosity and Ni Densification.* Journal of Power Sources, 2017. **365**: p. 210-219 DOI: https://doi.org/10.1016/j.jpowsour.2017.08.095.

- 55. J. Karczewski, K.J. Dunst, P. Jasinski, and S. Molin, *High Temperature Corrosion and Corrosion Protection of Porous Ni22Cr Alloys*. Surface and Coatings Technology, 2015. **261**: p. 385-390 DOI: https://doi.org/10.1016/j.surfcoat.2014.10.051.
- 56. M. Halinen and J. Pennanen, *Analysis of Leakages in a Solid Oxide Fuel Cell Stack in a System Environment*. Fuel Cells, 2015. **15**(2): p. 434-444 DOI: <a href="https://doi.org/10.1002/fuce.201400072">https://doi.org/10.1002/fuce.201400072</a>.
- 57. J.W. Fergus, *Sealants for Solid Oxide Fuel Cells*. Journal of Power Sources, 2005. **147**(1): p. 46-57 DOI: <a href="https://doi.org/10.1016/j.jpowsour.2005.05.002">https://doi.org/10.1016/j.jpowsour.2005.05.002</a>.
- 58. M. Bram, S. Reckers, P. Drinovac, J. Mönch, R.W. Steinbrech, H.P. Buchkremer, and D. Stöver, *Characterisation and Evaluation of Compression Loaded Sealing Concepts for SOFC Stacks*. ECS Proceedings Volumes, 2003. **2003-07**(1): p. 888 DOI: <a href="https://doi.org/10.1149/200307.0888PV">https://doi.org/10.1149/200307.0888PV</a>.
- 59. M. Bram, S.E. Brünings, F. Meschke, W.A. Meulenberg, H.P. Buchkremer, R.W. Steinbrech, and D. Stöver, *Application of Metallic Gaskets in SOFC Stacks*. ECS Proceedings Volumes, 2001. **2001-16**(1): p. 875 DOI: <a href="https://doi.org/10.1149/200116.0875PV">https://doi.org/10.1149/200116.0875PV</a>.
- 60. R. Barfod, S. Koch, Y.L. Liu, P.H. Larsen, and P.V. Hendriksen, *Long-Term Tests of DK-SOFC Cells*. ECS Proceedings Volumes, 2003. **2003-07**(1): p. 1158 DOI: https://doi.org/10.1149/200307.1158PV.
- 61. K.A. Nielsen, M. Solvang, F.W. Poulsen, and P.H. Larsen, Evaluation of Sodium Aluminosilicate Glass Composite Seal with Magnesia Filler, in 28th International Conference on Advanced Ceramics and Composites A: Ceramic Engineering and Science Proceedings. 2004. p. 309-314.
- 62. K.L. Ley, M. Krumpelt, R. Kumar, J.H. Meiser, and I. Bloom, *Glass-Ceramic Sealants for Solid Oxide Fuel Cells: Part I. Physical Properties*. Journal of Materials Research, 1996. **11**(6): p. 1489-1493 DOI: <a href="https://doi.org/10.1557/JMR.1996.0185">https://doi.org/10.1557/JMR.1996.0185</a>.
- 63. S.P. Jiang, L. Christiansen, B. Hughan, and K. Foger, *Effect of Glass Sealant Materials on Microstructure and Performance of Sr-Doped LaMnO3 Cathodes*. Journal of Materials Science Letters, 2001. **20**(8): p. 695-697 DOI: https://doi.org/10.1023/A:1010950722533.
- 64. N. Lahl, L. Singheiser, K. Hilpert, K. Singh, and D. Bahadur, *Aluminosilicate Glass Ceramics as Sealant in SOFC Stacks*. ECS Proceedings Volumes, 1999. **1999-19**(1): p. 1057 DOI: https://doi.org/10.1149/199919.1057PV.
- 65. Q. Zhou, T.R. Bieler, and J.D. Nicholas, *Transient Porous Nickel Interlayers for Improved Silver-Based Solid Oxide Fuel Cell Brazes*. Acta Materialia, 2018. **148**: p. 156-162 DOI: <a href="https://doi.org/10.1016/j.actamat.2018.01.061">https://doi.org/10.1016/j.actamat.2018.01.061</a>.

- 66. A. Pönicke, J. Schilm, M. Kusnezoff, and A. Michaelis, *Aging Behavior of Reactive Air Brazed Seals for SOFC*. Fuel Cells, 2015. **15**(5): p. 735-741 DOI: https://doi.org/10.1002/fuce.201400192.
- 67. K. Scott Weil, C.A. Coyle, J.T. Darsell, G.G. Xia, and J.S. Hardy, *Effects of Thermal Cycling and Thermal Aging on the Hermeticity and Strength of Silver–Copper Oxide Air-Brazed Seals*. Journal of Power Sources, 2005. **152**: p. 97-104 DOI: <a href="https://doi.org/10.1016/j.jpowsour.2005.01.053">https://doi.org/10.1016/j.jpowsour.2005.01.053</a>.
- 68. J.Y. Kim, J.S. Hardy, and S. Weil, *Dual-Atmosphere Tolerance of Ag–CuO-Based Air Braze*. International Journal of Hydrogen Energy, 2007. **32**(16): p. 3655-3663 DOI: https://doi.org/10.1016/j.ijhydene.2006.08.054.
- 69. T. Bause, J. Malzbender, M. Pausch, T. Beck, and L. Singheiser, *Damage and Failure of Silver Based Ceramic/Metal Joints for SOFC Stacks*. Fuel Cells, 2013. **13**(4): p. 578-583 DOI: <a href="https://doi.org/10.1002/fuce.201200181">https://doi.org/10.1002/fuce.201200181</a>.
- 70. M. Rautanen, O. Thomann, O. Himanen, J. Tallgren, and J. Kiviaho, *Glass Coated Compressible Solid Oxide Fuel Cell Seals*. Journal of Power Sources, 2014. **247**: p. 243-248 DOI: <a href="https://doi.org/10.1016/j.jpowsour.2013.08.085">https://doi.org/10.1016/j.jpowsour.2013.08.085</a>.
- 71. M. Rautanen, O. Himanen, V. Saarinen, and J. Kiviaho, *Compression Properties and Leakage Tests of Mica-Based Seals for SOFC Stacks*. Fuel Cells, 2009. **9**(5): p. 753-759 DOI: <a href="https://doi.org/10.1002/fuce.200900029">https://doi.org/10.1002/fuce.200900029</a>.
- 72. K.S. Weil, J.Y. Kim, and J.S. Hardy, *Reactive Air Brazing: A Novel Method of Sealing SOFCs and Other Solid-State Electrochemical Devices*. Electrochemical and solid-state letters, 2005. **8**(2): p. A133 DOI: https://doi.org/10.1149/1.1850391.
- 73. M. Way, J. Willingham, and R. Goodall, *Brazing Filler Metals*. International Materials Reviews, 2020. **65**(5): p. 257-285 DOI: https://doi.org/10.1080/09506608.2019.1613311.
- 74. J.Y. Kim, J.S. Hardy, and K.S. Weil, *Silver-Copper Oxide Based Reactive Air Braze for Joining Yttria-Stabilized Zirconia*. Journal of Materials Research, 2005. **20**(3): p. 636-643 DOI: https://doi.org/10.1557/Jmr.2005.0088.
- 75. J.Y. Kim, J.S. Hardy, and K.S. Weil, *Novel Metal-Ceramic Joining for Planar SOFCs*. Journal of the Electrochemical Society, 2005. **152**(6): p. J52-J58 DOI: <a href="https://doi.org/10.1149/1.1896530">https://doi.org/10.1149/1.1896530</a>.
- 76. J.Y. Kim, J.S. Hardy, and K.S. Weil, *Effects of CuO Content on the Wetting Behavior and Mechanical Properties of a Ag-CuO Braze for Ceramic Joining*. Journal of the American Ceramic Society, 2005. **88**(9): p. 2521-2527 DOI: <a href="https://doi.org/10.1111/j.1551-2916.2005.00492.x">https://doi.org/10.1111/j.1551-2916.2005.00492.x</a>.
- 77. Z.B. Shao, K.R. Liu, L.Q. Liu, H.K. Liu, and S.-x. Dou, *Equilibrium Phase Diagrams in the Systems PbO–Ag and CuO–Ag*. Journal of the American Ceramic Society, 1993. **76**(10): p. 2663-2664 DOI: <a href="https://doi.org/10.1111/j.1151-2916.1993.tb03996.x">https://doi.org/10.1111/j.1151-2916.1993.tb03996.x</a>.

- 78. T. Phongpreecha, J.D. Nicholas, T.R. Bieler, and Y. Qi, Computational Design of Metal Oxides to Enhance the Wetting and Adhesion of Silver-Based Brazes on Yttria-Stabilized-Zirconia. Acta Materialia, 2018. **152**: p. 229-238 DOI: https://doi.org/10.1016/j.actamat.2018.04.024.
- 79. C.J. Smithells, W.F. Gale, and T.C. Totemeier, *Smithells Metals Reference Book*. 8th ed. 2004: Elsevier.
- 80. R.L. Klueh and W.W. Mullins, *Some Observations on Hydrogen Embrittlement of Silver*. TRANSACTIONS OF THE METALLURGICAL SOCIETY OF AIME, 1968. **242**(2): p. 237-44.
- P. Singh, Z. Yang, V. Viswanathan, and J.W. Stevenson, *Observations on the Structural Degradation of Silver during Simultaneous Exposure to Oxidizing and Reducing Environments*. Journal of Materials Engineering and Performance, 2004. **13**(3): p. 287-294 DOI: <a href="https://doi.org/10.1361/10599490419261">https://doi.org/10.1361/10599490419261</a>.
- 82. K.S. Weil, J.Y. Kim, J.S. Hardy, and J.T. Darsell, *The Effect of TiO2 on the Wetting Behavior of Silver–Copper Oxide Braze Filler Metals*. Scripta Materialia, 2006. **54**(6): p. 1071-1075 DOI: https://doi.org/10.1016/j.scriptamat.2005.12.003.
- 83. K.S. Weil, J.Y. Kim, J.S. Hardy, and J.T. Darsell. *Improved Wetting Characteristics in TiO2–Modified Ag-CuO Air Braze Filler Metals*. 2006. ASM International.
- 84. W. Zhao, S. Zhang, J. Yang, T. Lin, D.P. Sekulic, and P. He, *Wetting and Brazing of YIG Ceramics Using Ag–CuO–TiO2 Metal Filler*. Journal of Materials Research and Technology, 2021. **10**: p. 1158-1168 DOI: <a href="https://doi.org/10.1016/j.jmrt.2020.12.080">https://doi.org/10.1016/j.jmrt.2020.12.080</a>.
- W. Kobsiriphat and S. Barnett, *Ag–Cu–Ti Braze Materials for Sealing SOFCs*. Journal of Fuel Cell Science and Technology, 2008. **5**(1) DOI: <a href="https://doi.org/10.1115/1.2784279">https://doi.org/10.1115/1.2784279</a>.
- M. Singh, T.P. Shpargel, and R. Asthana, *Brazing of Stainless Steel to Yttria-Stabilized Zirconia Using Gold-Based Brazes for Solid Oxide Fuel Cell Applications*. International Journal of Applied Ceramic Technology, 2007. **4**(2): p. 119-133 DOI: <a href="https://doi.org/10.1111/j.1744-7402.2007.02126.x">https://doi.org/10.1111/j.1744-7402.2007.02126.x</a>.
- 87. K.-L. Lin, M. Singh, R. Asthana, and C.-H. Lin, *Interfacial and Mechanical Characterization of Yttria-Stabilized Zirconia (YSZ) to Stainless Steel Joints Fabricated Using Ag–Cu–Ti Interlayers*. Ceramics International, 2014. **40**(1, Part B): p. 2063-2071 DOI: <a href="https://doi.org/10.1016/j.ceramint.2013.07.119">https://doi.org/10.1016/j.ceramint.2013.07.119</a>.
- 88. M.L. Santella, J.A. Horton, and J.J. Pak, *Microstructure of Alumina Brazed with a Silver-Copper-Titanium Alloy*. Journal of the American Ceramic Society, 1990. **73**(6): p. 1785-1787 DOI: https://doi.org/10.1111/j.1151-2916.1990.tb09835.x.
- 89. X. Si, J. Cao, X. Song, Y. Qu, and J. Feng, Reactive Air Brazing of YSZ Ceramic with Novel Al2O3 Nanoparticles Reinforced Ag-CuO-Al2O3 Composite Filler: Microstructure and

- *Joint Properties.* Materials & Design, 2017. **114**: p. 176-184 DOI: <a href="https://doi.org/10.1016/j.matdes.2016.10.062">https://doi.org/10.1016/j.matdes.2016.10.062</a>.
- 90. X. Si, J. Cao, X. Song, Z. Wang, Z. Wang, and J. Feng, Evolution Behavior of Al2O3 Nanoparticles Reinforcements during Reactive Air Brazing and Its Role in Improving the Joint Strength. Materials & Design, 2017. 132: p. 96-104 DOI: <a href="https://doi.org/10.1016/j.matdes.2017.07.002">https://doi.org/10.1016/j.matdes.2017.07.002</a>.
- 91. Y. Luo, X.G. Song, S.P. Hu, Z.Q. Xu, Z.H. Li, and Y. Lei, *Reactive Air Brazing of Al2O3 Ceramic with Ag-CuO-Pt Composite Fillers: Microstructure and Joint Properties.* Journal of the European Ceramic Society, 2021. **41**(2): p. 1407-1414 DOI: <a href="https://doi.org/10.1016/j.jeurceramsoc.2020.10.008">https://doi.org/10.1016/j.jeurceramsoc.2020.10.008</a>.
- 92. X.J. Liu, F. Gao, C.P. Wang, and K. Ishida, *Thermodynamic Assessments of the Ag-Ni Binary and Ag-Cu-Ni Ternary Systems*. Journal of Electronic Materials, 2008. **37**(2): p. 210-217 DOI: <a href="https://doi.org/10.1007/s11664-007-0315-1">https://doi.org/10.1007/s11664-007-0315-1</a>.
- 93. G. Hu, Q. Zhou, A. Bhatlawande, J. Park, R. Termuhlen, Y. Ma, T.R. Bieler, H.-C. Yu, Y. Qi, T. Hogan, and J.D. Nicholas, *Patterned Nickel Interlayers for Enhanced Silver Wetting, Spreading and Adhesion on Ceramic Substrates*. Scripta Materialia, 2021. **196**: p. 113767 DOI: https://doi.org/10.1016/j.scriptamat.2021.113767.
- 94. J. Park, T. Phongpreecha, J.D. Nicholas, and Y. Qi, *Enhanced Liquid Metal Wetting on Oxide Surfaces via Patterned Particles*. Acta Materialia, 2020. **199**: p. 551-560 DOI: https://doi.org/10.1016/j.actamat.2020.08.037.
- 95. R. Termuhlen, G. Hu, J.D. Nicholas, and H.-C. Yu, *Spontaneous Imbibition Velocities in Porous Metal Layers on Ceramic Substrates Calculated Using Microstructural Analyses*. Materialia, 2023. **28**: p. 101779 DOI: <a href="https://doi.org/10.1016/j.mtla.2023.101779">https://doi.org/10.1016/j.mtla.2023.101779</a>.
- 96. R. Termuhlen, K. Fitzmaurice, and H.-C. Yu, *Smoothed Boundary Method for Simulating Incompressible Flow in Complex Geometries*. Computer Methods in Applied Mechanics and Engineering, 2022. **399**: p. 115312 DOI: <a href="https://doi.org/10.1016/j.cma.2022.115312">https://doi.org/10.1016/j.cma.2022.115312</a>.
- 97. T. Wang, X. Chen, G.Q. Lu, and G.Y. Lei, *Low-Temperature Sintering with Nano-Silver Paste in Die-Attached Interconnection*. Journal of Electronic Materials, 2007. **36**(10): p. 1333-1340 DOI: https://doi.org/10.1007/s11664-007-0230-5.
- 98. K. Suganuma, S. Sakamoto, N. Kagami, D. Wakuda, K.S. Kim, and M. Nogi, *Low-Temperature Low-Pressure Die Attach with Hybrid Silver Particle Paste*. Microelectronics Reliability, 2012. **52**(2): p. 375-380 DOI: <a href="https://doi.org/10.1016/j.microrel.2011.07.088">https://doi.org/10.1016/j.microrel.2011.07.088</a>.
- 99. I.E. Stewart, M.J. Kim, and B.J. Wiley, *Effect of Morphology on the Electrical Resistivity of Silver Nanostructure Films*. ACS Applied Materials & Interfaces, 2017. **9**(2): p. 1870-1876 DOI: <a href="https://doi.org/10.1021/acsami.6b12289">https://doi.org/10.1021/acsami.6b12289</a>.
- 100. B.Y. Ahn, E.B. Duoss, M.J. Motala, X. Guo, S.I. Park, Y. Xiong, J. Yoon, R.G. Nuzzo, J.A. Rogers, and J.A. Lewis, *Omnidirectional Printing of Flexible, Stretchable, and*

- *Spanning Silver Microelectrodes.* Science, 2009. **323**(5921): p. 1590-1593 DOI: <a href="https://doi.org/10.1126/science.1168375">https://doi.org/10.1126/science.1168375</a>.
- 101. M. Knoerr and A. Schletz. Power Semiconductor Joining through Sintering of Silver Nanoparticles: Evaluation of Influence of Parameters Time, Temperature and Pressure on Density, Strength and Reliability. in 2010 6th International Conference on Integrated Power Electronics Systems, CIPS 2010. 2011.
- 102. H. Ogura, M. Maruyama, R. Matsubayashi, T. Ogawa, S. Nakamura, T. Komatsu, H. Nagasawa, A. Ichimura, and S. Isoda, *Carboxylate-Passivated Silver Nanoparticles and Their Application to Sintered Interconnection: A Replacement for High Temperature Lead-Rich Solders*. Journal of Electronic Materials, 2010. **39**(8): p. 1233-1240 DOI: https://doi.org/10.1007/s11664-010-1236-y.
- 103. R. Khazaka, L. Mendizabal, and D. Henry, *Review on Joint Shear Strength of Nano-Silver Pasteand Its Long-Term High Temperature Reliability*. Journal of Electronic Materials, 2014. **43**(7): p. 2459-2466 DOI: <a href="https://doi.org/10.1007/s11664-014-3202-6">https://doi.org/10.1007/s11664-014-3202-6</a>.
- 104. J. Liu and S.A. Barnett, *Operation of Anode-Supported Solid Oxide Fuel Cells on Methane and Natural Gas.* Solid State Ionics, 2003. **158**(1): p. 11-16 DOI: https://doi.org/10.1016/S0167-2738(02)00769-5.
- 105. C. Xia and M. Liu, *Low-Temperature SOFCs Based on Gd0.1Ce0.9O1.95 Fabricated by Dry Pressing.* Solid State Ionics, 2001. **144**(3): p. 249-255 DOI: <a href="https://doi.org/10.1016/S0167-2738(01)00980-8">https://doi.org/10.1016/S0167-2738(01)00980-8</a>.
- 106. X. Xu, C. Xia, S. Huang, and D. Peng, YSZ Thin Films Deposited by Spin-Coating for IT-SOFCs. Ceramics International, 2005. **31**(8): p. 1061-1064 DOI: <a href="https://doi.org/10.1016/j.ceramint.2004.11.005">https://doi.org/10.1016/j.ceramint.2004.11.005</a>.
- 107. Z. Lü, L. Pei, T.-m. He, X.-q. Huang, Z.-g. Liu, Y. Ji, X.-h. Zhao, and W.-h. Su, *Study on New Copper-Containing SOFC Anode Materials*. Journal of Alloys and Compounds, 2002. 334(1): p. 299-303 DOI: <a href="https://doi.org/10.1016/S0925-8388(01)01795-9">https://doi.org/10.1016/S0925-8388(01)01795-9</a>.
- 108. N. Li, Z. Lü, B. Wei, X. Huang, K. Chen, Y. Zhang, and W. Su, *Characterization of GdBaCo2O5+δ Cathode for IT-SOFCs*. Journal of Alloys and Compounds, 2008. **454**(1): p. 274-279 DOI: https://doi.org/10.1016/j.jallcom.2006.12.017.
- 109. Y. Xie, J. Xiao, D. Liu, J. Liu, and C. Yang, *Electrolysis of Carbon Dioxide in a Solid Oxide Electrolyzer with Silver-Gadolinium-Doped Ceria Cathode*. Journal of The Electrochemical Society, 2015. **162**(4): p. F397-F402 DOI: <a href="https://doi.org/10.1149/2.0501504jes">https://doi.org/10.1149/2.0501504jes</a>.
- 110. Z.Z. Zhang and G.Q. Lu, *Pressure-Assisted Low-Temperature Sintering of Silver Paste as an Alternative Die-Attach Solution to Solder Reflow.* IEEE Transactions on Electronics Packaging Manufacturing, 2002. **25**(4): p. 279-283 DOI: <a href="https://doi.org/10.1109/TEPM.2002.807719">https://doi.org/10.1109/TEPM.2002.807719</a>.

- 111. T.G. Lei, J.N. Calata, G.Q. Lu, X. Chen, and S. Luo, *Low-Temperature Sintering of Nanoscale Silver Paste for Attaching Large-Area* (>100mm2) *Chips.* IEEE Transactions on Components and Packaging Technologies, 2010. **33**(1): p. 98-104 DOI: https://doi.org/10.1109/TCAPT.2009.2021256.
- 112. A. Hirose, H. Tatsumi, N. Takeda, Y. Akada, T. Ogura, E. Ide, and T. Morita, *A Novel Metal-to-Metal Bonding Process through In-Situ Formation of Ag Nanoparticles Using Ag2O Microparticles*. Journal of Physics: Conference Series, 2009. **165**: p. 012074 DOI: https://doi.org/10.1088/1742-6596/165/1/012074.
- 113. K. Asama, T. Matsuda, T. Ogura, T. Sano, M. Takahashi, and A. Hirose, *Low-Temperature Metal-to-Alumina Direct Bonding Process Utilizing Redox Reaction between Silver Oxide and Organic Agent*. Materials Science and Engineering: A, 2017. **702**: p. 398-405 DOI: <a href="https://doi.org/10.1016/j.msea.2017.07.034">https://doi.org/10.1016/j.msea.2017.07.034</a>.
- 114. S.B. Walker and J.A. Lewis, *Reactive Silver Inks for Patterning High-Conductivity Features at Mild Temperatures*. Journal of the American Chemical Society, 2012. **134**(3): p. 1419-1421 DOI: https://doi.org/10.1021/ja209267c.
- T. Kunimune, M. Kuramoto, S. Ogawa, T. Sugahara, S. Nagao, and K. Suganuma, *Ultra Thermal Stability of LED Die-Attach Achieved by Pressureless Ag Stress-Migration Bonding at Low Temperature*. Acta Materialia, 2015. **89**: p. 133-140 DOI: <a href="https://doi.org/10.1016/j.actamat.2015.02.011">https://doi.org/10.1016/j.actamat.2015.02.011</a>.
- T. Kunimune, M. Kuramoto, S. Ogawa, M. Nogi, and K. Suganuma, *Low-Temperature Pressure-less Silver Direct Bonding*. IEEE Transactions on Components, Packaging and Manufacturing Technology, 2013. **3**(3): p. 363-369 DOI: <a href="https://doi.org/10.1109/TCPMT.2012.2231901">https://doi.org/10.1109/TCPMT.2012.2231901</a>.
- 117. K.M.A. Rahman, D.N. Wells, and M.T. Duignan, *Laser Direct-Write of Materials for Microelectronics Applications*. MRS Proceedings, 2000. **624**: p. 99 DOI: <a href="https://doi.org/10.1557/PROC-624-99">https://doi.org/10.1557/PROC-624-99</a>.
- 118. X. Li, H. Li, Y. Chen, and X. Zeng, Silver Conductor Fabrication by Laser Direct Writing on Al2O3 Substrate. Applied Physics A, 2004. **79**(8): p. 1861-1864 DOI: https://doi.org/10.1007/s00339-004-2914-5.
- 119. B. Sérier, A. Berroug, D. Juvé, D. Tréheux, and E.G. Moya, *Silver-Alumina Solid State Bonding: Study of Diffusion and Toughness Close to the Interface*. Journal of the European Ceramic Society, 1993. **12**(5): p. 385-390 DOI: <a href="https://doi.org/10.1016/0955-2219(93)90008-F">https://doi.org/10.1016/0955-2219(93)90008-F</a>.
- 120. B. Serier and D. Treheux, *Silver-Alumina Solid State Bonding: Influence of the Work Hardening of the Metal.* Acta Metallurgica et Materialia, 1993. **41**(2): p. 369-374 DOI: https://doi.org/10.1016/0956-7151(93)90067-3.

- 121. C.-H. Sha, P.J. Wang, W.P. Lin, and C.C. Lee, *Solid State Bonding of Silver Foils to Metalized Alumina Substrates at 260°C*. Journal of Electronic Packaging, 2011. **133**(4) DOI: https://doi.org/10.1115/1.4005295.
- 122. D. Treheux, P. Lourdin, B. Mbongo, and D. Juve, *Metal-Ceramic Solid State Bonding: Mechanisms and Mechanics*. Scripta Metallurgica et Materialia, 1994. **31**(8): p. 1055-1060 DOI: <a href="https://doi.org/10.1016/0956-716X(94)90526-6">https://doi.org/10.1016/0956-716X(94)90526-6</a>.
- 123. B. Serier, B. Bachir Bouiadjra, M. Belhouari, and D. Treheux, *Experimental Analysis of the Strength of Silver–Alumina Junction Elaborated at Solid State Bonding*. Materials & Design, 2011. **32**(7): p. 3750-3755 DOI: https://doi.org/10.1016/j.matdes.2011.03.047.
- 124. C.C. Schu'ler, A. Stuck, N. Beck, H. Keser, and U. Ta'ck, *Direct Silver Bonding An Alternative for Substrates in Power Semiconductor Packaging*. Journal of Materials Science: Materials in Electronics, 2000. **11**(5): p. 389-396 DOI: <a href="https://doi.org/10.1023/A:1008942502309">https://doi.org/10.1023/A:1008942502309</a>.
- 125. H.-j. Xie, X.-c. Wu, and Y.-a. Min, *Influence of Chemical Composition on Phase Transformation Temperature and Thermal Expansion Coefficient of Hot Work Die Steel.*Journal of Iron and Steel Research International, 2008. **15**(6): p. 56-61 DOI: <a href="https://doi.org/10.1016/S1006-706X(08)60267-8">https://doi.org/10.1016/S1006-706X(08)60267-8</a>.
- 126. JFE Steel Corporation. *JFE20-5USR High Oxidation Resistant Stainless Steel*. [cited 2023 June 25]; Available from: https://www.jfe-steel.co.jp/en/products/stainless/jfe20\_5usr.php.
- 127. Straub Metals. *441 Stainless Steel*. [cited 2023 June 25]; Available from: <a href="https://www.straubmetal409.com/441-stainless-steel/">https://www.straubmetal409.com/441-stainless-steel/</a>.
- 128. D. Sarantaridis and A. Atkinson, *Redox Cycling of Ni-Based Solid Oxide Fuel Cell Anodes: A Review.* Fuel cells, 2007. **7**(3): p. 246-258 DOI: https://doi.org/10.1002/fuce.200600028.
- D. Waldbillig, A. Wood, and D.G. Ivey, *Electrochemical and Microstructural Characterization of the Redox Tolerance of Solid Oxide Fuel Cell Anodes*. Journal of Power Sources, 2005. **145**(2): p. 206-215 DOI: <a href="https://doi.org/10.1016/j.jpowsour.2004.12.071">https://doi.org/10.1016/j.jpowsour.2004.12.071</a>.
- 130. H. Sumi, T. Yamaguchi, K. Hamamoto, T. Suzuki, and Y. Fujishiro, *Electrochemical Analysis for Anode-Supported Microtubular Solid Oxide Fuel Cells in Partial Reducing and Oxidizing Conditions*. Solid State Ionics, 2014. **262**: p. 407-410 DOI: <a href="https://doi.org/10.1016/j.ssi.2014.01.012">https://doi.org/10.1016/j.ssi.2014.01.012</a>.
- 131. M. Hanasaki, C. Uryu, T. Daio, T. Kawabata, Y. Tachikawa, S.M. Lyth, Y. Shiratori, S. Taniguchi, and K. Sasaki, *SOFC Durability against Standby and Shutdown Cycling*. Journal of The Electrochemical Society, 2014. **161**(9): p. F850 DOI: https://doi.org/10.1149/2.0421409jes.

- 132. B. Iwanschitz, J. Sfeir, A. Mai, and M. Schütze, *Degradation of SOFC Anodes upon Redox Cycling: A Comparison Between Ni/YSZ and Ni/CGO*. Journal of The Electrochemical Society, 2010. **157**(2): p. B269 DOI: <a href="https://doi.org/10.1149/1.3271101">https://doi.org/10.1149/1.3271101</a>.
- 133. T. Klemensø, C.C. Appel, and M. Mogensen, *In Situ Observations of Microstructural Changes in SOFC Anodes during Redox Cycling*. Electrochemical and Solid-State Letters, 2006. **9**(9): p. A403 DOI: <a href="https://doi.org/10.1149/1.2214303">https://doi.org/10.1149/1.2214303</a>.
- 134. D. Sarantaridis, R.J. Chater, and A. Atkinson, *Changes in Physical and Mechanical Properties of SOFC Ni–YSZ Composites Caused by Redox Cycling*. Journal of The Electrochemical Society, 2008. **155**(5): p. B467 DOI: https://doi.org/10.1149/1.2883731.
- 135. H. Sumi, R. Kishida, J.-Y. Kim, H. Muroyama, T. Matsui, and K. Eguchi, *Correlation Between Microstructural and Electrochemical Characteristics during Redox Cycles for Ni–YSZ Anode of SOFCs.* Journal of The Electrochemical Society, 2010. **157**(12): p. B1747 DOI: <a href="https://doi.org/10.1149/1.3491345">https://doi.org/10.1149/1.3491345</a>.
- 136. M. Pihlatie, A. Kaiser, and M. Mogensen, *Redox Stability of SOFC: Thermal Analysis of Ni–YSZ Composites*. Solid State Ionics, 2009. **180**(17): p. 1100-1112 DOI: https://doi.org/10.1016/j.ssi.2009.04.011.
- T. Hatae, Y. Matsuzaki, S. Yamashita, and Y. Yamazaki, *Destruction Modes of Anode-Supported SOFC Caused by Degrees of Electrochemical Oxidation in Redox Cycle*. Journal of The Electrochemical Society, 2010. **157**(5): p. B650 DOI: <a href="https://doi.org/10.1149/1.3328453">https://doi.org/10.1149/1.3328453</a>.
- 138. Q. Ma, F. Tietz, A. Leonide, and E. Ivers-Tiffée, *Anode-Supported Planar SOFC with High Performance and Redox Stability*. Electrochemistry Communications, 2010. **12**(10): p. 1326-1328 DOI: <a href="https://doi.org/10.1016/j.elecom.2010.07.011">https://doi.org/10.1016/j.elecom.2010.07.011</a>.
- Q. Zhou, T.R. Bieler, and J.D. Nicholas, *Dual Atmosphere Isothermal Aging and Rapid Thermal Cycling of Ag-Ni and Ag-CuO Stainless Steel to Zirconia Braze Joints*. Journal of the Electrochemical Society, 2019. **166**(10): p. F594 DOI: https://doi.org/10.1149/2.0911910jes.
- 140. Y.B. Matus, L.C. De Jonghe, C.P. Jacobson, and S.J. Visco, *Metal-Supported Solid Oxide Fuel Cell Membranes for Rapid Thermal Cycling*. Solid State Ionics, 2005. **176**(5): p. 443-449 DOI: <a href="https://doi.org/10.1016/j.ssi.2004.09.056">https://doi.org/10.1016/j.ssi.2004.09.056</a>.
- 141. K.J. Kim, B.H. Park, S.J. Kim, Y. Lee, H. Bae, and G.M. Choi, *Micro Solid Oxide Fuel Cell Fabricated on Porous Stainless Steel: a New Strategy for Enhanced Thermal Cycling Ability*. Scientific Reports, 2016. **6**(1): p. 22443 DOI: <a href="https://doi.org/10.1038/srep22443">https://doi.org/10.1038/srep22443</a>.
- 142. R.J. Milcarek, M.J. Garrett, T.S. Welles, and J. Ahn, *Performance Investigation of a Micro-Tubular Flame-Assisted Fuel Cell Stack with 3,000 Rapid Thermal Cycles*. Journal of Power Sources, 2018. **394**: p. 86-93 DOI: https://doi.org/10.1016/j.jpowsour.2018.05.060.

- 143. M.C. Tucker, G.Y. Lau, C.P. Jacobson, L.C. DeJonghe, and S.J. Visco, *Stability and Robustness of Metal-Supported SOFCs*. Journal of Power Sources, 2008. **175**(1): p. 447-451 DOI: https://doi.org/10.1016/j.jpowsour.2007.09.032.
- 144. M.W. Barsoum, *Fundamentals of Ceramics*. 2003, Bristol and Philadelphia: Institute of Physics Publishing.
- 145. American Society for Testing and Materials, Standard Test Methods for Measuring Resistivity and Hall Coefficient and Determining Hall Mobility in Single-Crystal Semiconductors. ASTM Standards, 2016 DOI: <a href="http://dx.doi.org/10.1520/F0076-08R16E01">http://dx.doi.org/10.1520/F0076-08R16E01</a>.
- 146. J.H. Klootwijk and C.E. Timmering. *Merits and limitations of circular TLM structures for contact resistance determination for novel III-V HBTs.* in *Proceedings of the 2004 International Conference on Microelectronic Test Structures (IEEE Cat. No.04CH37516).* 2004. DOI: 10.1109/ICMTS.2004.1309489.
- 147. G.S. Marlow and M.B. Das, *The Effects of Contact Size and Non-Zero Metal Resistance on the Determination of Specific Contact Resistance*. Solid-State Electronics, 1982. **25**(2): p. 91-94 DOI: <a href="https://doi.org/10.1016/0038-1101(82)90036-3">https://doi.org/10.1016/0038-1101(82)90036-3</a>.
- 148. D.W. Koon, M. Heřmanová, and J. Náhlík, *Electrical Conductance Sensitivity Functions for Square and Circular Cloverleaf van der Pauw Geometries*. Measurement Science and Technology, 2015. **26**(11): p. 115004 DOI: <a href="https://doi.org/10.1088/0957-0233/26/11/115004">https://doi.org/10.1088/0957-0233/26/11/115004</a>.
- 149. D.R. Lide, *CRC Handbook of Chemistry and Physics, Internet Version*. 2005: CRC Press, Boca Raton, FL.
- 150. Rolled Metal Products. *Stainless Steel Type 441*. [cited 2023 June 25]; Available from: https://rolledmetalproducts.com/stainless-steel-type-441/.
- 151. R.A. Matula, *Electrical Resistivity of Copper, Gold, Palladium, and Silver.* Journal of Physical and Chemical Reference Data, 1979. **8**(4): p. 1147-1298 DOI: https://doi.org/10.1063/1.555614.
- 152. A. Hassini, M. Gervais, S. Roger, P. Simon, J. Lecomte, N. Raimboux, and F. Gervais, *Upshift of Ferromagnetic–Paramagnetic Phase Transition Temperature of La0.8Sr0.2Mn1–xRuxO3 Probed by Electron Spin Resonance*. Solid State Sciences, 2002. **4**(7): p. 907-910 DOI: <a href="https://doi.org/10.1016/S1293-2558(02)01354-7">https://doi.org/10.1016/S1293-2558(02)01354-7</a>.
- 153. A. Bhatlawande, G. Hu, J. Nicholas, and T. Hogan, *Temperature-Dependent Sheet and Contact Resistivity Measurements on Ag and Ag-Ni Circuit Pastes*. ECS Transactions, 2023. **111**(6): p. 2361 DOI: https://doi.org/10.1149/11106.2361ecst.
- 154. D.M. Lipkin, J.N. Israelachvili, and D.R. Clarke, *Estimating the Metal-Ceramic Van der Waals Adhesion Energy*. Philosophical Magazine A, 1997. **76**(4): p. 715-728 DOI: <a href="https://doi.org/10.1080/01418619708214205">https://doi.org/10.1080/01418619708214205</a>.

- 155. Z. Yang, Recent Advances in Metallic Interconnects for Solid Oxide Fuel Cells. International Materials Reviews, 2008. **53**(1): p. 39-54 DOI: https://doi.org/10.1179/174328007X212526.
- J.C.W. Mah, A. Muchtar, M.R. Somalu, and M.J. Ghazali, *Metallic Interconnects for Solid Oxide Fuel Cell: A Review on Protective Coating and Deposition Techniques*. International Journal of Hydrogen Energy, 2017. **42**(14): p. 9219-9229 DOI: <a href="https://doi.org/10.1016/j.ijhydene.2016.03.195">https://doi.org/10.1016/j.ijhydene.2016.03.195</a>.
- 157. J.Y. Kim, J.-P. Choi, and K. Scott Weil, *Mechanical Properties and Dual Atmosphere Tolerance of Ag–Al Based Braze*. International Journal of Hydrogen Energy, 2008. **33**(14): p. 3952-3961 DOI: https://doi.org/10.1016/j.ijhydene.2007.12.043.
- 158. J.Y. Kim, J.S. Hardy, and K.S. Weil, *Ag–Al Based Air Braze for High Temperature Electrochemical Devices*. International Journal of Hydrogen Energy, 2007. **32**(16): p. 3754-3762 DOI: <a href="https://doi.org/10.1016/j.ijhydene.2006.08.055">https://doi.org/10.1016/j.ijhydene.2006.08.055</a>.
- 159. J. Mougin, A. Galerie, M. Dupeux, N. Rosman, G. Lucazeau, A.M. Huntz, and L. Antoni, *In-Situ Determination of Growth and Thermal Stresses in Chromia Scales Formed on a Ferritic Stainless Steel.* Materials and Corrosion, 2002. **53**(7): p. 486-490 DOI: https://doi.org/10.1002/1521-4176(200207)53:7<486::AID-MACO486>3.0.CO;2-P.
- 160. I. Barin, Ag-AuTe2, in Thermochemical Data of Pure Substances. 1995. p. 1-103.
- 161. B.C.H. Steele and A. Heinzel, *Materials for Fuel-Cell Technologies*. Nature, 2001. **414**(6861): p. 345-352 DOI: https://doi.org/10.1038/35104620.
- 162. I. Karakaya and W.T. Thompson, *The Ag-Pt (Silver-Platinum) System*. Bulletin of Alloy Phase Diagrams, 1987. **8**(4): p. 334-340 DOI: https://doi.org/10.1007/BF02869269.
- 163. H. Okamoto, *Ag-Pt* (*Silver-Platinum*). Journal of Phase Equilibria, 1997. **18**(5): p. 485-485 DOI: https://doi.org/10.1007/BF02647706.
- 164. I. Karakaya and W.T. Thompson, *The Ag-Pd (Silver-Palladium) System*. Bulletin of Alloy Phase Diagrams, 1988. **9**(3): p. 237-243 DOI: <a href="https://doi.org/10.1007/BF02881271">https://doi.org/10.1007/BF02881271</a>.
- 165. M. Venkatraman and J.P. Neumann, *The Ag-Cr (Silver-Chromium) System*. Bulletin of Alloy Phase Diagrams, 1990. **11**(3): p. 263-265 DOI: <a href="https://doi.org/10.1007/BF03029296">https://doi.org/10.1007/BF03029296</a>.
- 166. H. Niu, X.-Q. Chen, P. Liu, W. Xing, X. Cheng, D. Li, and Y. Li, *Extra-Electron Induced Covalent Strengthening and Generalization of Intrinsic Ductile-to-Brittle Criterion*. Scientific Reports, 2012. **2**(1): p. 718 DOI: <a href="https://doi.org/10.1038/srep00718">https://doi.org/10.1038/srep00718</a>.
- 167. Y.-S. Chou and J.W. Stevenson, *Novel Silver/Mica Multilayer Compressive Seals for Solid-Oxide Fuel Cells: The Effect of Thermal Cycling and Material Degradation on Leak Behavior*. Journal of Materials Research, 2003. **18**(9): p. 2243-2250 DOI: <a href="https://doi.org/10.1557/JMR.2003.0313">https://doi.org/10.1557/JMR.2003.0313</a>.

- 168. Q. Zhou, Ellingham Diagram from Thermaldynamic Data. ca. 2017.
- 169. G.T. Mase, R.E. Smelser, and G.E. Mase, *Continuum Mechanics for Engineers*. 2009: CRC press.

### APPENDIX A: BRAZING TEMPERATURE PROFILES AND RATIONALE

The preparation of the Ag-Ni AFA-441 samples involved two-step heating. Firstly, the nickel-printed stainless steel pieces were heated to ~830°C at 5°C/min and held at this temperature for 2 hours. Subsequently, the samples were cooled down to room temperature at 5°C/min. Next, the silver pieces were positioned between the printed layers, and the assembled samples were subjected to another heating process. The temperature was increased to ~1025°C at a rate of 5°C/min, and held for 30 minutes. Throughout both heating processes, a flow of 20 sccm argon gas was maintained. The alumina tube in which the samples were placed contained residual organic substance originating from the organic vehicle present in the paste used in previous experiments. This carbon present in the system, as well as the carbon in the nickel paste, can hinder proper wetting. To address this issue, nickel oxide powder was placed around the samples. The nickel oxide serves to remove excess carbon from the system.

The first heating process serves two primary purposes. Firstly, it is aimed at sintering the porous nickel interlayer, which induces structural changes and generates capillary forces that promote effective wetting. This step is crucial for improving the overall bonding process. Secondly, the first heating process facilitates the oxidation of carbon present in the nickel paste. The introduction of nickel oxide within the system ensures a sufficiently high oxygen partial pressure, enabling the oxidation of carbon while preserving the integrity of the nickel metal. The utilization of the Ellingham Diagram (shown in the Figure A-1) demonstrates that above approximately 175°C, the oxygen partial pressure set by the 2Ni+O<sub>2</sub>=2NiO reaction surpasses that set by the C+O<sub>2</sub>=CO<sub>2</sub> reaction.

The second heating process primarily focuses on the melting of silver, enabling the bonding to occur. This step facilitates the formation of a strong and durable bond between the materials being joined.

Overall, the two-step heating process combines the sintering of the nickel interlayer, controlled oxidation of carbon, and silver melting to achieve successful bonding and ensure the desired material properties are obtained.

The preparation of the Ag-25wt.%Pt AFA-441 samples involved one-step heating. Pure silver foil was positioned between the Ag-Pt-printed stainless steel pieces. The assembled samples were heated to ~830°C at 5°C/min and held at this temperature for 2 hours. Subsequently, the temperature was ramped to ~1025°C at a rate of 5°C/min, and held for 30 minutes. Throughout the heating process, a flow of 20 sccm argon gas was maintained. Nickel oxide powder was placed around the samples to remove excess carbon from the system.

The heating process employed for the Ag-25wt.%Pt sample preparations differed from that used for the Ag-Ni samples. The main distinction lies in the cooling step after the sintering of the interlayer particles. In the case of Ag-25wt.%Pt samples, they were not cooled down following interlayer particle sintering. The holding at approximately 830°C during the first heating segment aims to sinter the porous interlayer and eliminate any carbon present in the paste. By proceeding directly to the subsequent heating phase after the first segment, the reaction between platinum and iron in the steel is mostly prevented. It was observed that using the same two-step heating temperature profile as the Ag-Ni samples resulted in inadequate bonding. The reason for this poor bonding is attributed to the reaction between platinum and iron, which consumes the interlayer material and consequently hampers wetting due to insufficient interlayer material availability. The ~1025°C holding serves to melt silver, enabling the bonding to occur.

The preparation of the Ag-CuO samples involved one-step heating. Pure silver foil was positioned between the Ag-Cu-printed stainless steel pieces. The assembled samples were heated to ~850°C at 5°C/min and held at this temperature for 2 hours. Subsequently, the temperature was ramped to ~990°C at a rate of 5°C/min, and held for 6 minutes. This process was carried out in a static air atmosphere, which was deliberately chosen due to the reliance of Ag-CuO brazing on the reaction between copper oxide and the substrate. When applying this brazing technique to alumina, ceramic-ceramic bonding becomes more favorable than metal-ceramic bonding. Hence, the oxidation of copper components in the filling metal becomes necessary.

During the ~850°C holding phase, the primary objectives are to partly sinter the Ag-Cu interlayer and oxidize the copper within it. Subsequently, the temperature is raised to melt the silver. In contrast to the temperature profiles used for Ag-Ni and Ag-Pt samples, the holding time for silver melting is intentionally reduced. This alteration was implemented in response to observations that the Ag-Cu pattern was unable to contain the molten silver effectively. As a result, silver tended to escape from the gaps and form inadequate brazes. This phenomenon is attributed to the relatively poor wetting of silver on copper oxide printed substrates. To address this issue and prevent undesired silver flow, a shorter holding period during silver melting was employed. This modification effectively minimized the likelihood of unwanted silver movement and contributed to the production of more successful brazes.

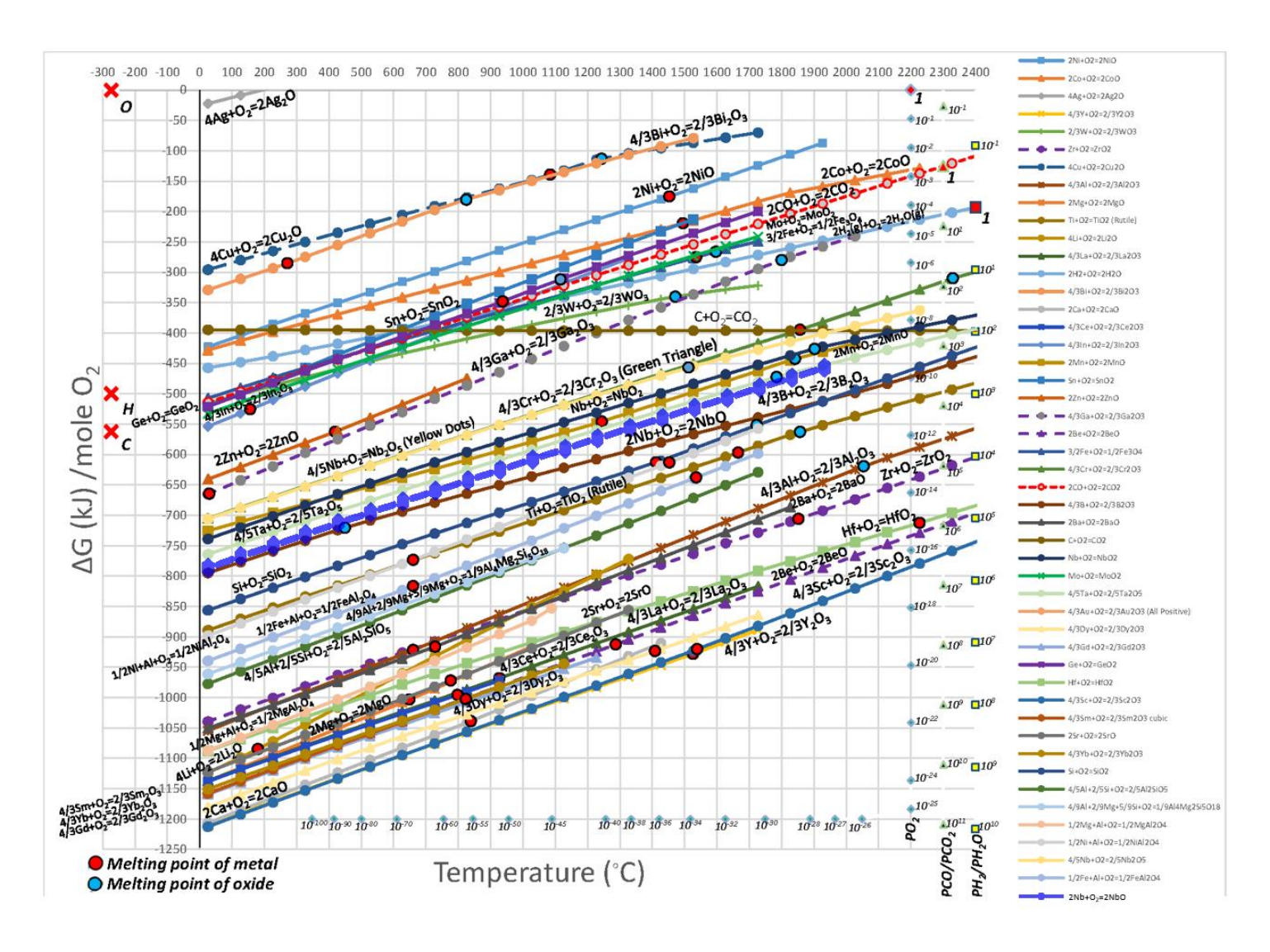


Figure A-1 Ellingham diagram of common metal and non-metal elements. Generated by Dr. Quan Zhou with thermodynamics data [168].

#### APPENDIX B: METAL-ALUMINIDE DUCTILITY DETERMINATION

The determination of whether one metal element's aluminide phase is ductile or brittle was carried out following the method detailed by Niu *et al.* [166]. In their research, they observed that when dividing the Cauchy pressure by the Young's modulus, referred to as the normalized Cauchy pressure, and plotting the results against the Pugh's modulus ratio, it resulted in a pseudo-hyperbolic curve (termed hyperbolic by the authors, but it does not conform to a true mathematical hyperbolic curve). All the ductile compounds fall into the upper-left region while the brittle compounds fall into the lower-right region.

Figure B-1 shows the Hooke's Law for isotropic continuous media [169] .

$$\begin{bmatrix} \sigma_{11} \\ \sigma_{22} \\ \sigma_{33} \\ \sigma_{23} \\ \sigma_{13} \\ \sigma_{12} \end{bmatrix} = \begin{bmatrix} \lambda + 2\mu & \lambda & \lambda & 0 & 0 & 0 \\ & \lambda + 2\mu & \lambda & 0 & 0 & 0 \\ & & \lambda + 2\mu & 0 & 0 & 0 \\ & & & \mu & 0 & 0 \\ & & & & \mu & 0 \\ & & & & \mu \end{bmatrix} \begin{bmatrix} \epsilon_{11} \\ \epsilon_{22} \\ \epsilon_{33} \\ 2\epsilon_{23} \\ 2\epsilon_{13} \\ 2\epsilon_{12} \end{bmatrix}$$

$$\lambda = \frac{E\nu}{(1+\nu)(1-2\nu)}, \ \mu = G = \frac{E}{2(1+\nu)}$$

Figure B-1 Matrix form of Hooke's law for continuous isotropic materials.

Based on the stiffness tensor of isotropic materials, the expressions for the Cauchy pressure and Bulk modulus are as follows:

$$C_{12} - C_{44} = \lambda - \mu$$

$$B = \frac{E}{3(1-2\nu)}$$

where

$$\lambda = \frac{E\nu}{(1+\nu)(1-2\nu)}$$
  $\mu = G = \frac{E}{2(1+2\nu)}$ 

As a result, the normalized Cauchy pressure can be simplified to:

$$\frac{C_{12} - C_{44}}{E} = \frac{4\nu - 1}{2(1 + \nu)(1 - 2\nu)}$$

and the Pugh's modulus ratio can be simplified to:

$$\frac{G}{B} = \frac{3(1-2v)}{2(1+v)}$$

Both terms are solely related to the Poisson ratio. Combining them, we obtain:

$$\frac{C_{12} - C44}{E} = \frac{\left(3 - 5\frac{G}{B}\right)\left(\frac{G}{B} + 3\right)}{27\frac{G}{B}}$$

Figure B-2 shows the distribution of common metals, inorganic compounds, aluminide phases of various elements, and the plot of the aforementioned equation. Based on the above equations, materials suggested to be ductile according to the criteria are compounds with a high Poisson ratio. Therefore, this diagram essentially represents the Poisson ratio of materials.

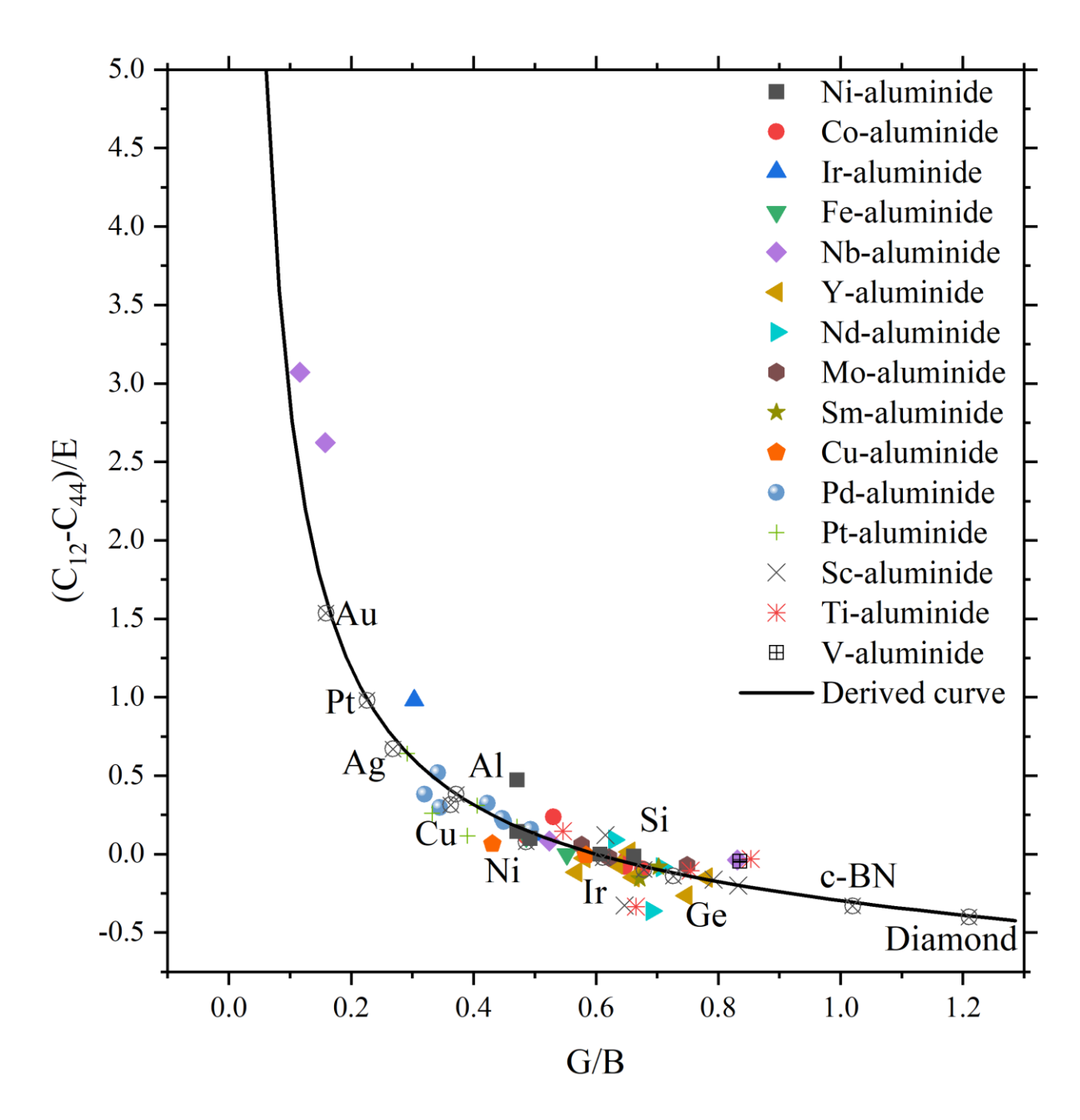


Figure B-2 The ductility analysis diagram of common metals, inorganic compounds, aluminide phases of various elements, and the derived curve.

## APPENDIX C: SIDE EFFECTS OF COMBINING PT AND NI INTERLAYERS

Experiments were conducted to evaluate the feasibility of using Pt and Ni interlayers on different sides to combine the advantages of both Ag-Pt and Ag-Ni brazes. A braze sample was prepared with Ag-25wt.%Pt interlayer on AFA and Ni interlayer on 441, with pure Ag foil in between. However, delamination occurred after firing, indicating that the two substrates were not properly brazed together.

Cross-sectional SEM analyses revealed that diffusion occurred, and Pt and Ni reacted with each other, depleting the interlayer and resulting in poor bonding. Figure C-1 shows the microstructure and the interfacial composition. This reaction was particularly detrimental on the AFA side, where the Ag joint remained adhered to the 441 substrate.

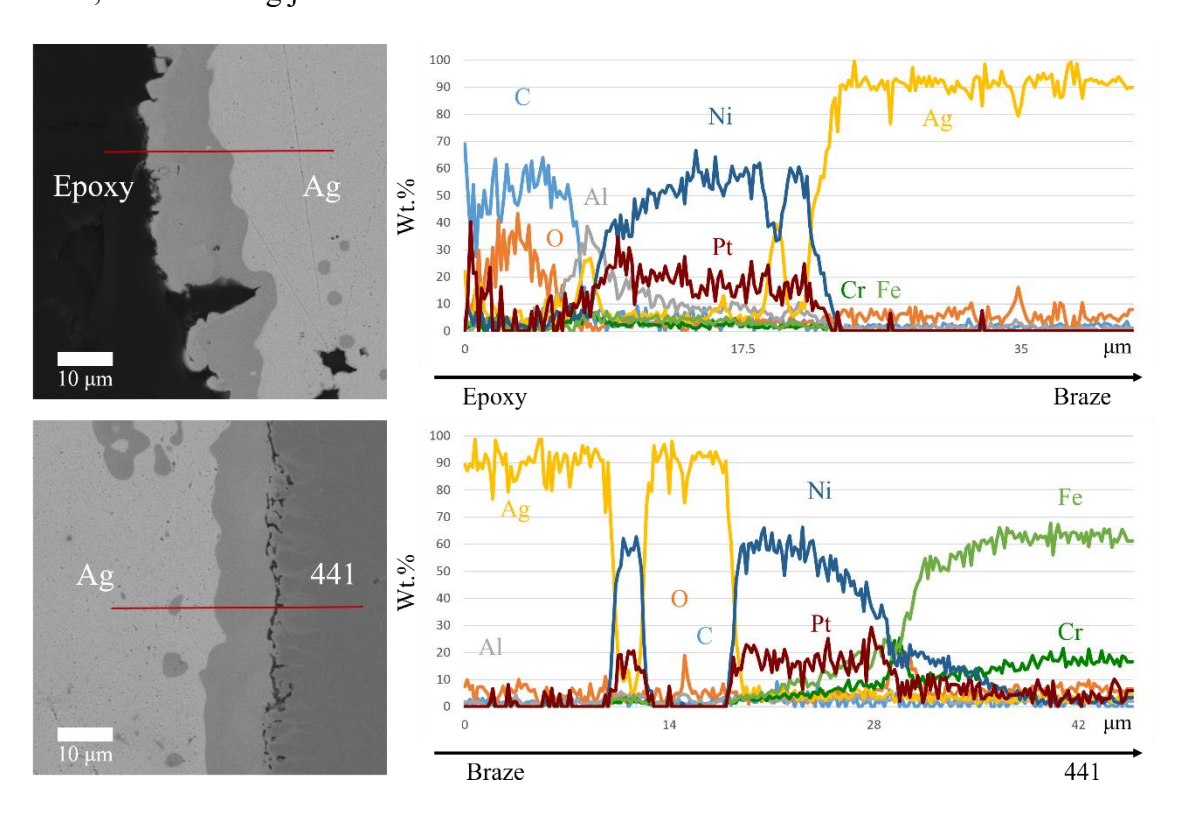


Figure C-1 Back-scattered scanning electron microscopy images and energy dispersive X-ray spectroscopy analysis of the AFA-25wt.%Pt-Ag-Ni-441 sample.